

Doctoral Thesis in Department of Molecular Science and Technology

**Hyaluronan-bile acid nanoparticles: Implications  
as a nanomedicine for the treatment of obesity-  
related chronic inflammatory diseases**

The Graduate School, Ajou University

Department of Molecular Science and Technology

Wang Hee Lee

# **Hyaluronan-bile acid nanoparticles: Implications as a nanomedicine for the treatment of obesity- related chronic inflammatory diseases**

**Advisor: Professor Wook Kim**

A thesis submitted to the faculty of the Graduate School of Ajou University in  
partial fulfillment of the requirements for the doctoral degree of Engineering in  
the Department of Molecular Science and Technology

2023.2

Department of Molecular Science and Technology

Graduate School of Ajou University

Wang Hee Lee

The Doctoral thesis of Wang Hee Lee in the Department of  
Molecular Science and Technology is hereby approved

The Graduate School of Ajou University

December 16, 2022

Thesis Defense Committee Chair

Eunha Kim Ph.D



Ki Woo Kim, Ph.D



Yong Jae Lee, Ph.D



Tae Hyeon Yoo, Ph.D



Wook Kim Ph.D



## **ABSTRACT**

Wang Hee Lee

Advisor: Professor Wook Kim

Department of Molecular Science and Technology

Graduate School of Ajou University

Self-assembled hyaluronic acid nanoparticles (HANPs), consisting of the outermost hydrophilic HA layer surrounding multiple hydrophobic inner moieties, have been investigated broadly as a nanocarrier. Interestingly, several groups have recently reported that an empty HANP not bearing any drug is a potential therapeutic agent for the treatment of type 2 diabetes, arthritis, and atherosclerosis. Here, I report the efficacy of HANP in another chronic inflammatory diseases including obesity and psoriasis. First, I confirmed the potential of self-assembled hyaluronan-bile acid nanoparticles (HABAs) as therapeutics to treat obesity by assessing their in vitro and in vivo effects on adipogenesis and lipogenesis. Treatment of 3T3-L1 preadipocytes with HABA resulted in a dose-dependent suppression of adipogenesis and lipid accumulation, and decreased the expression of key adipogenic and lipogenic regulators. However, these HABA mediated effects were not observed in 3T3-L1 cells transfected with siRNAs against CD44. Consistent with in-vitro results, HABA

treatment of diet-induced obese mice reduced the body weight and epididymal fat mass, and suppressed the induction of adipogenic and lipogenic regulators, while these effects were attenuated in the CD44-null mice. Subsequently, I investigated the potential of HABA as therapeutics for treating psoriasis. HABA exerted potent therapeutic efficacy against psoriasis-like skin by suppressing hyperproliferation of keratinocyte and M1 polarization of macrophage without overt toxicity signs. Transcutaneously administered HABAs were found to be accumulated and associated with pro-inflammatory M1 macrophages in the inflamed skin, and suppressed the M1 polarization of macrophage. As a result, HABA, compared with conventional drugs, revealed remarkable efficacy on IMQ-induced psoriasis-like mice. Taken together, I report that HANP have potential as a nanomedicine for treating obesity-related chronic inflammatory diseases.

**KEYWORDS:** Self-assembled hyaluronic acid nanoparticles (HANPs), Self-assembled Hyaluronan-Bile Acid nanoparticles (HABA), Chronic inflammatory diseases, Obesity, Psoriasis

---

## **CONTENTS**

<b>ABSTRACT.....</b>	<b>i</b>
<b>CONTENTS.....</b>	<b>iii</b>
<b>LIST OF TABLES.....</b>	<b>viii</b>
<b>LIST OF FIGURES.....</b>	<b>viii</b>
<b>ABBREVIATIONS.....</b>	<b>xii</b>
<b>PART I - Self-assembled hyaluronic acid nanoparticle suppresses fat accumulation via CD44 in diet-induced obese mice.....</b>	<b>1</b>
<b>I-1. INTRODUCTION.....</b>	<b>2</b>
<b>I-2. RESULTS.....</b>	<b>5</b>
I-2.1 Synthesis and characterization of self-assembled HACN.....	<b>5</b>
I-2.2 Self-assembled HACNs suppress adipogenesis and lipogenesis during the 3T3-L1 differentiation .....	<b>10</b>
I-2.3 HACN mediated effects on adipogenesis and lipogenesis depend on	

CD44.....	15
I-2.4 In vivo effects of HACN in WT and CD44 KO DIO mice.....	20
I-2.5 Effects of CA and free HA on adipogenesis and weight change....	26
<b>I-3. DISCUSSION.....</b>	<b>31</b>

**PART II - Hyaluronic Acid Nanoparticles as a Topical Agent for Treating Psoriasis..... 33**

<b>II-1. INTRODUCTION.....</b>	<b>34</b>
<b>II-2. RESULTS.....</b>	<b>37</b>
II-2.1. Synthesis and characterization of self-assembled HALN.....	37
II-2.2. Therapeutic efficacy of HALN administered via the subcutaneous route in psoriasis-like skin dermatitis.....	47
II-2.3. Accumulation of Transcutaneously Administered HALN in IMQ-Inflamed Dermis.....	63
II-2.4. Efficacy of Transcutaneously Administered HALNs against Psoriasis-like Skin Dermatitis.....	
II-2.5. Macrophages as a Target in IMQ-Inflamed Skin.....	97

II-2.6. Modulation of Macrophage Polarization.....	104
<b>II-3. DISCUSSION.....</b>	<b>117</b>
<b>III. MATERIALS and METHODS.....</b>	<b>120</b>
2.1. Materials.....	120
2.2. Characterization of Compounds.....	120
2.3. CA Ester.....	120
2.4. EtCA .....	121
2.5. HA-CA.....	122
2.6. LCA Ester .....	122
2.7. EtLCA .....	123
2.8. HA-LCA .....	124
2.9. 10k-HA-LCA.....	124
2.10. Cy5.5-HA .....	125
2.11 Cy5.5-HA-LCA and Cy5.5-HA-CA .....	125
2.12. Characterization of HANPs.....	126

2.13. The 3T3-L1 cell culture and differentiation.....	126
2.14. The 3T3-L1 cell viability assay.....	127
2.15. Transfection of small tnerfering RNA .....	128
2.16. Mice .....	128
2.17. Histology and Immunofluorescence.....	128
2.18. Quantitative real-time PCR analysis.....	130
2.19. High-fat diet induced obesity mice.....	132
2. 20. Determination of adipocyte size .....	132
2.21. Oil-red-O staining.....	133
2. 22. Colorimetric Assessment of Terminal N-Acetyl-d-Glucosamine (Hyaluronan Breakdown Products).....	133
2. 23. Psoriasis-like Mouse Models.....	134
2.24. Cell Isolation from the Shaved Dorsal Skin.....	136
2.25. Hematological Toxicity.....	136
2.26. In Vivo Toxicity Test.....	137
2.27. In Vivo Skin Penetration Studies.....	137
2.28. Multi-Photon Microscopy.....	128
2.29. Ex Vivo Biodistribution.....	128

2.30. Cell Culture.....	139
2.31. In Vivo Depletion of Macrophages.....	140
2.32. In Vitro Competitive Inhibition Assay.....	140
2.33. In Vitro Cellular Uptake Assay.....	141
2.34. RNA-seq and Bioinformatic Analysis.....	141
2.35. Immunoblot Analysis.....	142
2.36. In Vitro Macrophage Polarization.....	143
2.37. Statistical analysis.....	144
<b>IV. CONCLUSION.....</b>	<b>146</b>
<b>V. REFERENCE.....</b>	<b>147</b>
<b>VI. ABSTRACT IN KOREAN (국문초록).....</b>	<b>157</b>

## **LIST OF TABLES**

Table 1. Characteristics of HACN in part 1.....	<b>6</b>
Table 2. Characteristics of HANPs in part 2.....	<b>39</b>
Table 3. Primer sequences used in this report.....	<b>131</b>

## **LIST OF FIGURES**

### **Part I. Self-assembled hyaluronic acid nanoparticle suppresses fat accumulation via CD44 in diet-induced obese mice**

Figure 1. Synthesis and characterization of self-assembled HACN.....	<b>7</b>
Figure 2. Effects of HACN on 3T3-L1 adipocyte differentiation.....	<b>11</b>
Figure 3. Effects of HACN on the expression of adipogenic and lipogenic genes in differentiated 3T3-L1 adipocytes.....	<b>13</b>
Figure 4. Effects of HACN on 3T3-L1 adipocyte differentiation following CD44 silencing.....	<b>16</b>
Figure 5. Effects of HACN on the expression of adipogenic and lipogenic genes in differentiated 3T3-L1 adipocytes following CD44 silencing.....	<b>18</b>
Figure 6. Effects of HACN on epididymal fat mass in WT and CD44 KO	

DIO mice.....	22
Figure 7. Effects of HACN on the expression of adipogenic and lipogenic genes in WT and CD44 KO DIO mice.....	24
Figure 8. Effects of CA and free HA on 3T3-L1 adipocyte differentiation.	27
Figure 9. Effects of 235k-HANP treatment in WT and CD44 KO DIO mice on body weight and adipocyte size.....	29
 <b>Part II. Self-assembled hyaluronic acid nanoparticles as a topical therapeutic agent for the treatment of psoriasis</b>	
Figure 1. Synthesis of self-assembled HALN.....	40
Figure 2. Fluorescamine assay for verifying the amount of EtLCA or EtCA in HACN or in HALN.....	43
Figure 3. Characterization of self-assembled HALN.....	45
Figure 4. Subcutaneous administration of HALN protects animals against psoriasis-like skin dermatitis induced by IMQ.....	49
Figure 5. Subcutaneous administration of HALN ameliorates IMQ-induced psoriasis-like skin inflammation.....	51
Figure 6. Effects of subcutaneously administered LCA on IMQ-induced	

psoriasis-like skin dermatitis.....	54
Figure 7. Effects of HALN, LCA, and MTX on IL-23-induced psoriasis-like skin dermatitis.....	57
Figure 8. Safety profiles of HALN.....	60
Figure 9. Ex vivo skin penetration of Cy5.5-HALN.....	65
Figure 10. Transcutaneously administered HALN localizes in IMQ-inflamed dermis.....	67
Figure 11. TLR4-mediated association of Cy5.5-HALN with M1 macrophages.....	70
Figure 12. In vivo skin penetration efficiency of Cy5.5-HALN-1, Cy5.5-HALN-2, and Cy5.5-HALN-3.....	72
Figure 13. Ex vivo biodistribution of transcutaneously administered Cy5.5-HALN.....	74
Figure 14. The synthesis of HACN.....	76
Figure 15. Ex vivo skin penetration efficiency of Cy5.5-HACN.....	78
Figure 16. Transcutaneous administration of HALN protects animals against IMQ-induced psoriasis-like skin dermatitis.....	82
Figure 17. Effects of HALN size on IMQ-induced psoriasis-like skin	

dermatitis.....	85
Figure 18. Effects of 10k-HALN on IMQ-induced psoriasis-like skin dermatitis.....	88
Figure 19. Effects of HALN, Dermovate, and Daivonex on IMQ-induced psoriasis-like skin inflammation.....	91
Figure 20. Effects of HALN, anti-IL-17A antibody, and MTX on IMQ-induced psoriasis-like skin dermatitis.....	94
Figure 21. Effects of HACN on IMQ-inflamed mice after macrophage depletion.....	99
Figure 22. Clodronate-mediated depletion of macrophages in normal and IMQ-inflamed mice.....	102
Figure 23. HACN alters LPS-induced gene expression patterns in BMDMs.....	106
Figure 24. HACN can competitively inhibit the LPS-binding capacity of TLR4.....	109
Figure 25. Relative densities for TLR4 downstream signaling proteins determined by western blot analysis in THP-1.....	111
Figure 26. HALN inhibits LPS-induced M1 polarization of macrophages..	113

Figure 27. HALN inhibits LPS-induced M1 polarization of macrophages.. **116**

## ABBREVIATIONS

T2D	type 2 diabetes
PPAR $\gamma$	proliferator- activated receptor gamma
C/EBP $\alpha$	CCAAT/enhancer binding protein alpha
Fabp4	fatty acid-binding protein 4
AdipoQ	adiponectin
FAS	fatty acid synthase
SCD1	stearoyl-CoA desaturase-1
HA	hyaluronic acid
NPs	nano-sized particles
DIO	diet-induced obesity
HANP	self-assembled hyaluronic acid nanoparticle
WT	wildtype
KO	knockout
CA	5 $\beta$ -cholanic acid
HACN	self-assembled hyaluronan-5 $\beta$ -cholanic acid nanoparticle
TEM	Transmission electron microscope

HABA	hyaluronan-bile acid nanoparticles
IMQ	imiquimod
NHS	N-hydroxysuccinimide
EDC·HCl	1-ethyl-3-(dimethylamino)propyl carbodiimide·hydrochloride
HOBr	hydroxybenzotriazole
TLC	thin-layer chromatography
TMS	tetramethylsilane
LRMS	low-resolution mass spectrometry
PBS	phosphate buffered saline
TEM	Transmission electron microscope
LCA	lithocholic acid
HALN	Self-assembly of HA-LCA nanoparticle
DMF	dimethylformamide
DMEM	Dulbecco's modified eagle medium
DMI	dexamethasone, 3-iso-butyl-1-methylxantine and insulin
MTS	3-(4,5-dimethylthiazol-2-y)-5-(3-carboxymethoxyphenyl)-2-(4-sulfophenyl)-2H-tetrazolium
siRNAs	small interfering RNAs

eWAT	Epididymal white adipose tissue
PFA	paraformaldehyde
H&E	hematoxylin and eosin
DW	distilled water
qPCR	quantitative real-time polymerase chain reaction
HFD	high-fat diet
i.p	intraperitoneally
DS	Degree of substitution
HYAL	hyaluronidase
DMAB	p-dimethylaminobenzaldehyde
PASI	Area and Severity Index
LMW	low-molecular weight
CMC	critical micelle concentration
control siRNA	siCtrl
NC	negative control

**PART I**

**Self-assembled hyaluronic acid nanoparticle  
suppresses fat accumulation via CD44 in diet-  
induced obese mice**

## I-1. INTRODUCTION

Obesity is a major risk factor responsible for the development of various metabolic diseases, such as type 2 diabetes (T2D), cardiovascular diseases, hypertension, and nonalcoholic fatty liver disease. It is characterized by an abnormal expansion of adipose tissue mass, resulting from two distinct mechanisms: hyperplasia (increased formation of new adipocytes in the process of adipogenesis) and hypertrophy (increase in size of existing adipocytes due to lipogenesis and lipid accumulation). Hyperplasia occurs via the differentiation of preadipocytes into mature adipocytes, which have remarkable hypertrophic potential, and increased adipocyte size is closely associated with increased adipose tissue inflammation and systemic insulin resistance.<sup>1</sup> Adipogenesis and lipogenesis are controlled through the sequential activation of multistep gene regulations that are mainly mediated by the two primary transcription factors, proliferator-activated receptor gamma (PPAR $\gamma$ ) and CCAAT/enhancer-binding protein alpha (C/EBP $\alpha$ ).<sup>2-4</sup> As the master regulator of adipogenesis, PPAR $\gamma$  induces adipocyte differentiation and maturation, while C/EBP $\alpha$  is one of the most important downstream effectors of PPAR $\gamma$ .<sup>5</sup> As a result, PPAR $\gamma$  and C/EBP $\alpha$  cooperate functionally to fully drive the adipocyte maturation program by inducing the transcription of target genes that are expressed in the mature adipocytes, such as fatty acid-binding protein 4 (Fabp4) and adiponectin (AdipoQ).<sup>6</sup> In addition, both the proteins also promote lipid accumulation by modulating the expression of fatty acid synthase (FAS) and stearoyl-CoA desaturase-1 (SCD1).<sup>7-9</sup>

Therefore, pharmacological therapies that suppress adipogenesis and lipogenesis by inhibiting the activity of PPAR $\gamma$  and C/EBP $\alpha$  would be useful for the prevention or treatment of obesity. However, an ideal anti-obesity strategy targeting adipogenesis and lipogenesis has not been implemented yet.

Owing to its biodegradability, biocompatibility, and specific receptor binding characteristics, hyaluronic acid (HA) has received increasing attention for biomedical applications such as tissue engineering, drug delivery, and molecular imaging<sup>10-14</sup>. In particular, amphiphilic HA derivatives capable of being self-assembled into nano-sized particles (NPs) in an aqueous condition, have been extensively investigated as drug carriers to actively target pathological sites that express the HA receptor, CD44.<sup>15</sup> Interestingly, apart from its role as a drug carrier, it has been recently demonstrated that an empty HANP (not bearing any drug) is a potential therapeutic agent, for the treatment of inflammatory diseases, including T2D and atherosclerosis<sup>16, 17</sup>. Here, I identified that empty HANPs without any drug, reduced body weight and fat mass in diet induced obesity (DIO) mice, leading to an improvement in obesity-related metabolic disorders, adipose tissue inflammation, insulin sensitivity, and glycemic control.<sup>17</sup> However, the mechanism by which HANP reduces fat mass remains unclear.

In this study, I demonstrate the in vitro and in vivo effects of self-assembled hyaluronic acid nanoparticle (HANP) on adipogenesis and lipogenesis during the adipocyte differentiation. In addition, using wildtype (WT) and CD44-knockout (KO)

DIO mice, I also show that these effects of HANP on adipogenesis and lipogenesis are mediated through CD44.



## I-2. RESULTS

### I-2.1. Synthesis and characterization of self-assembled HACN

Self-assembled hyaluronan-5 $\beta$ -cholanic acid nanoparticle (HACN) was synthesized by chemical modification of low-molecular weight (MW = 10 kDa) HA with hydrophobic CA (Figure 1A), as previously described HANPs<sup>18</sup>. The amphiphilic HA conjugate bearing 5 CAs per 100 sugar residues of HA, was confirmed using <sup>1</sup>H-NMR in our previous report.<sup>17</sup> Transmission electron microscope (TEM) images showed that the HACN was spherical in shape (Figure 1B). Their hydrodynamic diameter and zeta potential, confirmed by dynamic light scattering, were  $223.1 \pm 7.2$  nm and  $-25.6 \pm 5.2$ , respectively (Table 1). The particle size of the HACN decreased as the DS increased due to the formation of a more compact hydrophobic inner core (Figure 1C). The critical micelle concentration (CMC) value of HACN was above of 0.049 mg/mL, which is significantly lower than that of lower MW detergent<sup>19</sup> (Figure 1D). Moreover, The HACN exhibited the long-term colloidal stability in PBS (pH 7.4) and water solution for at least 3 days (Figure 1E,F). The cytotoxicity of various HACN concentrations (50, 100, and 200  $\mu$ g/ml) was monitored by measuring cell proliferation of 3T3-L1 cells using the MTS assay Kit. I confirmed that the cell viability was not affected by HACN during the 3T3-L1 differentiation (Figure 1G).

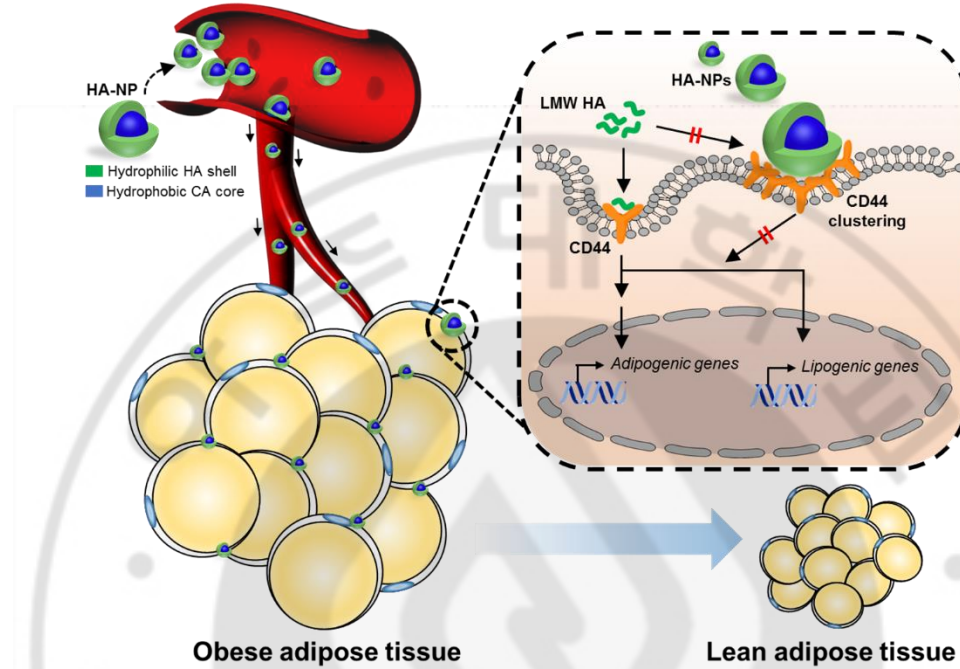
**Table 1.** Characteristics of HACN

Sample	DS <sup>a</sup>	Size (nm) <sup>b</sup>	$\zeta$ (mV) <sup>c</sup>
HACN	5	$223.1 \pm 7.2$	$-25.6 \pm 5.2$

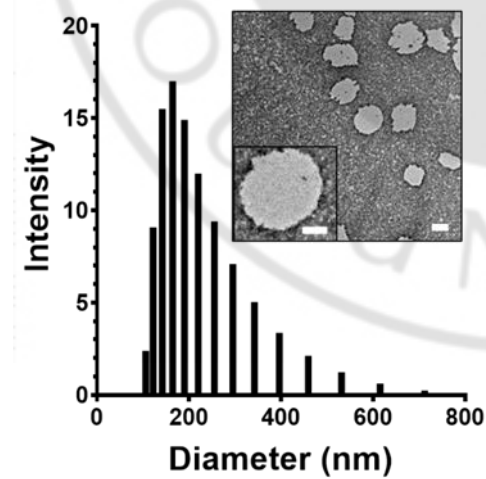
<sup>a</sup> Degree of substitution of CA, estimated from  $^1\text{H-NMR}$  spectrum. <sup>b</sup> Measured by DLS. <sup>c</sup> Measured by Zeta-sizer.

**Figure 1**

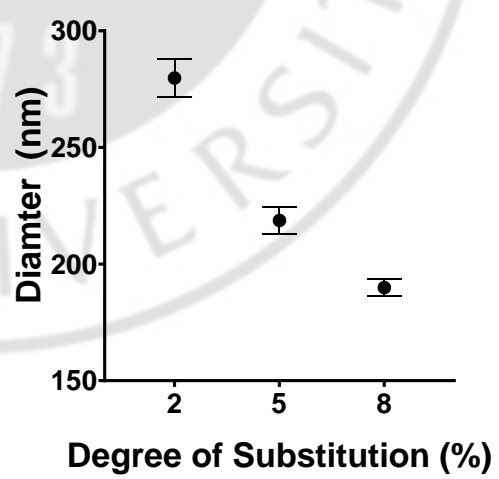
**A**



**B**



**C**



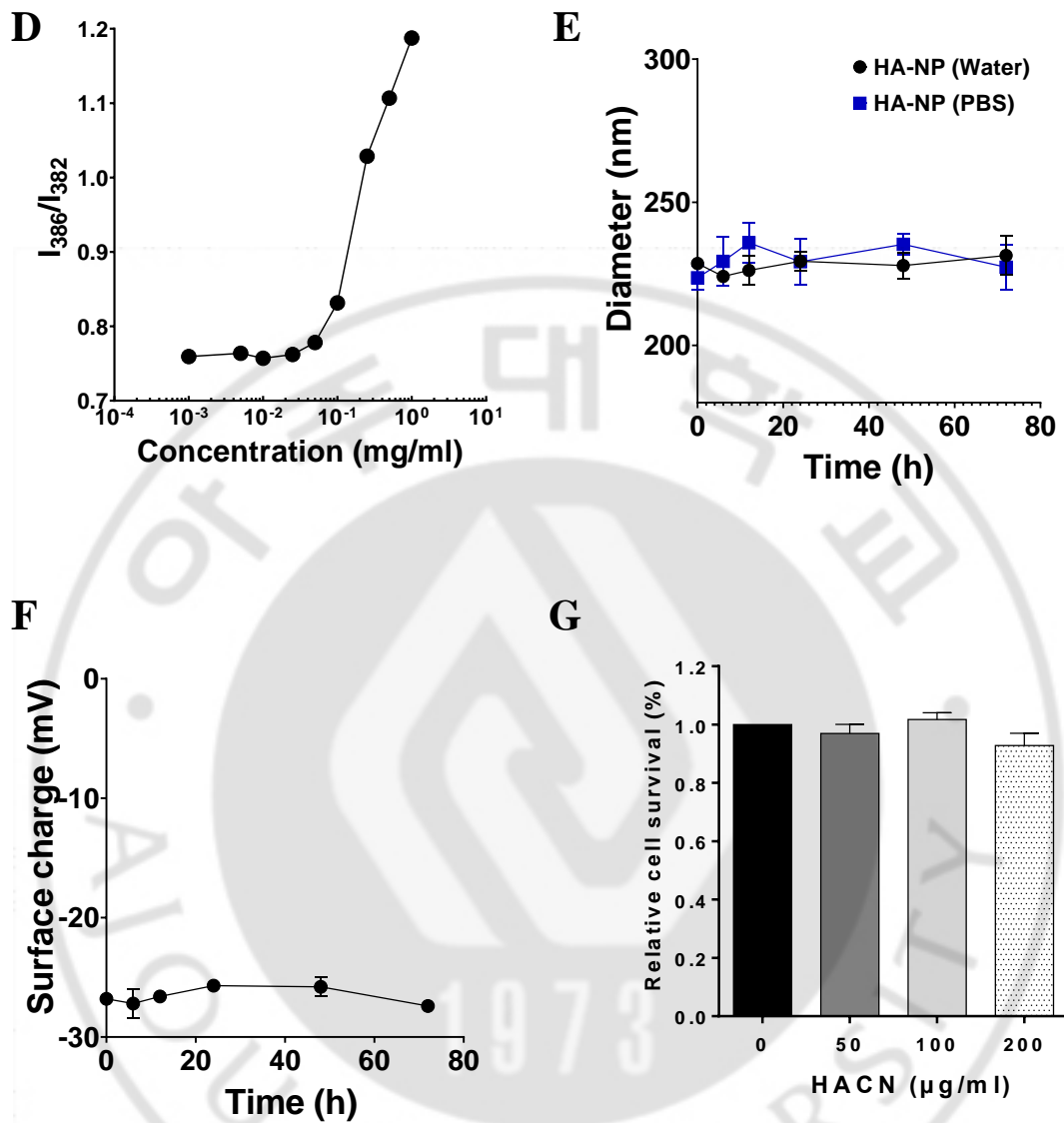


**Figure 1. Synthesis and characterization of self-assembled HACN**

(A) Schematic illustration of HACN for the regulation of adipogenesis and lipid accumulation. (B) Size distribution and TEM image of HACN. Scale bar, 200 nm. Insets are magnified images (Scale bar, 50 nm). (C) Particle size of HANPs with different amounts of CA. (D) Intensity ratio ( $I_{386}/I_{382}$ ) from pyrene excitation spectra. (E and F) Time-dependent changes in particle size (E) and surface charge (F) of HACN in PBS and water solution as a function of time. The error bars represent standard deviation ( $n = 5$ ). (G) Cell viability of 3T3-L1 cells treated with HACN for 10 days. Data represent the mean  $\pm$  SEM ( $n = 3$ ).

## I-2.2. Self-assembled HACNs suppress adipogenesis and lipogenesis during the 3T3-L1 differentiation

Given that HACN reduces body weight in the DIO mouse model,<sup>17</sup> I investigated their effects on adipogenesis and lipogenesis. Toward this, I used 3T3-L1 which is a cell line isolated from the embryo of a mouse for research on adipogenesis and lipogenesis. 3T3-L1 cells have a fibroblast-like morphology, but, under appropriate conditions, the cells differentiate into an adipocyte-like cells. 3T3-L1 cells were treated with HACN (50, 100, or 200 µg/ml) every three days during adipocyte differentiation (Figure 2A). At the end of the treatment period, I found that HACN inhibited lipid accumulation and adipocyte differentiation in a dose-dependent manner (Figure 2B–D). Accordingly, the mRNA expression of adipogenic marker genes such as PPAR $\gamma$  and C/EBP $\alpha$  was also decreased in a dose-dependent manner by HANP (Figure 3A). Consistent with this, the mRNA levels of Fabp4 and AdipoQ, which are target genes of PPAR $\gamma$  and C/EBP $\alpha$ , were also reduced in the HACN-treated 3T3-L1 cells compared to the cells treated with PBS alone (Figure 3A). I also confirmed decreased mRNA levels of lipogenic marker genes including Fas and Scd1, following HACN treatment (Figure 3B). These results indicate that HACN has inhibitory effects on adipogenesis and lipogenesis.

**Figure 2**

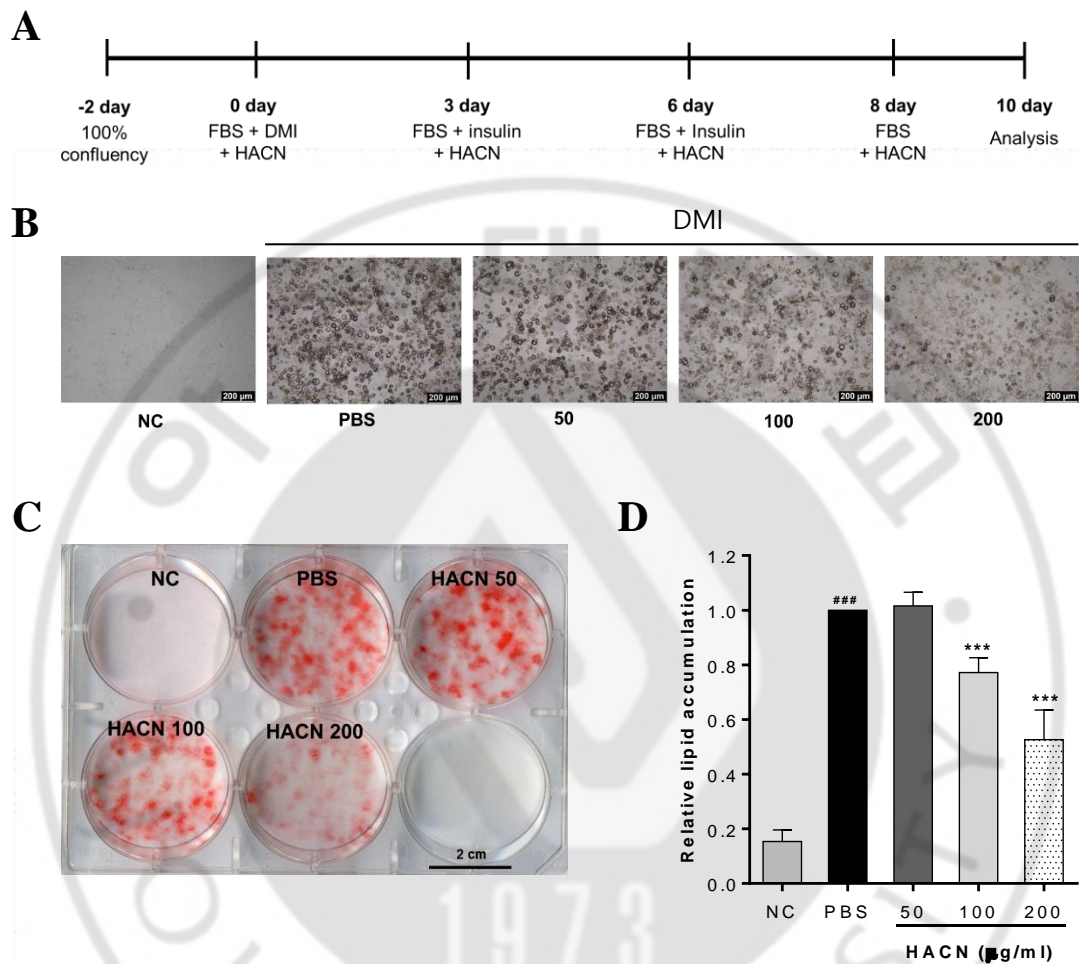
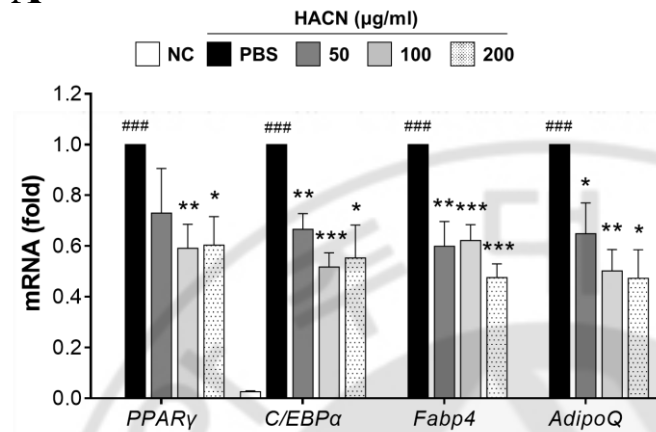


**Figure 2. Effects of HACN on 3T3-L1 adipocyte differentiation**

(A) Experimental timeline for HACN treatment during 3T3-L1 adipocyte differentiation. DMI: dexamethasone, 3-iso-butyl-1-methylxantine and insulin. (B and C) Microscopic (B) and Oil Red-O staining (C) images of differentiated 3T3-L1 adipocytes following HACN treatment. Scale bar, 200  $\mu$ m (B) and 2 cm (C). (D) Quantification of Oil red-O staining in (C). Data represent the mean  $\pm$  SEM ( $n = 3$ ).  
###P<0.001 compared with the negative control (NC) group, \*\*\*P<0.001 compared with the PBS group.

**Figure 3**

**A**



**B**

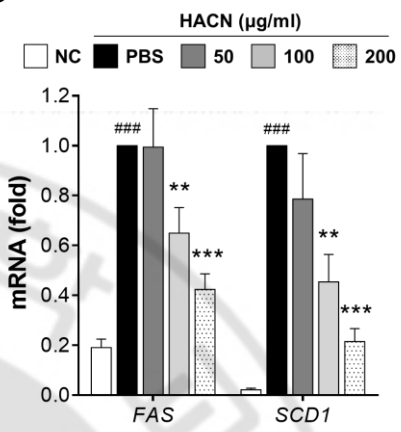


**Figure 3. Effects of HACN on the expression of adipogenic and lipogenic genes in differentiated 3T3-L1 adipocytes**

(A) The relative mRNA levels of PPAR $\gamma$ , C/EBP $\alpha$ , Fabp4, and AdipoQ in differentiated 3T3-L1 adipocytes. (B) The relative mRNA levels of Fas and Scd1 in differentiated 3T3-L1 adipocytes. The mRNA levels were measured by qPCR following HACN treatment. Data represent the mean  $\pm$  SEM (n = 3). ###P<0.001 compared with the NC group, \*P < 0.05, \*\*P < 0.01, \*\*\*P < 0.001 compared with the PBS group.

### I-2.3. HACN mediated effects on adipogenesis and lipogenesis depend on CD44

CD44 is a multifunctional membrane receptor involved in many biological functions such as cell-cell interactions, cell adhesion, and migration<sup>20-22</sup>. It is the major cell-surface HA receptor, signifying that HA-based NPs could specifically target cells that overexpress CD44<sup>23-25</sup>. Recently, it has been demonstrated that the expression of CD44 is significantly increased in adipose tissue by HFD and that effective targeting of HANPs to adipose tissues is mediated by the interaction between HANPs and CD44<sup>24-29</sup>. Thus, I evaluated whether the effects of HACN are mediated by CD44. Towards this, 3T3-L1 cells were transfected with CD44 siRNAs (siCD44) one day prior to treatment with adipogenic agents and HACN (Figure 4A). The effects of HACN on lipid accumulation and adipocyte differentiation were significantly impaired by silencing of CD44 compared to cells transfected with control siRNA (siCtrl) (Figure 4B-E). Moreover, HANPs inhibited expression of adipogenic and lipogenic genes, whereas this effect was attenuated in silencing CD44 cells (Figure 5A-F). These results suggest that effects of HACN on lipid accumulation and adipocyte differentiation depend on CD44.

**Figure 4**

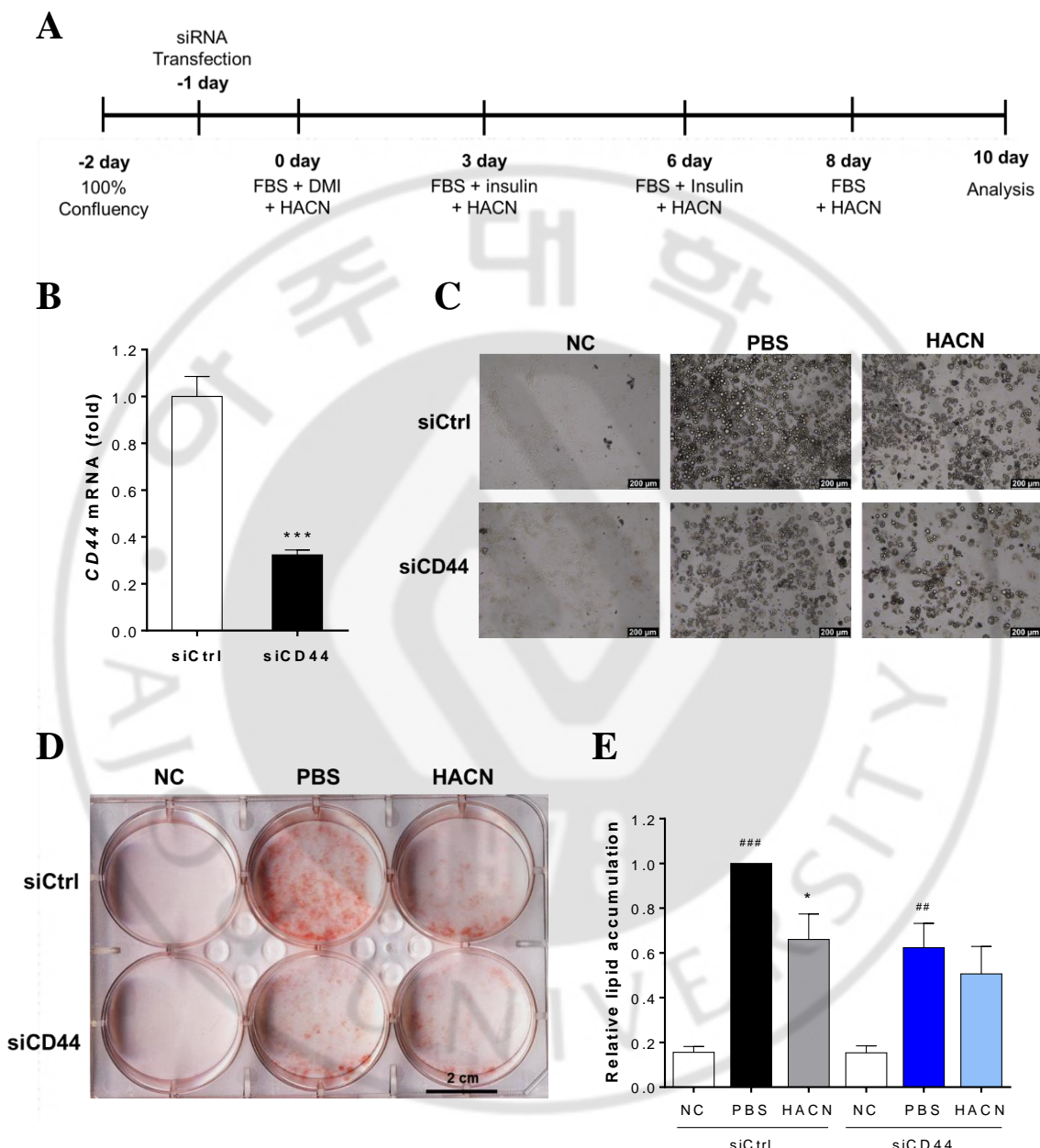


**Figure 4. Effects of HACN on 3T3-L1 adipocyte differentiation following CD44 silencing**

(A) Experimental timeline for HACN (100 µg/ml) treatment and siRNA transfection during 3T3-L1 adipocyte differentiation. (B) qPCR analysis of CD44 mRNA levels in differentiated 3T3-L1 adipocytes following siCtrl or siCD44 transfection. Data represent the mean ± SEM (n = 3). \*\*\*P < 0.001 compared with the siCtrl group. (C and D) Microscopic (C) and Oil Red O staining (D) images of differentiated 3T3-L1 adipocytes following siCtrl or siCD44 transfection followed by HANP treatment. (E) Quantification of Oil red-O staining in (D). Data represent the mean ± SEM (n = 3). ##P<0.01, ###P<0.001 compared with the NC group, \*P < 0.05 compared with the PBS group.

**Figure 5**

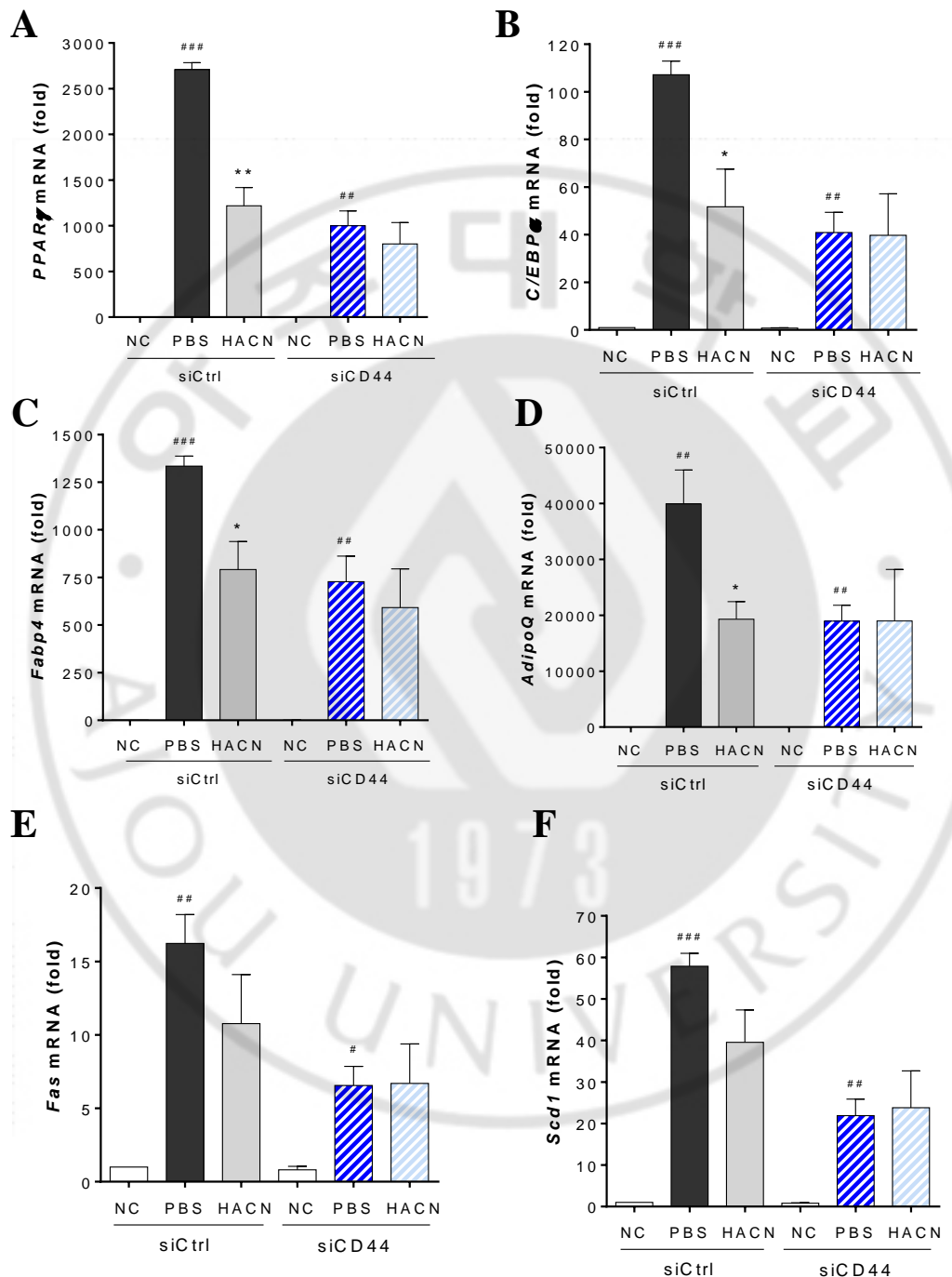


**Figure 5. Effects of HACN on the expression of adipogenic and lipogenic genes in differentiated 3T3-L1 adipocytes following CD44 silencing**

(A-F) The relative mRNA levels of PPAR $\gamma$  (A), C/EBP $\alpha$  (B), Fabp4 (C), AdipoQ (D), Fas (E), and Scd1 (F) measured by qPCR in differentiated 3T3-L1 adipocytes following siCtrl or siCD44 transfection followed by HACN (100  $\mu$ g/ml) treatment. Data represent the mean  $\pm$  SEM ( $n = 3$ ). #P<0.05, ##P<0.01, ###P<0.001 compared with the NC group, \*P < 0.05, \*\*P < 0.01 compared with the PBS group.

#### I-2.4. In vivo effects of HACN in WT and CD44 KO DIO mice

I next confirmed the in vivo effects of HACN using DIO mice. Male C57BL/6 WT and CD44 KO mice were fed an HFD for 20 weeks and administered i.p. injections of vehicle (PBS) or HACN (150 mg/kg) daily for additional 30 days. At the end of the treatment period, the mRNA expression of CD44 was found to be decreased following HACN treatment in WT mice (Figure 6A), and their body weight and epididymal fat mass were significantly reduced (Figure 6B,C). However, these reductions by HACN were not observed in the CD44 KO mice (Figure 6B,C). These effects were further supported by the adipocyte size in the epididymal fat tissues of WT and CD44 KO mice; HANP decreased the adipocyte size in the WT, but not in the CD44 KO mice (Figure 6D,E). I also observed that the mRNA levels of adipogenic and lipogenic genes in the epididymal fat tissues from WT mice were decreased by HANP, whereas these HANP mediated effects were attenuated in the epididymal fat tissues from CD44 KO mice (Figure 7A–F). Taken together, it is likely that HANP inhibits adipogenesis and lipogenesis by blockade of CD44. The biological effects of HANPs are attributable to multiple CD44 binding sites present on the hydrophilic HA shell, irrespective of hydrophobic constituents (CA) and the MWs of free HA.<sup>17</sup> Through these multivalent or repeated binding sites, it is likely that HANP binds simultaneously to many CD44 receptors, leading to clustering and subsequent inactivation of CD44 (Figure. 1A).

Adipogenesis and lipogenesis play a critical role in the development of obesity

due to the expansion of the total adipose tissue mass that contribute to complications such as insulin resistance. We previously reported that HANP caused a reduction in the body weight and eWAT mass in DIO mice, leading to the improvement of hormonal/metabolic abnormalities, glycemic control, and insulin sensitivity.<sup>17</sup> This is in agreement with our current findings of an inhibitory role of HACN in adipogenesis and lipogenesis. Taken together, our results suggest that HANP contributes to decreased body weight likely due to an inhibition of adipogenesis and lipogenesis in a CD44-dependent manner.

**Figure 6**

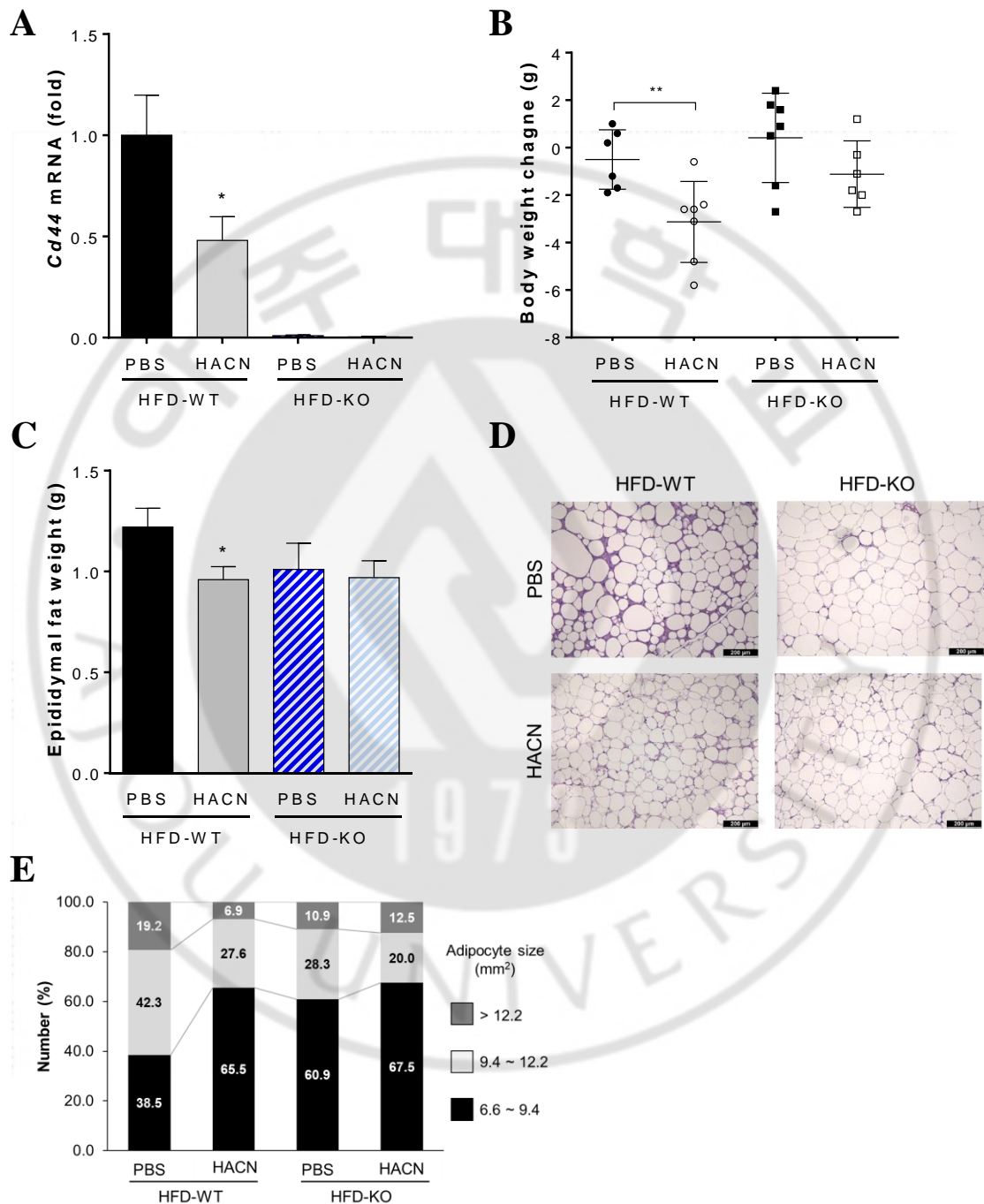


**Figure 6. Effects of HACN on epididymal fat mass in WT and CD44 KO DIO mice**

(A) qPCR analysis of CD44 mRNA levels in the eWAT of WT PBS- or HACN treated and KO PBS- or HACN treated in DIO mice. (B) Body weight change of PBS- or HANP-treated DIO mice. (C) Epididymal fat weights of PBS- or HANP-treated DIO mice. (D) Representative images ( $\times 100$ ) of H&E staining in the eWAT of PBS or HANP-treated WT or CD44 KO DIO mice. (E) The size distribution of adipocytes in the eWAT of PBS or HANP-treated WT or CD44 KO DIO mice. Data represent the mean  $\pm$  SEM (n=3-9). \*P < 0.05, \*\*P < 0.01 compared with the PBS group.

**Figure 7**

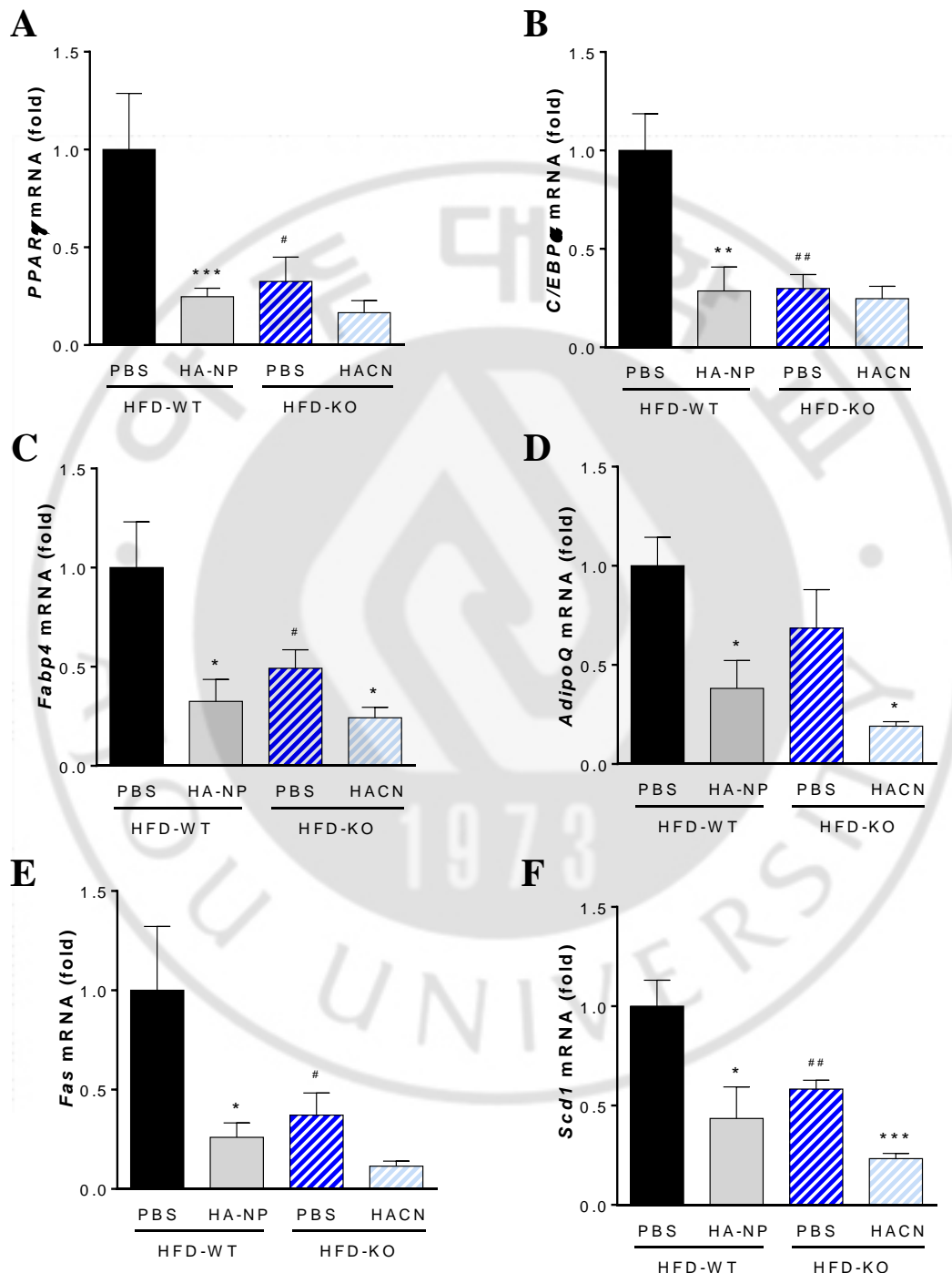


**Figure 7. Effects of HACN on the expression of adipogenic and lipogenic genes in WT and CD44 KO DIO mice**

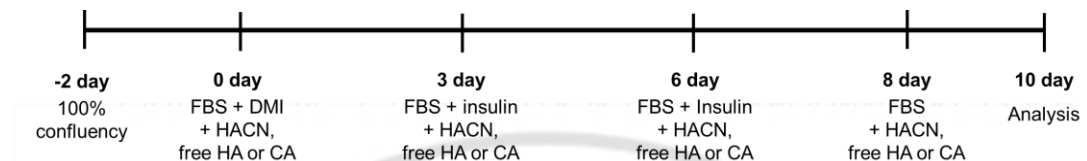
(A-F) The relative mRNA expression of PPAR $\gamma$  (A), C/EBP $\alpha$  (B), Fabp4 (C), AdipoQ (D), Fas (E), and Scd1 (F) measured by qPCR in the same eWAT. Data represent the mean  $\pm$  SEM (n=3-9). #P<0.05, ##P<0.01 compared with the WT-PBS group, \*P < 0.05, \*\*P < 0.01, \*\*\*P < 0.001 compared with each PBS group.

### I-2.5. Effects of CA and free HA on adipogenesis and weight change

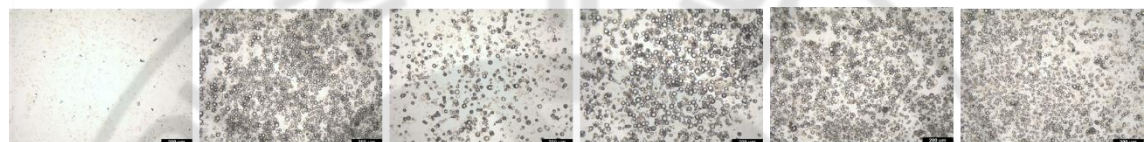
To confirm the effect of CA and MW of HA on adipogenesis, I compared the effects of HACN with those of free HAs (10 kDa and 2000 kDa) and CA during adipocyte differentiation (Figure 8A). Lipid accumulation and adipocyte differentiation were inhibited by HACN, but not by CA and free HAs (Figure 8B,C). Similar patterns were observed in the mRNA expression of adipogenic and lipogenic genes (Figure 8D,E). In addition, I further verified the *in vivo* effects of other self-assembled HACN (235k-HACN), consisting of higher MW HA (MW =235 kDa) as previously described.<sup>17</sup> The hydrodynamic diameter and zeta potential of 235k-HACN were  $221.0 \pm 3.1$  nm and  $-25.7 \pm 1.3$  mV, respectively.<sup>17</sup> WT mice were fed an HFD for 20 weeks and administered i.v. injections of vehicle (PBS), 235k-HACN (20 mg/kg), 235 kDa HA (20 mg/kg) or CA (2 mg/kg) daily for additional 28 days. Similar with HACN, 235k-HACN significantly reduced body weight and adipocyte size, whereas this reduction was not observed by 235 kDa HA and CA (Figure 9). Thus, these results suggest that, irrespective of the hydrophobic constituent and the MW of free HA, the effects of HACNs on body weight and fat accumulation are due to the presence of self-assembled HA shell.

**Figure 8**

**A**



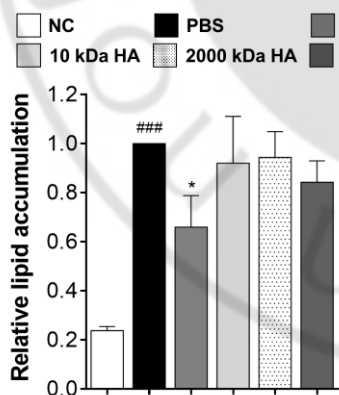
**B**



**C**



**D**



**E**

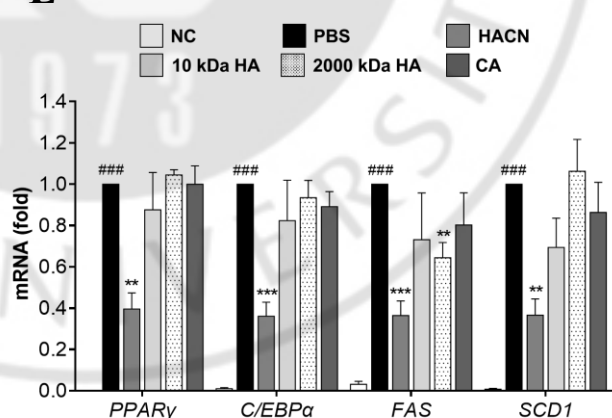
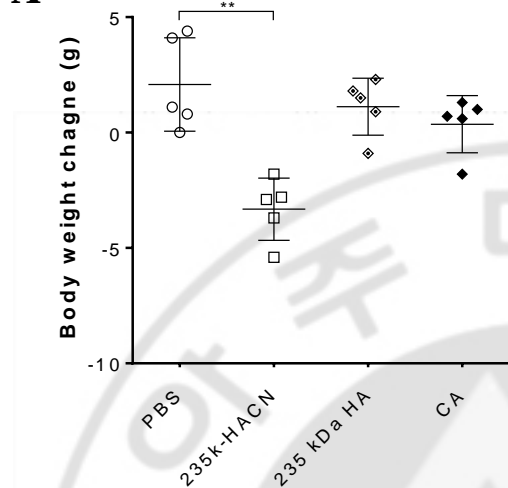


**Figure 8. Effects of CA and free HA on 3T3-L1 adipocyte differentiation**

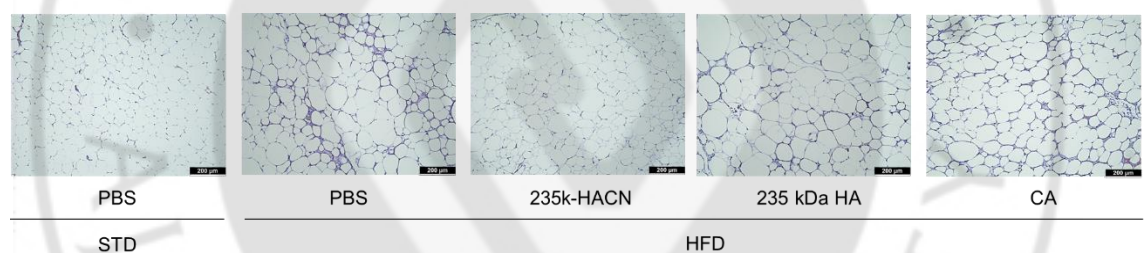
(A) Experimental timeline for the treatment of HANP (200 µg/ml), 10 kDa and 2000 kDa free HA (200 µg/ml), or CA (10 µg/ml) during 3T3-L1 adipocyte differentiation. DMI: dexamethasone, 3-iso-butyl-1-methylxantine and insulin. (B and C) Microscopic (B) and Oil Red O staining (C) images of differentiated 3T3-L1 adipocytes following the treatment. Scale bar, 200 µm (B) and 2 cm (C). (D) Quantification of Oil red-O staining in (C). (E) The relative mRNA levels of adipogenic and lipogenic genes in differentiated 3T3-L1 adipocytes. The mRNA levels were measured by qPCR following the treatment. Data represent the mean ± SEM ( $n = 3$ ).  $^{###}P < 0.001$  compared with the NC group,  $^*P < 0.05$ ,  $^{**}P < 0.01$ ,  $^{***}P < 0.001$  compared with the PBS group.

## Figure 9

A



B



C

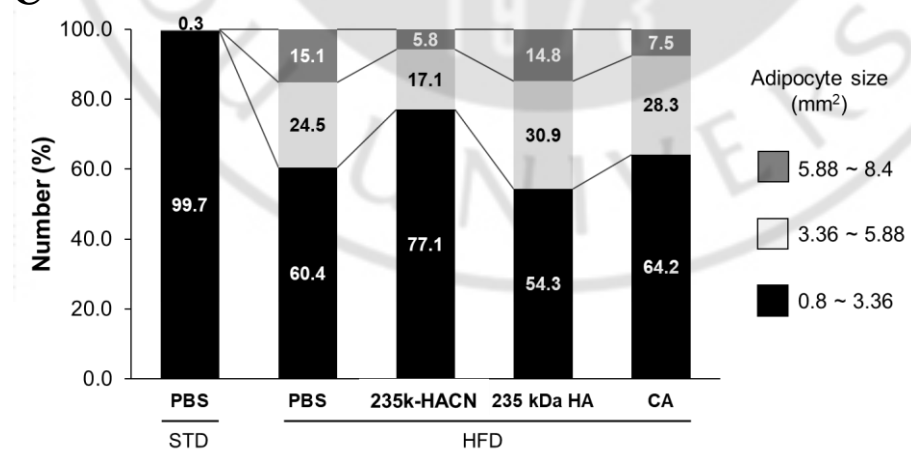


**Figure 9. Effects of 235k-HANP treatment in WT and *CD44* KO DIO mice on body weight and adipocyte size**

(A) Body weight change of WT and *CD44* KO DIO mice treated with PBS, 235k-HANP, 235 kDa HA or CA. (B) Representative images ( $\times 200$ ) of H&E staining in the eWAT of STD and DIO mice. (C) The size distribution of adipocytes in the eWAT of STD and DIO mice. Data represent the mean  $\pm$  SEM ( $n = 5$ ). \*\* $P < 0.01$  compared the PBS group.

## I-3 DISCUSSION

In previous study, I showed that HABA suppressed weight gain in the HFD-induced obesity environment.<sup>17</sup> However, the exact mechanism of HABN was unknown. In this study, I detected that HABA suppressed weight gain by regulating adipogenesis and lipogenesis through CD44 in both 3T3-L1 differentiation and HFD-induced obese mice. But the anti-adipogenesis effects of HABN were not shown when HA or BA was treated alone (Figure 8). I suspect that the effects of HABA are most likely due to the HA shell exposed to the outside of the nanoparticles.

HA, an important component of ECM, is a liner glycosaminoglycan that can exist in the form of an unbranched polymer, owing to HA's nonsulfated characteristic<sup>30</sup>,<sup>31</sup>. It is a unique molecule that has both physical function<sup>32</sup> such as structure formation of ECM and biochemical functions such as cell proliferation<sup>33-35</sup>, migration<sup>36, 37</sup>, wound healing<sup>35, 38-40</sup> and inflammation<sup>39-41</sup>. In a normal environment, endogenous HAs are generally synthesized as the high molecular weight HA (HMW-HA ( $\geq 1000$  kD) and cells are surrounded by these. However, if ECM homeostasis is disrupted by an inflammatory environment is given by external or internal stimuli, cells secrete HYALs and reactive oxygen species (ROS), then HMW-HA is cleaved into LMW-HA by HYALs or ROS<sup>42-44</sup>. Thereafter, the inflammatory response is accelerated.<sup>40, 45</sup> So, HMW-HA predominates in healthy tissues<sup>32, 46</sup>. For this reason, recently, the function of HA as an immune modulator has been attracting attention, and it is mainly known that low-molecular weight HA (LMW-HA,  $\leq 500$  kD) as pro-

inflammatory function and high-molecular weight HA (HMW-HA,  $\geq 1000$  kD) as anti-inflammatory functions.<sup>43-45, 47</sup> HACN, like HMW-HA, has an anti-inflammation effect.<sup>17</sup>

Also, a group showed that 50 kDa (LMW, but not 2000 kD, 2 kD) HA has anti-adipogenesis<sup>48</sup> and anti-obesity effects.<sup>49</sup> In addition, it has been reported that HYAL treatment inhibits 3T3-L1 differentiation and HFD-induced weight gain<sup>50</sup>. These results indicate that HA plays an important role in adipocyte differentiation and weight gain. For this reason, I speculate that HACN inhibits adipocyte differentiation and weight gain by interfering with these HA functions.

Interestingly, HACN has the anti-obesity effect of LMW-HA (about 50kD) and the anti-inflammation of HMW-HA ( $\geq 1000$  kD) at the same time, and it is more stable against HYAL than endogenous HA. Although the specific mechanism of HACN remains unknown, I expect HABN to be an anti-obesity strategy targeting adipogenesis and lipogenesis.

## **Part II**

# **Hyaluronic Acid Nanoparticles as a Topical Agent for Treating Psoriasis**

## **II-1. INTRODUCTION**

Pathogenesis of psoriasis is associated with an excessively thickened skin epidermis, impaired differentiation of keratinocytes, and skin barrier dysfunction, due to increased inflammatory cell recruitment and activation in the skin.<sup>51,52</sup> Conventional approaches for psoriasis have been primarily concerned with reducing the main symptoms of psoriasis by inhibiting hyperactive inflammatory responses. At the same time, topical therapy offers a favorable option for treating psoriasis and has been extensively studied, because it is a non-invasive and self-administered method. Still, its long-term use and high-dose application can cause a variety of off-target adverse effects.<sup>53, 54</sup> Despite advances in transdermal drug delivery, conventional topical approaches remain challenging, owing to the low therapeutic or skin-penetrating efficacy of hydrophilic or larger-sized molecules and adverse effects of long-term use.<sup>53-56</sup> As a topical nanotherapeutic agent capable of addressing this unmet medical need, we investigated self-assembled hyaluronic acid nanoparticles (HANPs) that can target inflamed dermis and suppress pro-inflammatory immune responses in the skin without overt signs of local and systemic toxicity in a psoriasis mouse model.

HA, a biologically active glycosaminoglycan biopolymer mainly found in the extracellular matrix, has distinctive physicochemical and biological characteristics, including biodegradability, non-toxicity and receptor-specific binding,<sup>57-59</sup> and the potential to modulate inflammatory responses by regulating macrophages activation

via the cell-surface HA receptors including TLR2 and TLR4.<sup>60, 61</sup> In addition to these excellent characteristics, HA contains functional groups at the backbone that can be used for chemical conjugation, making it suitable to be used in various formulations such as drug-conjugates, dendrimer-conjugates, inorganic-conjugates, and self-assembled NPs.<sup>62</sup> Especially, self-assembled HANPs, consisting of the outermost hydrophilic HA layer surrounding multiple hydrophobic inner moieties, have been investigated broadly as a nanocarrier for the selective delivery of drugs to the inflammatory lesion via the HA receptors present on pro-inflammatory macrophages.<sup>14, 16, 17, 63</sup> Indeed, these HA-based drug delivery systems have been investigated in various diseases, including cancer,<sup>62</sup> atherosclerosis<sup>14, 16</sup> and skin diseases,<sup>64-68</sup> as a drug carrier to increase the amount of drug being absorbed and reaching target tissues, thereby improving therapeutic efficacy of drug while reducing side effects. In addition to their role as a drug carrier, HANPs have been explored for in vivo ultrasound imaging,<sup>69</sup> image-guided photothermal therapy,<sup>70</sup> and magnetic resonance imaging.<sup>71</sup> Recent studies have demonstrated that systemic administration of HANPs ameliorates type 2 diabetes (T2D)<sup>17, 72</sup> and osteoarthritis;<sup>73</sup> however, these studies administered HANPs in an invasive manner, and the mechanisms underlying their therapeutic value and action remain unclear.

Here, I identify the therapeutic potential of HANP as an effective topical agent to treat psoriasis. HANP can accumulate and target pro-inflammatory macrophages in the inflamed dermis after transcutaneous administration, thereby ameliorating

epidermal hyperplasia and pro-inflammatory responses in mouse models of imiquimod (IMQ)- and interleukin-23 (IL-23)-induced psoriasis-like skin dermatitis.

Finally, I identify HANP as a modulator of macrophage polarization.



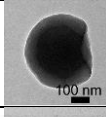
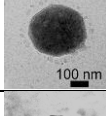
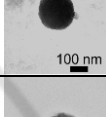
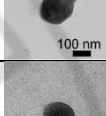
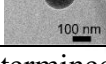
## **II-2. RESULT**

### **II-2.1 Synthesis and characterization of self-assembled HALN**

I used HA-Lithocholic acid nanoparticle (HALN) as HANP. To prepare a series of amphiphilic HA-LCA conjugates, hydrophilic 60-kDa free HAs were chemically conjugated with hydrophobic lithocholic acid (LCA, Figure 1A-C). For the conjugation reaction, aminated LCA was prepared by Fisher-Speier esterification of LCA, followed by aminolysis of ester product with ethylene diamine. By changing the molar ratio between HA and LCA during the amide coupling reaction, I successfully controlled the DS value (abbreviation for Degree of Substitution, expressed as the percentage of EtLCA molecules per repeating HA disaccharide) of HA-LCA conjugates, confirmed by  $^1\text{H-NMR}$  (Figure 1D and Table 2). The HA-LCA conjugates were dissolved in an aqueous buffer solution, inducing self-assembly of the conjugates to form HANP (HALN) via probe sonication. TEM images confirmed the self-assembly of HA-LCA conjugates in an aqueous environment to form HALNs (Figure 1A and Table 2). A negligible amount of aminated LCA remaining inside HALN was confirmed by a fluorescamine assay (Figure 2).<sup>74</sup> As the DS value increased from  $3.12 \pm 0.05$  to  $11.21 \pm 0.03$ , the hydrodynamic size of HALN decreased from  $429 \pm 43$  nm (HALN-1) to  $212 \pm 4$  nm (HALN-3, Figure 3A and Table 2), potentially resulting from the formation of a denser self-assembled nanostructure. The zeta potential increased from  $-15.74 \pm 1.96$  mV to  $-5.16 \pm 0.06$  mV depending on the hydrodynamic size of the HALN (Figure 3B and Table 2). In

addition to their colloidal stability in pH 7.4 PBS for 2 weeks (Figure 3C), HALN-3 showed a notably enhanced resistance to hyaluronidase (HYAL) degradation, compared with 60-kDa free HA (Figure 3D). Moreover, the resistance of the HALN against HYAL-mediated degradation increased as the hydrodynamic size decreased (Figure 3D), likely owing to steric hindrance from a more compact self-assembled nanostructure. Since then, HALN-3 (HALN) has been used as the basic HALN.

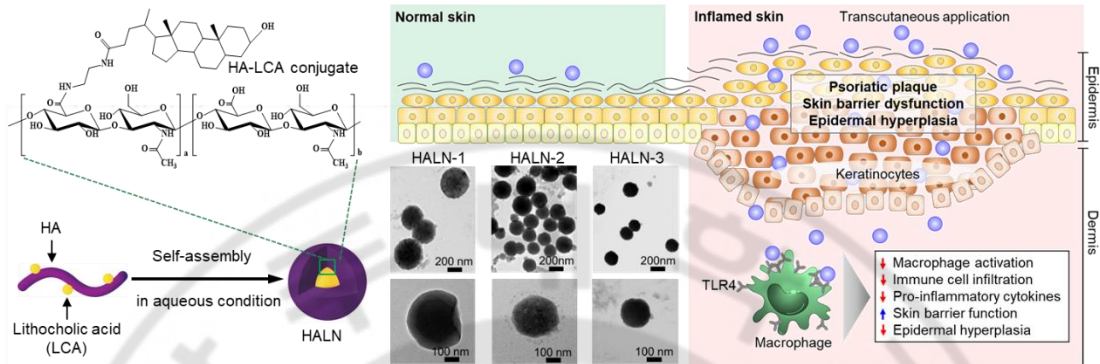
**Table 2.** Characteristics of HANPs

NP	MW of free HA	Hydrophobic moiety	Size (nm) <sup>a</sup>	$\zeta$ (mV) <sup>b</sup>	DS <sup>c</sup>	TEM image
<b>HALN-1</b>	60 kDa	LCA	429±43	-15.74±1.96	3.12±0.05	
<b>HALN-2</b>	60 kDa	LCA	332±6	-12.74±1.87	6.36±1.92	
<b>HALN-3 (HALN)</b>	60 kDa	LCA	212±4	-5.16±0.06	11.21 ± 0.03	
<b>10k-HALN</b>	10 kDa	LCA	204±15	-12.9±2.76	11.83±2.41	
<b>HACN</b>	10 kDa	CA	197±2	-8.04±0.23	2.21±0.22	

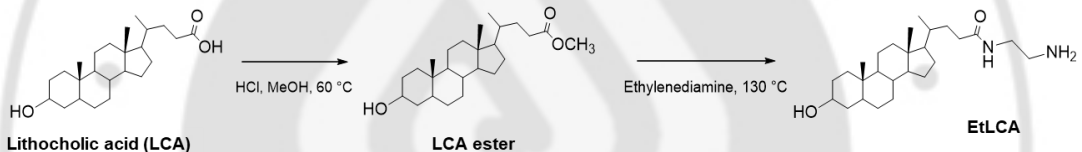
<sup>a</sup>Determined by dynamic light scattering measurement of Zetasizer, <sup>b</sup>Determined by electrophoretic light scattering measurement of Zetasizer, <sup>c</sup>Degree of substitution of CA, estimated from <sup>1</sup>H-NMR spectrum.

# Figure 1

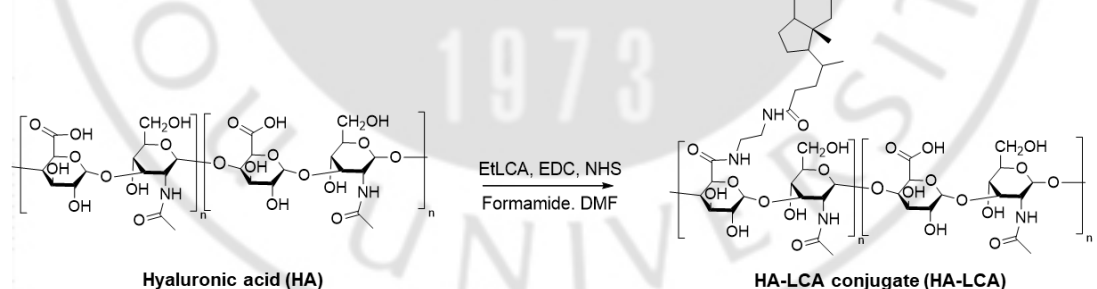
**A**



**B**



**C**



**D**

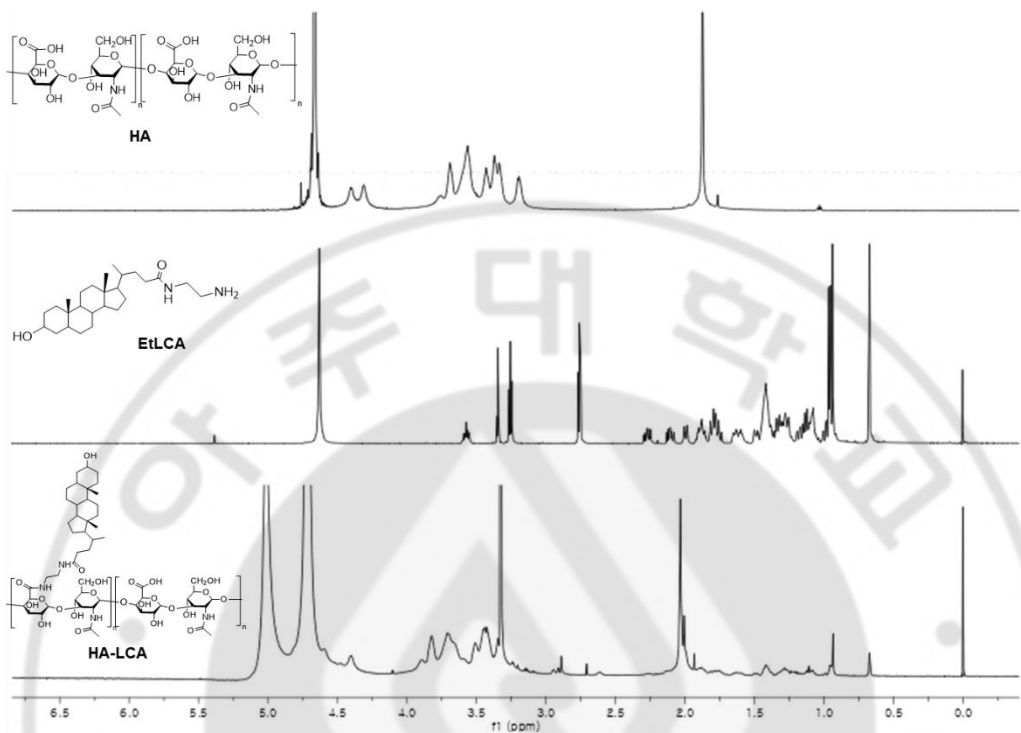


**Figure 1. Synthesis of self-assembled HALN**

(A) Chemical structure and self-assembly process of HA-LCA conjugate, and TEM images of HALNs. Scheme for the synthesis of (B) ethylenediaminated LCA (EtLCA) and (C) hyaluronic acid-lithocholic acid conjugate (HA-LCA). (D)  $^1\text{H}$  NMR spectra of hyaluronic acid (HA), EtLCA, and HA-LCA.

**Figure 2**

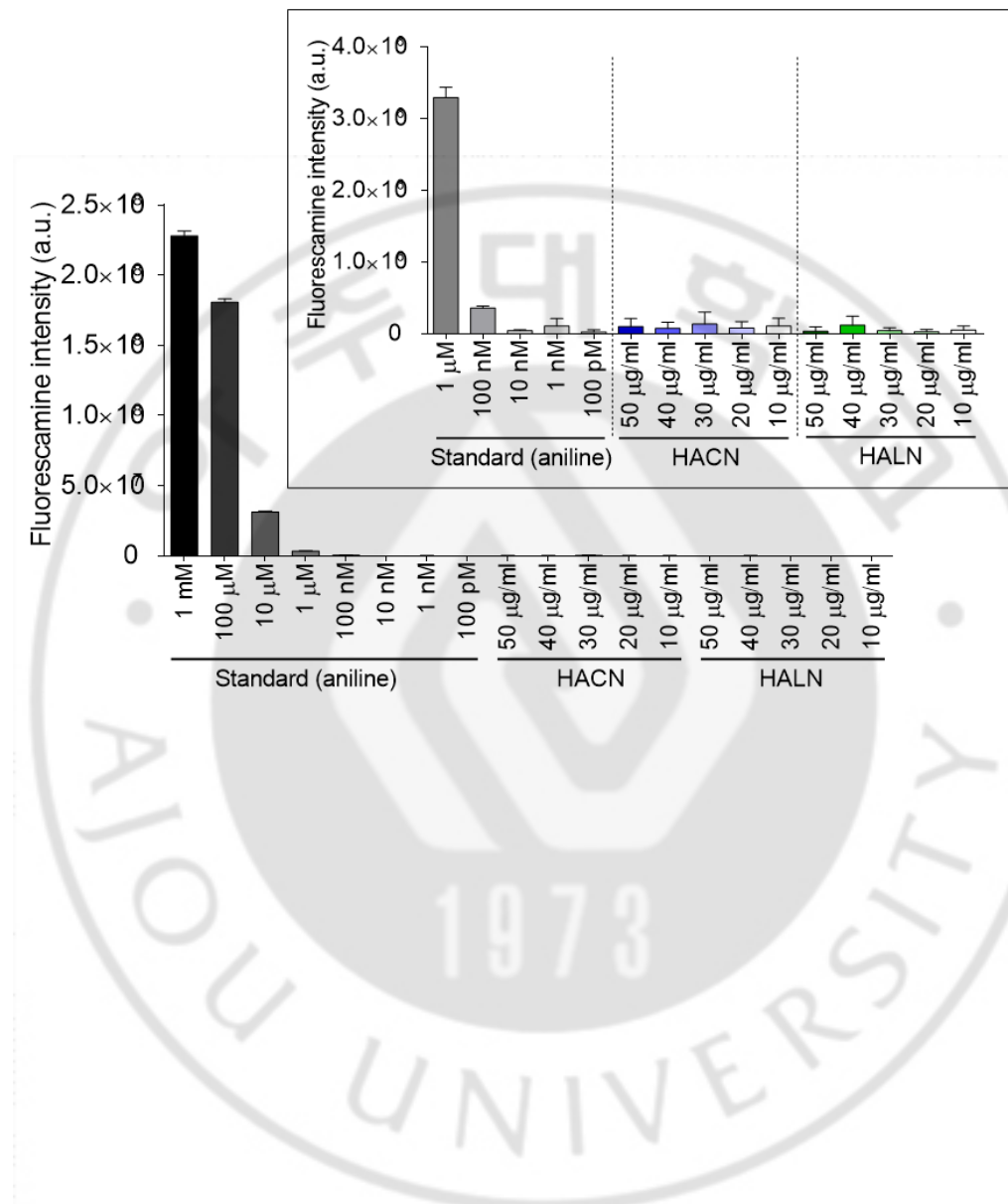


**Figure 2. Fluorescamine assay for verifying the amount of EtLCA or EtCA in HACN or in HALN.**

Amine quantification using fluorescamine assay was performed for detection of primary amine such as EtLCA and EtCA. For the calibration, a stock solution of fluorescamine (5 mg/ml) in DMSO was mixed with a solution of aniline (1000–0.1 nM) in PBS, and fluorescent intensity (ex: 382 nm, em: 480 nm) of the resulting solution was measured using plate reader (SpectraMax iD5, Molecular Devices). After the calibration, fluoresceamine assay was performed against a solution of HALN and HACN in DW (10–50 µg/ml). The final volume of the assay was 200 µl and final concentration of fluorescamine was 3 µg/ml.

**Figure 3**

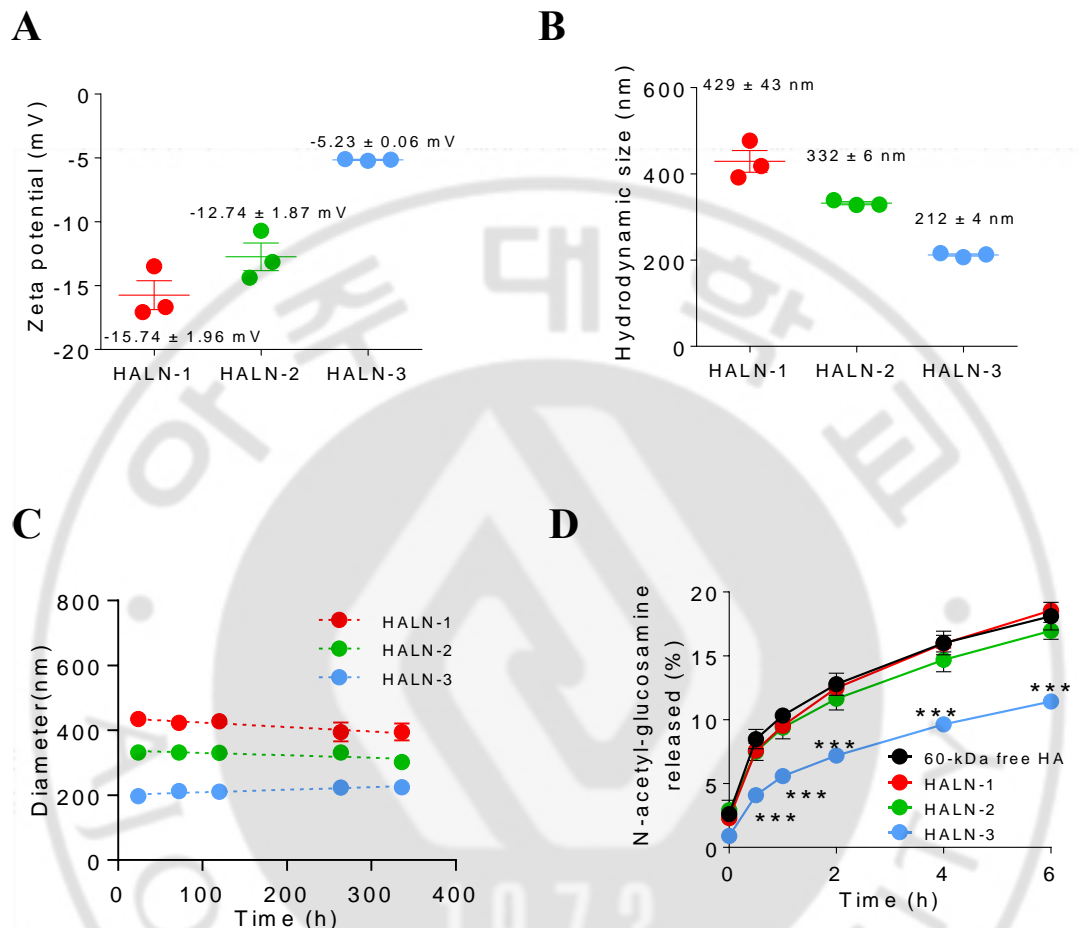


**Figure 3. Characterization of self-assembled HALN**

(A and B) Hydrodynamic sizes (A) and zeta potential values (B) of HALN-1, HALN-2, and HALN-3. (C) Time-dependent changes in the hydrodynamic size of HALN-1, HALN-2, and HALN-3 in PBS solution. (D) Amount of *N*-acetyl-glucosamine generated from 60-kDa free HA and HALNs by HYAL-II. \*\*\*P < 0.001, analyzed by two-tailed Student's t test

## **II-2.2 Therapeutic efficacy of HALN administered via the subcutaneous route in psoriasis-like skin dermatitis**

Next, I evaluated the therapeutic efficacy of an empty HALN-3 (hereinafter referred to as HALN) administered via the subcutaneous route in psoriasis-like skin dermatitis. C57BL/ 6 mice were subcutaneously administered with different doses of HALNs (5 or 20 mg/kg) daily, 2 h prior to being subjected to topical administration of 5% IMQ daily for 4 days on the shaved dorsal skin. Subcutaneously administered HALN protected the animals from IMQ-induced body weight loss and increased the clinical score of the psoriasis area and severity index (PASI) (Figure 4A–D), while suppressing epidermal hyperplasia (Figure 4E,F), macrophage infiltration (Figure 5A.B), and expression of psoriasis-associated cytokines (Figure 5D–F). LCA, the hydrophobic moiety of HALN, is a hydrophobic secondary bile acid produced by intestinal flora, and it was recently reported that intravenously administered LCA (4 mg/kg) suppresses IL-17 expression in T helper 17 ( $T_{H}17$ ) cells, thus exhibiting antipsoriatic effects.<sup>75</sup> In contrast, the most recent study demonstrated that LCA had no effects on IL-17A expression and  $T_{H}17$  cell differentiation, whereas other bile acid derivatives 3-oxoLCA and isoLCA markedly suppressed IL-17A expression and  $T_{H}17$  cell differentiation.<sup>76</sup> To investigate whether the effect of HALN is due to LCAs, I subcutaneously administered LCA (2 mg/kg, equivalent mass as in 20 mg/kg of HALN based on the DS) for four consecutive days in an

IMQ-induced psoriasis model (Figure 6A). As shown in Figure 6, LCA, in contrast to HALN, had no protective effect against psoriasis-like dermatitis caused by IMQ, suggesting that at least at the concentrations of HALNs used in my experiments, the protective effect of HALNs on psoriasis-like dermatitis is due to the presence of an outermost hydrophilic HA shell layer rather than LCAs. The effect of HALN was further confirmed in a psoriasis-like mouse model induced by IL-23. HALN (20 mg/kg), but not LCA (2 mg/kg), via an intravenous administration route showed comparable or enhanced therapeutic efficacy against IL-23 induced psoriasis-like skin dermatitis, compared with the conventional psoriasis therapeutic methotrexate (MTX) (Figure 7). Unlike conventional drugs used in the clinic, such as MTX and calcipotriene, known for adverse effects,<sup>53, 54</sup> HALN treatments did not trigger systemic toxicity or adverse effects in the major organs (Figure 8). Taken together, these results indicate that an empty self-assembled HALN itself is sufficient to protect animals against psoriasis-like skin dermatitis safely and effectively.

**Figure 4**

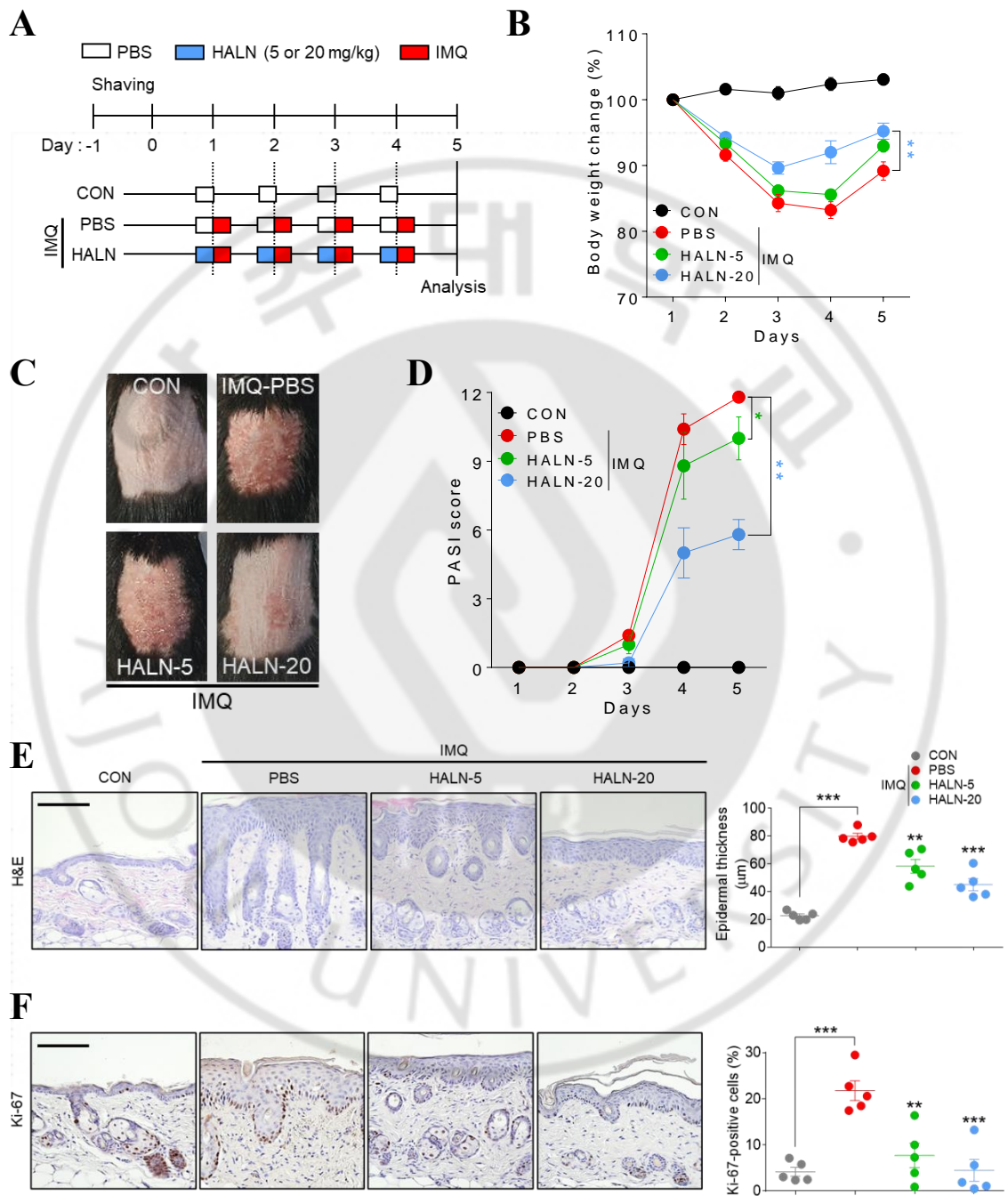
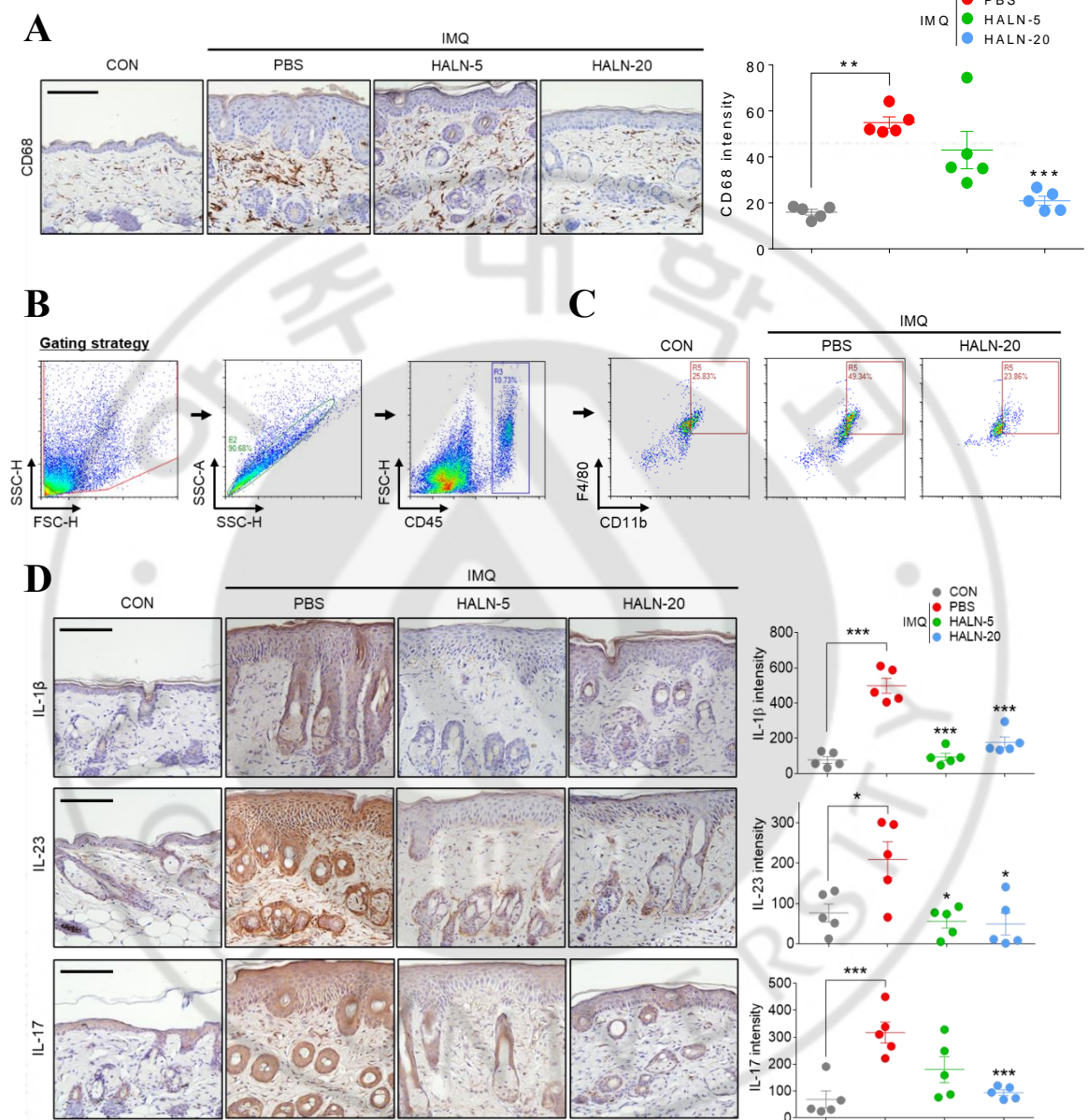


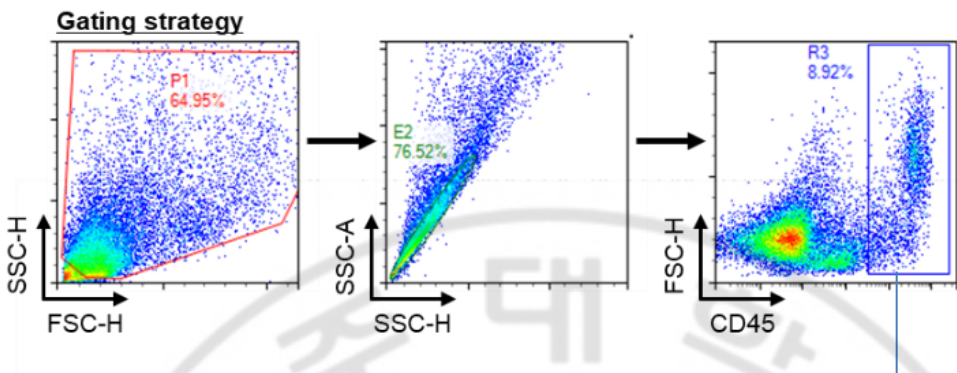
**Figure 4. Subcutaneous administration of HALN protects animals against psoriasis-like skin dermatitis induced by IMQ.**

**(A)** Experimental timeline. For four consecutive days, PBS or HALN (5 or 20 mg/kg) was subcutaneously administered into C57BL/6 mice 2 h prior to topical application of Aldara cream (5% IMQ). **(B)** Daily body weight changes. **(C)** Representative gross images of the skin on day 5. **(D)** PASI score reflecting the severity of erythema, scaling, and skin thickening for five days. **(E and F)** On day 5, the animals were euthanized, and epidermal thickness (**E**) and percentage of Ki-67-positive cells (**F**) were quantified in the epidermis of skin sections. Data are presented as mean  $\pm$  SEM ( $n = 5$  mice). \* $P < 0.05$ , \*\* $P < 0.01$ , \*\*\* $P < 0.001$ , data are analyzed by two-tailed Student's *t* test (**E, F**) or two-way ANOVA with Bonferroni's *post hoc* test (**B, D**).

# Figure 5



**E**



**F**

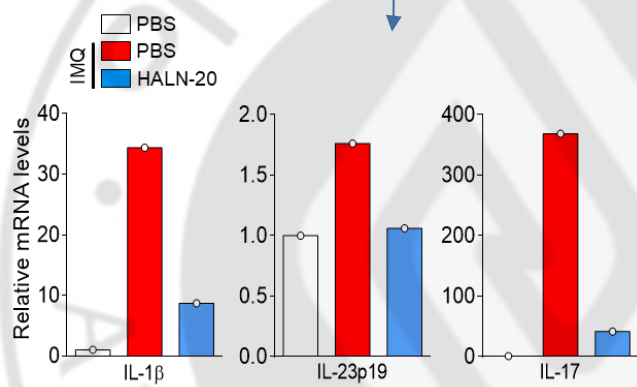
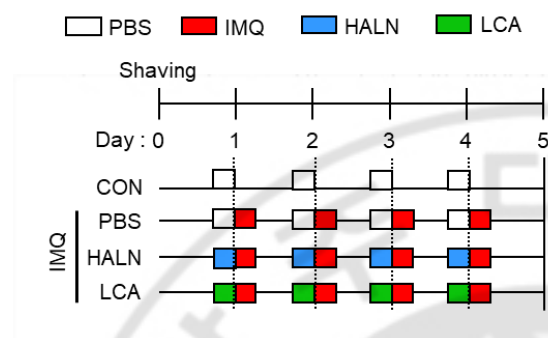


**Figure 5. Subcutaneous administration of HALN ameliorates IMQ-induced psoriasis-like skin inflammation.**

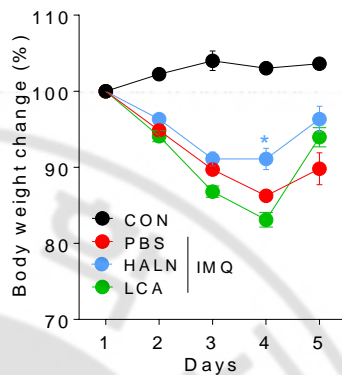
(A) Macrophage content determined by immunohistochemical staining for CD68 in the skin sections of IMQ-inflamed mice subcutaneously administered with PBS or HALN (5 or 20 mg/kg). Scale bars, 100  $\mu$ m. (B) Gating strategy for analyzing pro-inflammatory  $CD45^+F4/80^+CD11b^+$  macrophages in the skin of each group using flow cytometry. (C) Frequencies of pro-inflammatory  $CD45^+F4/80^+CD11b^+$  macrophages. Cells isolated from the skins of 5 mice per each group were pooled and analyzed by flow cytometry. (D) Expression patterns determined by immunohistochemical staining for IL-1 $\beta$ , IL-23 and IL-17 in skin sections of each group. Scale bars, 100  $\mu$ m. (E) Gating strategy for isolating  $CD45^+$  cells from the skin of each group using flow cytometry. (F) mRNA levels of IL-1 $\beta$ , IL-23 and IL-17 in  $CD45^+$  cells isolated from the skin tissues of each group. Cells isolated from the skin tissues of 5 mice per group were pooled and analyzed by qPCR. Data are presented as mean  $\pm$  SEM (n = 5 mice per group). \*P < 0.05, \*\*P < 0.01, \*\*\*P < 0.001, analyzed by two-tailed Student's t test.

**Figure 6**

**A**



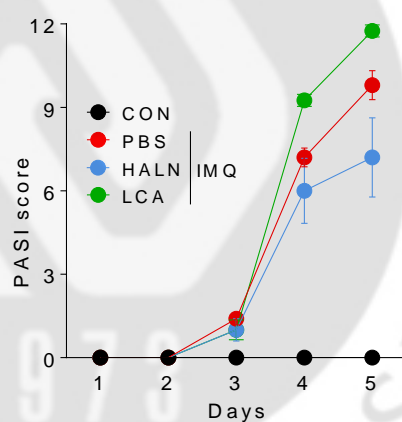
**B**



**C**



**D**



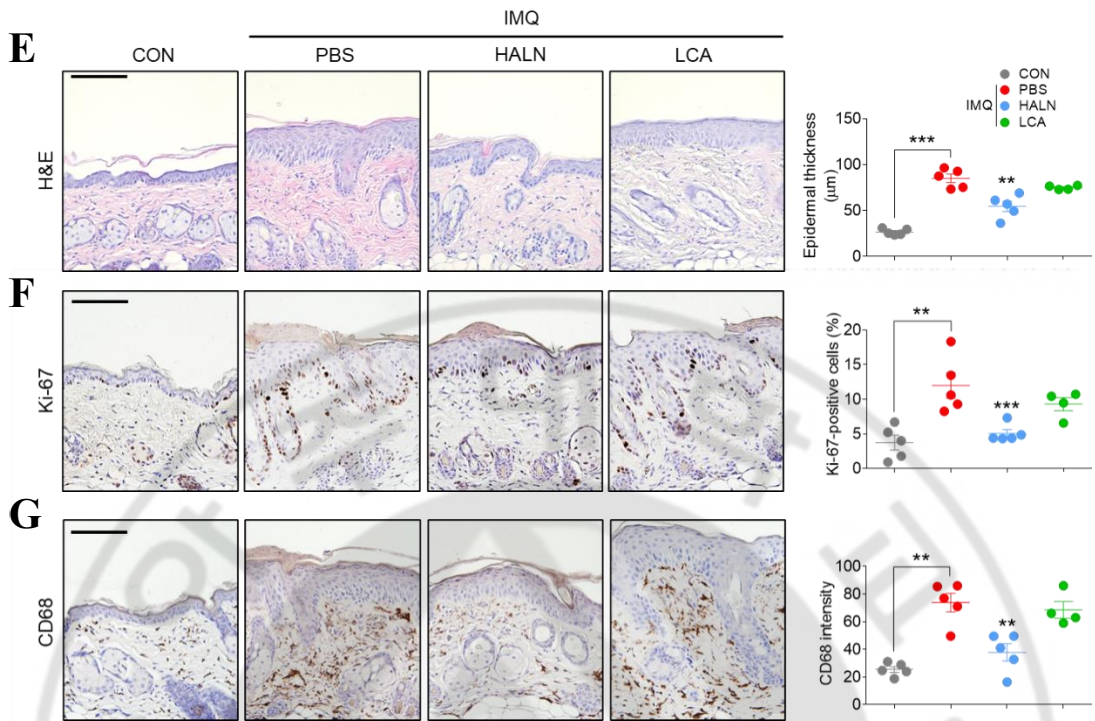
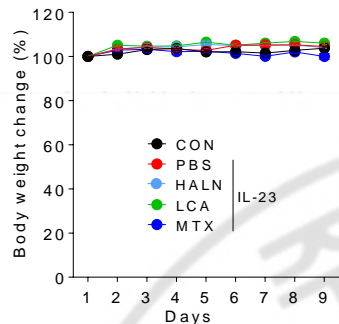


**Figure 6. Effects of subcutaneously administered LCA on IMQ-induced psoriasis-like skin dermatitis.**

(A) Experimental timeline. For 4 consecutive days, PBS, HALN (20 mg/kg), or LCA (2 mg/kg, equivalent mass as in 20 mg/kg of HALN based on the DS) was subcutaneously administered into the shaved dorsal skin of C57BL/6 mice 2 h prior to topical application of Aldara cream (5% IMQ). (B) Daily bodyweight changes in each group for 5 days. (C) Representative gross images of the skin on day 5. (D) PASI score reflecting the severity of erythema, scaling, and skin thickening for 5 days. (E and F) On day 5, animals were euthanized, and epidermal thickness (E) and the percentage of Ki-67-positive cells in epidermis (F) were quantified in skin sections from each group. Scale bars, 100  $\mu$ m. (G) Expression patterns determined by immunohistochemical staining for CD68 in skin sections of each group. Scale bars, 100  $\mu$ m. Data are presented as mean  $\pm$  SEM ( $n = 4\text{--}5$  mice per group). \* $P < 0.05$ , \*\* $P < 0.01$ , \*\*\* $P < 0.001$ , analyzed by two-tailed Student's t test.

**Figure 7**

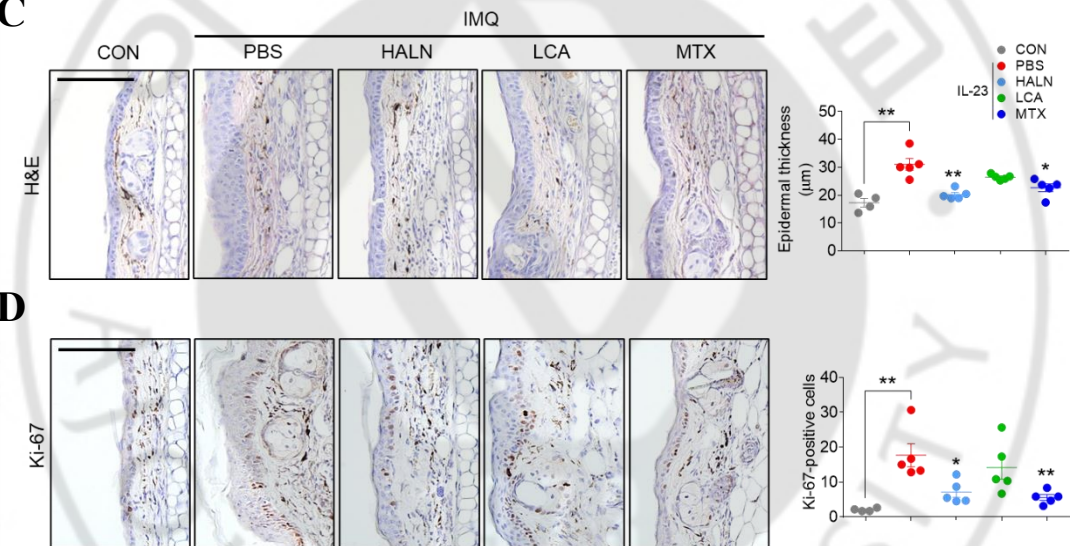
**A**



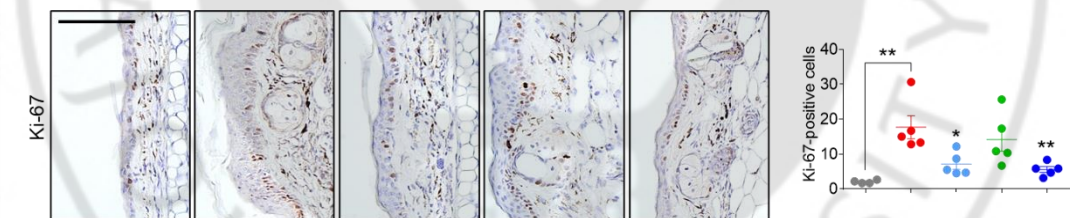
**B**

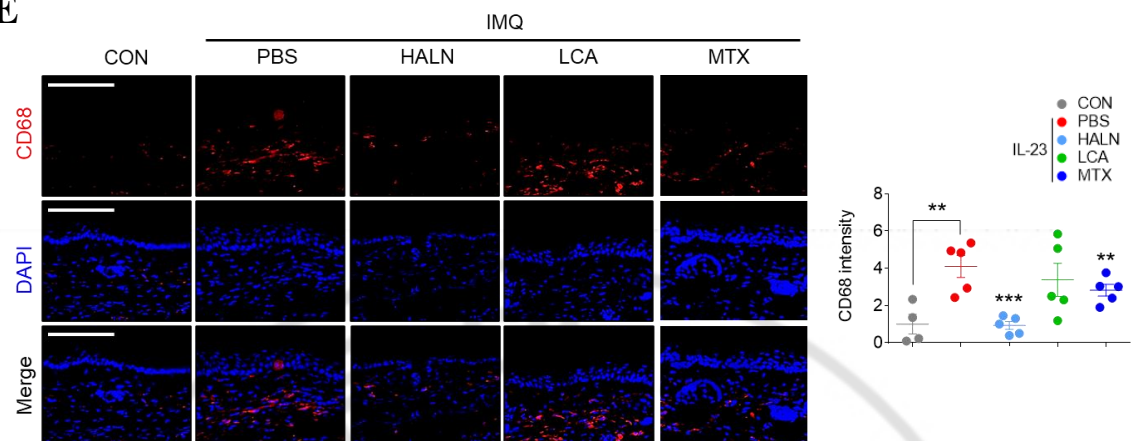


**C**



**D**



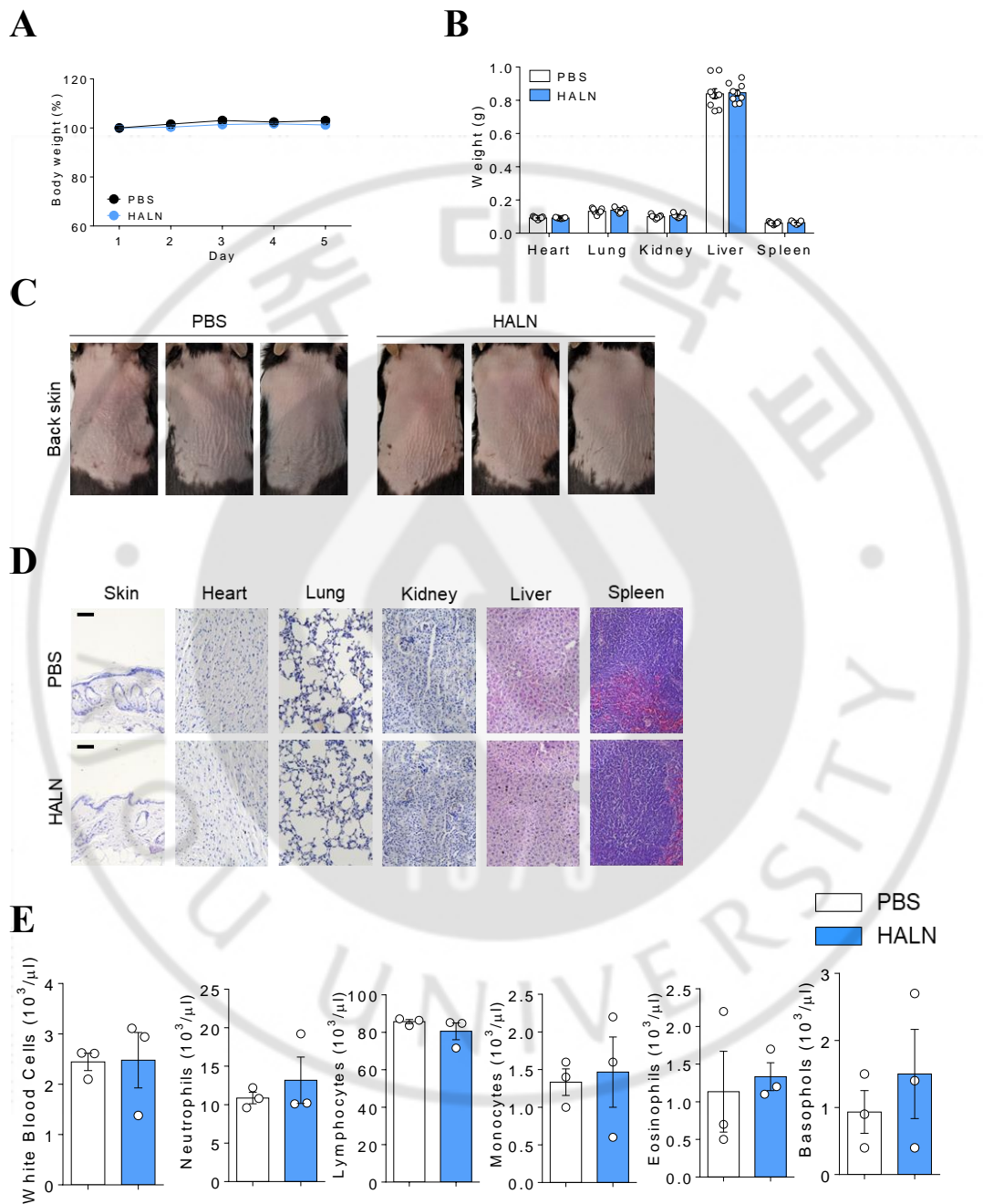
**E**

**Figure 7. Effects of HALN, LCA, and MTX on IL-23-induced psoriasis-like skin dermatitis.**

For 8 consecutive days, PBS, HALN (20 mg/kg), LCA (2 mg/kg), or MTX (10 mg/kg) was intravenously administered into the tail vein of C57BL/6 mice 2 h prior to intradermal injection of IL-23 (500 ng). (A) Daily bodyweight changes in each group for 9 days. (B) Representative gross images of the ear on day 9. (C and D) On day 9, animals were euthanized, and epidermal thickness (C) and the number of Ki-67-positive cells in epidermis (D) were quantified in ear sections from each group. Scale bars, 100  $\mu$ m. (E) Expression patterns determined by immunohistochemical staining for CD68 in ear sections of each group. DAPI was used for nuclei counter staining. Scale bars, 100  $\mu$ m. Data are presented as mean  $\pm$  SEM ( $n = 4\text{--}5$  mice per group).

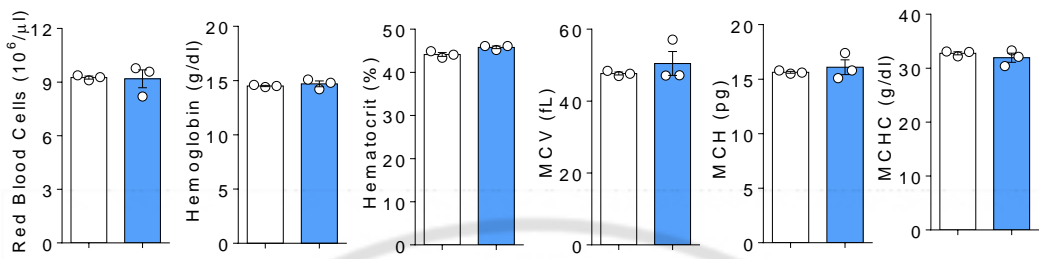
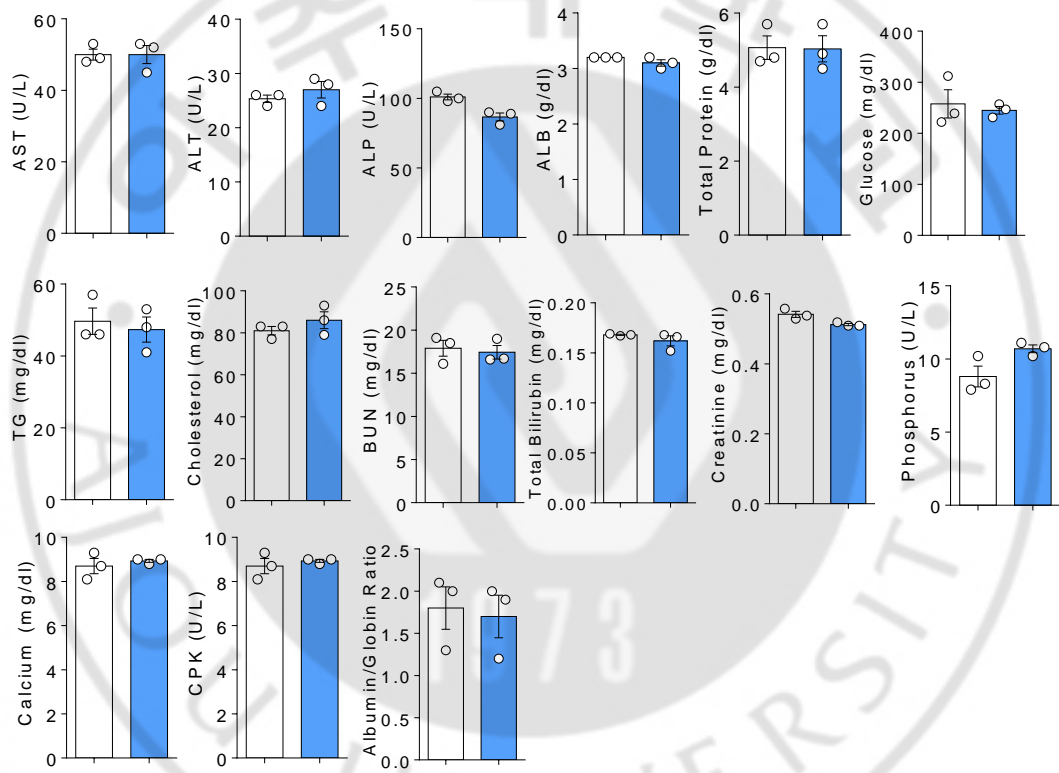
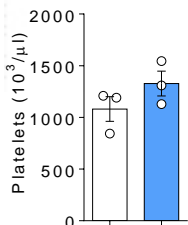
\* $P < 0.05$ , \*\* $P < 0.01$ , \*\*\* $P < 0.001$ , analyzed by two-tailed Student's t test.

**Figure 8**



**F**

PBS  
HALN

**G****H**

### **Figure 8. Safety profiles of HALN**

C57BL/6 mice were subcutaneously administered with PBS or HALN (20 mg/kg) for 5 consecutive days. On day 5, animals were euthanized, and blood and major organs were collected for histology, blood hematology, and blood chemistry analysis. **(A)** Daily bodyweight changes in each group for 5 days. **(B)** Weights of major organs in each group on day 5. **(C)** Representative gross images of the skin on day 5. Scale bars, 200  $\mu$ m. **(D)** Representative images of major organ sections stained with hematoxylin and eosin (H&E) on day 5. **(E-H)** Blood hematology and blood chemistry in each group on day 5. Levels of **(E)** white blood cells, **(F)** red blood cells and heme regulation. **(G)** function of liver and kidney and **(H)** level of platelet. Bloods were pooled from 2 mice for analysis. Data are presented as mean  $\pm$  SEM ( $n = 9$  mice per group for A-D and  $n = 6$  mice per group for E-H).

## **II-2.3. Accumulation of Transcutaneously Administered HALN in IMQ-Inflamed Dermis**

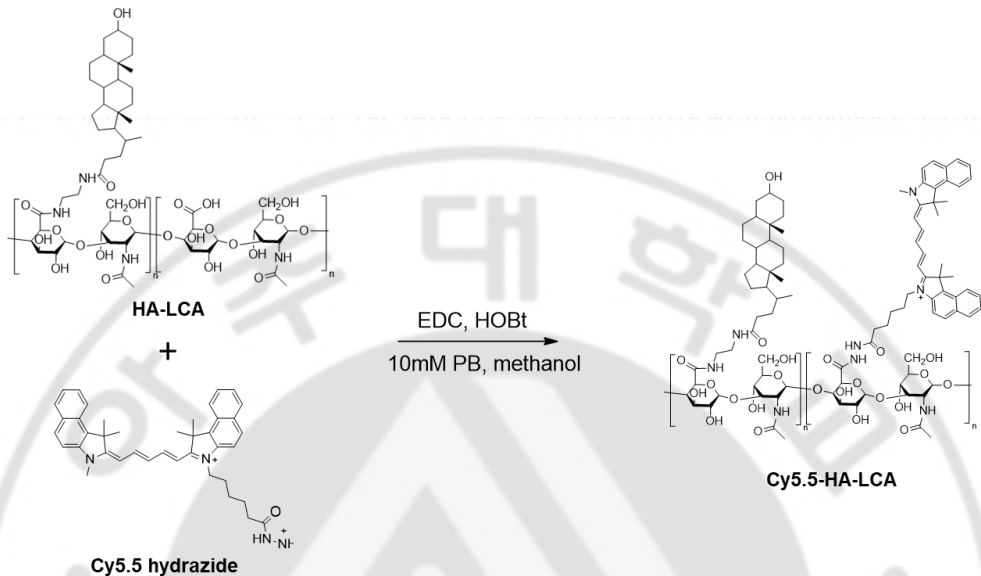
To examine skin penetration of HALN after transcutaneous application, I synthesized Cy5.5-conjugated HALN (Cy5.5-HALN, Figure 9A) and performed Franz diffusion cell (FDC) experiments using shaved dorsal skins collected from normal or IMQ-inflamed mice. Cy5.5-HALN exhibited proficient penetration through dorsal skins, and compared with normal dermis, the fluorescence signal of Cy5.5-HALN was observed faster and more robustly in IMQ-inflamed dermis (Figure 9B). For better visualization of Cy5.5-HALN's skin-penetrating ability, the shaved dorsal skins of normal and IMQ-inflamed mice after transcutaneous administration of Cy5.5-HALNs were analyzed under two-photon microscopy. Compared to normal mice skin, IMQ-inflamed skin revealed a greater and faster Cy5.5 signal in deeper skin layers (Figure 10A). Z-projection data from 6 to 48  $\mu\text{m}$  in IMQ-inflamed skin showed that, compared with Cy5.5-HA, Cy5.5-HALNs accumulated more in deeper layers of the skin (Figure 10B,C), indicating the efficient skin-penetrating ability of HALN. Moreover, confocal microscopic analysis showed that transcutaneously administered Cy5.5-HALNs on the shaved dorsal skin were accumulated and associated with CD68 $^{+}$  macrophages in the dermis of IMQ-inflamed mice; however, Cy5.5-HALN accumulation and association with CD68 $^{+}$  macrophages in the dermis were detected much less in disease-free normal mice than in IMQ-inflamed mice (Figure 10D). When Cy5.5-HALN was incubated with M0, M1, or M2 RAW 264.7

cells, strong Cy5.5-HALN signals were detected in pro-inflammatory M1 macrophages. In contrast, minimal signals were observed in conventional M0 or M2 macrophages (Figure 11A). The HALN signal in pro-inflammatory M1 macrophages was markedly inhibited by either siRNA or antibody against TLR4 (Figure 11B,C), suggesting TLR4-mediated targeting of HALN to pro-inflammatory M1 macrophages. Additionally, I confirmed *in vivo* skin penetration ability of HALN-1,2,3 on the shaved dorsal skin of normal and IMQ-inflamed mice; this experiment also revealed that the skin-penetrating ability of Cy5.5-HALN increases from HALN-1 to HALN-3 as the hydrodynamic size decreases (Figure 12), and Cy5.5- HALN-3 was not detected in any of the major organs tested, except for the skin (Figure 13).

To further confirm skin penetration of HANPs, I employed HACN, another HANP consisting of 10 kDa free HA and 5 $\beta$ -cholanic acid (CA), as indicated by  $^1\text{H}$  NMR and TEM (Figures 14 and Table 2). The DS value, hydrodynamic diameter, and zeta potential of HACN were  $2.21 \pm 0.22$ ,  $197 \pm 2$  nm, and  $-8.04 \pm 0.23$  mV, respectively (Table 2), and a fluorescamine analysis confirmed that the amount of aminated CA remaining inside HACN was negligible (Figure 2). Additionally, the skin penetrating ability of Cy5.5-conjugated HACN (Cy5.5-HACN, Figure 15A) was comparable with that of Cy5.5-HALNs, as shown by confocal and two-photon microscopic analysis after transcutaneous administration of Cy5.5-HACN on the shaved dorsal skins of normal and IMQ-inflamed mice (Figure 15B-C).

**Figure 9**

**A**



**B**

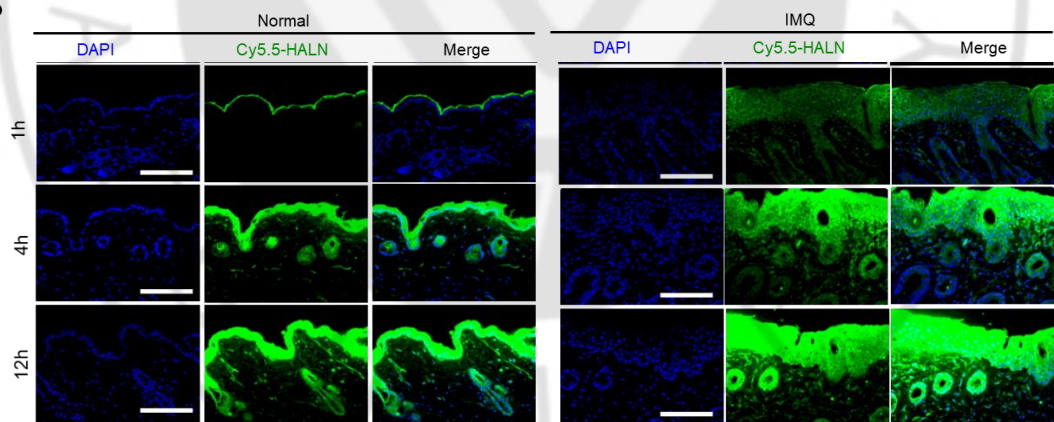
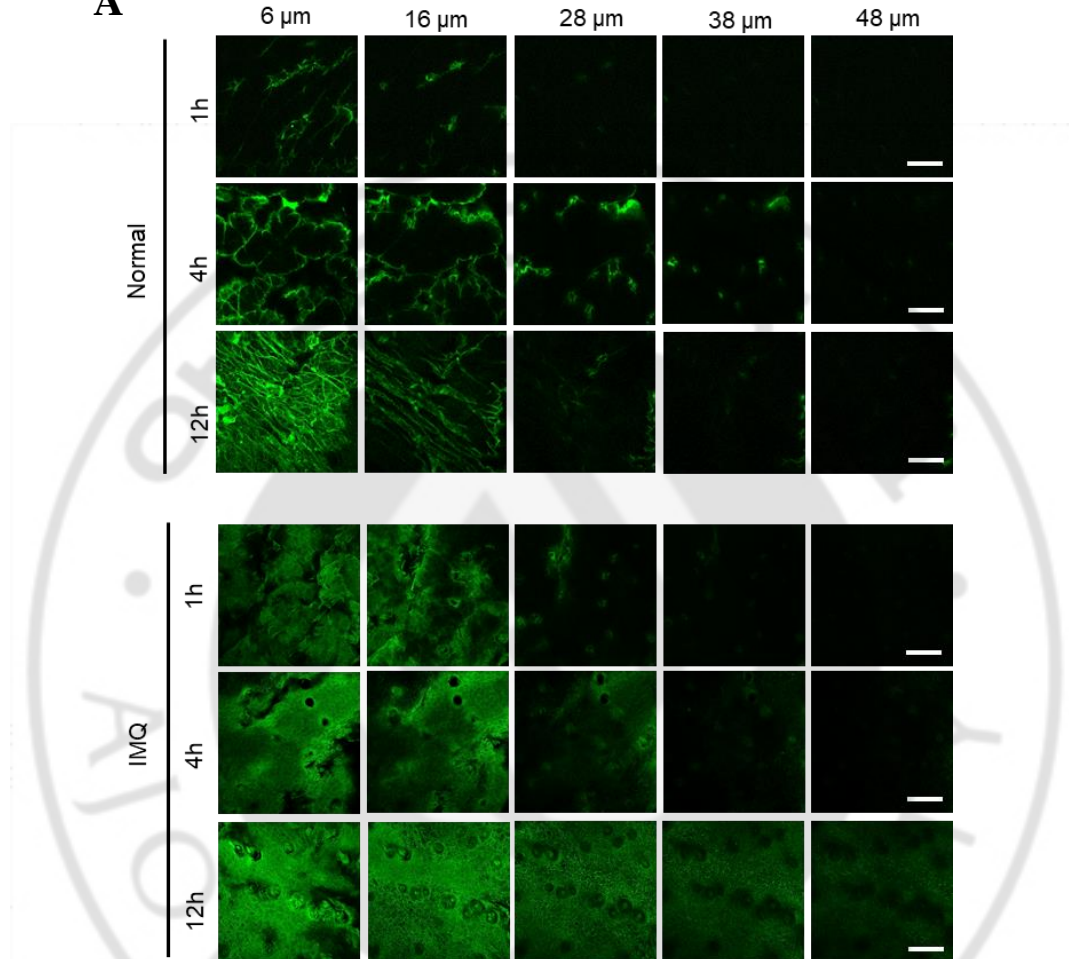


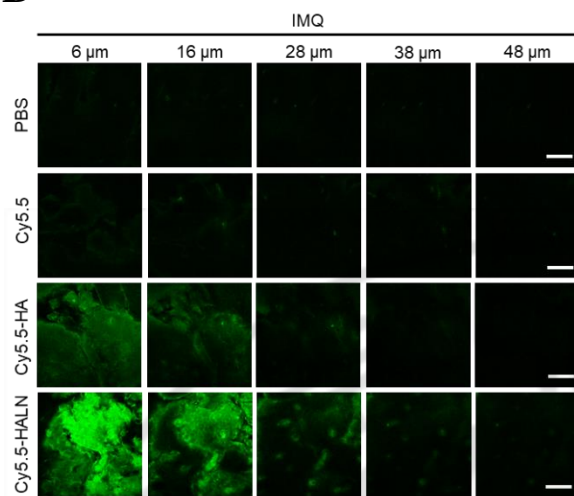
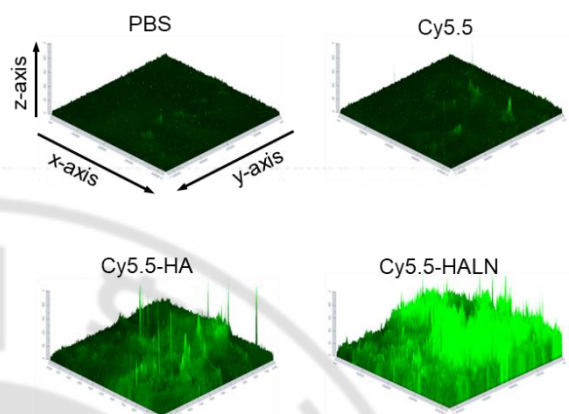
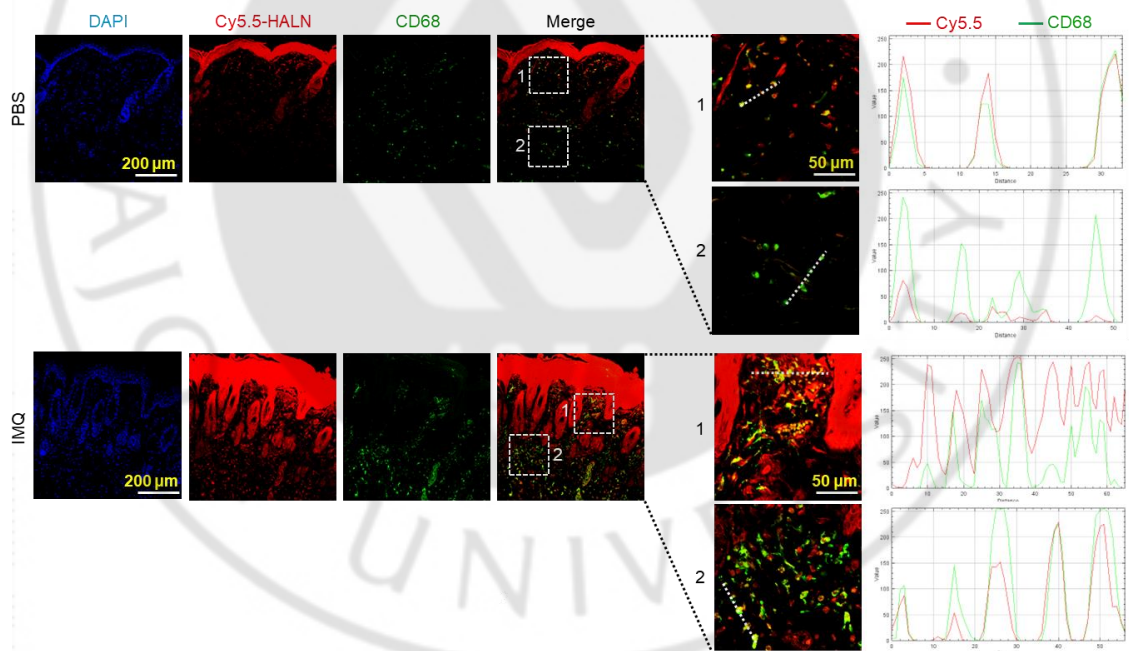
**Figure 9. Ex vivo skin penetration of Cy5.5-HALN**

(A) Scheme for the synthesis of Cy5.5-HA-LCA. (B) Skin penetration profiles of Cy5.5-HALN in the skin sections of normal and IMQ-inflamed mice. PBS or Aldara cream (5% IMQ) was topically applied on the shaved dorsal skins of C57BL/6 mice for 4 consecutive days. On day 5, the shaved dorsal skin tissues were excised and used in the FDC with Cy5.5-HALN (20 mg/ml). DAPI was used for nuclei counter staining. Scale bars, 100  $\mu$ m.

**Figure 10**

**A**



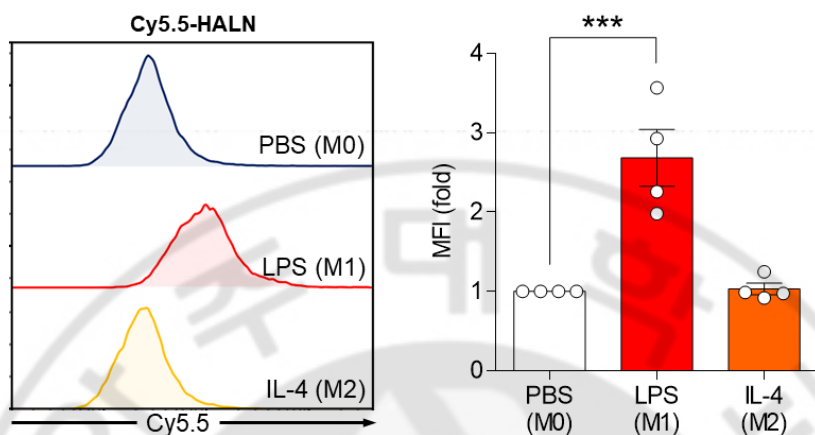
**B****C****D**

**Figure 10. Transcutaneously administered HALN localizes in IMQ-inflamed dermis**

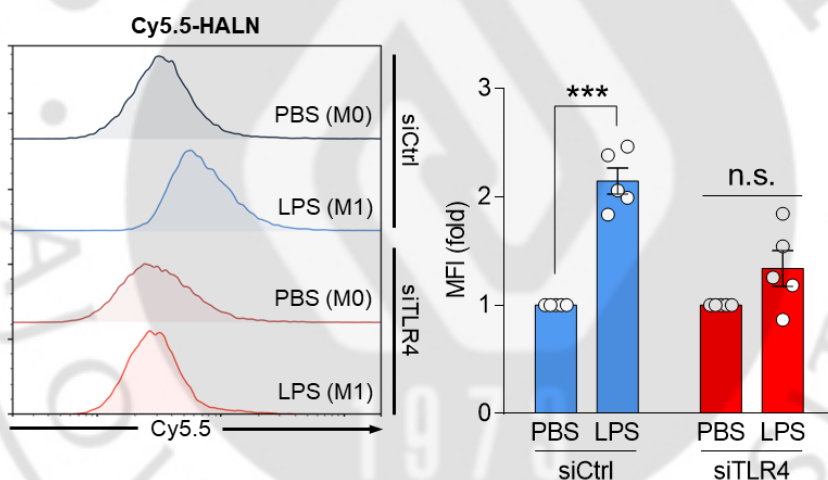
For four consecutive days, PBS or 5% IMQ was topically administered on the shaved dorsal skins. On day 5, PBS, 2 mg/cm<sup>2</sup> of Cy5.5-HALN, Cy5.5, or Cy5.5-HA (equivalent dose of Cy5.5) was administered on the shaved dorsal skin tissues in the FDC, and skin tissues were analyzed using two-photon microscopy (**A-C**) or confocal microscopy (**D**). **(A)** Optical serial sections of images from normal and IMQ-inflamed mice at 10 µm intervals below the skin surface. **(B)** Comparison of transcutaneous skin penetration efficiencies of Cy5.5, Cy5.5-HA, and Cy5.5-HALN through IMQ-inflamed skin tissues using a two-photon microscopy. **(C)** Three-dimensional view of the IMQ-inflamed skin sections transcutaneously applied with PBS, Cy5.5 only, Cy5.5-HA, and Cy5.5-HALN. **(D)** Accumulation of Cy5.5-HALN in CD68<sup>+</sup> macrophages within IMQ-inflamed skins. Normal and IMQ-inflamed skin sections transcutaneously applied with Cy5.5-HALN were stained with anti-CD68 antibody and visualized by confocal microscopy. DAPI was used for nuclei counter staining.

**Figure 11**

**A**



**B**



**C**

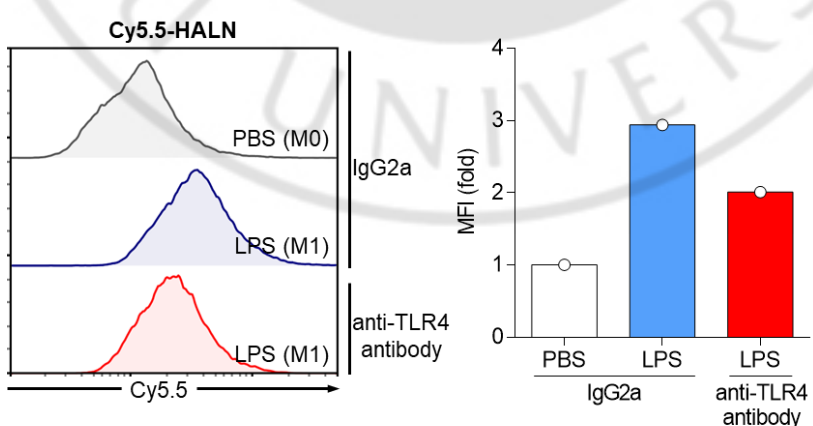


**Figure 11. TLR4-mediated association of Cy5.5-HALN with M1 macrophages**

(A) Flow cytometry analysis of Raw264.7 cells pre-treated for 24 h with PBS, LPS (1 µg/ml) or IL-4 (20 ng/ml), followed by incubation with Cy5.5-HALN (10 µg/ml) for 10 min. (B) Flow cytometry analysis of control (siCtrl) or TLR4 siRNA (siTLR4)-transfected Raw264.7 cells pre-treated for 24 h with PBS or LPS (1 µg/ml), followed by 1 h incubation with Cy5.5-HALN (10 µg/ml). (C) Flow cytometry analysis of Raw264.7 cells pre-treated for 24 h with PBS or LPS (1 µg/ml) and incubated with IgG2a (10 µg/ml) or anti-TLR4 antibody (10 µg/ml) for 1 h, followed by treatment with Cy5.5-HALN (10 µg/ml) for 10 min. Data are presented as mean ± SEM (n = 4 independent samples for A and B). \*\*\*P < 0.001, analyzed by two-tailed Student's t test. n.s., not significant.

**Figure 12**

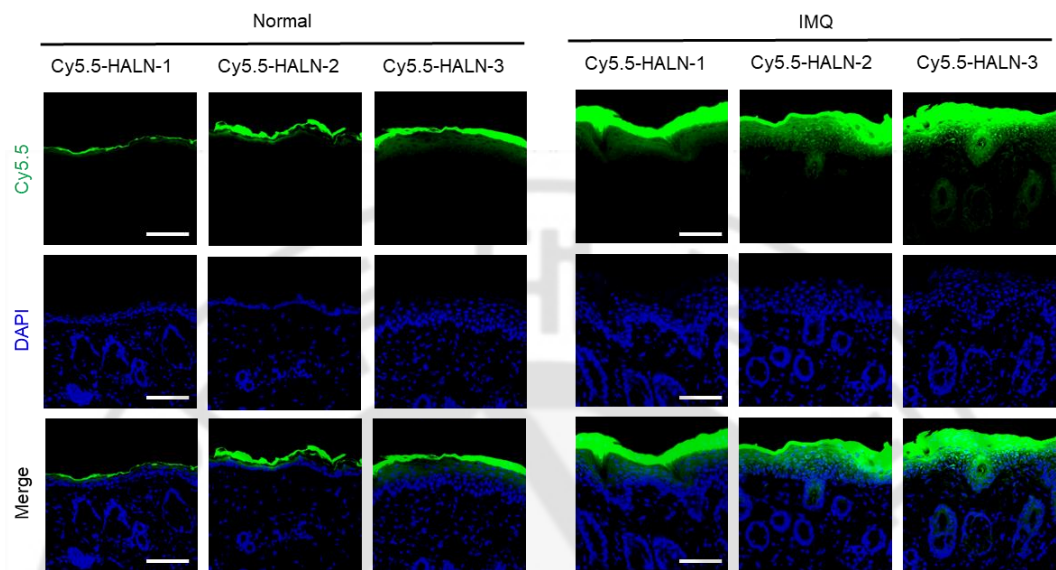


**Figure 12. In vivo skin penetration efficiency of Cy5.5-HALN-1, Cy5.5-HALN-2, and Cy5.5-HALN-3**

A total of 1 mg/cm<sup>2</sup> of Cy5.5-HALNs (HALN-1, HALN-2, or HALN-3, equivalent mass of Cy5.5) was transcutaneously administered on the shaved dorsal skin of normal and IMQ-inflamed mice for 4 h. DAPI was used for nuclei counter staining.

Scale bars, 100 μm.

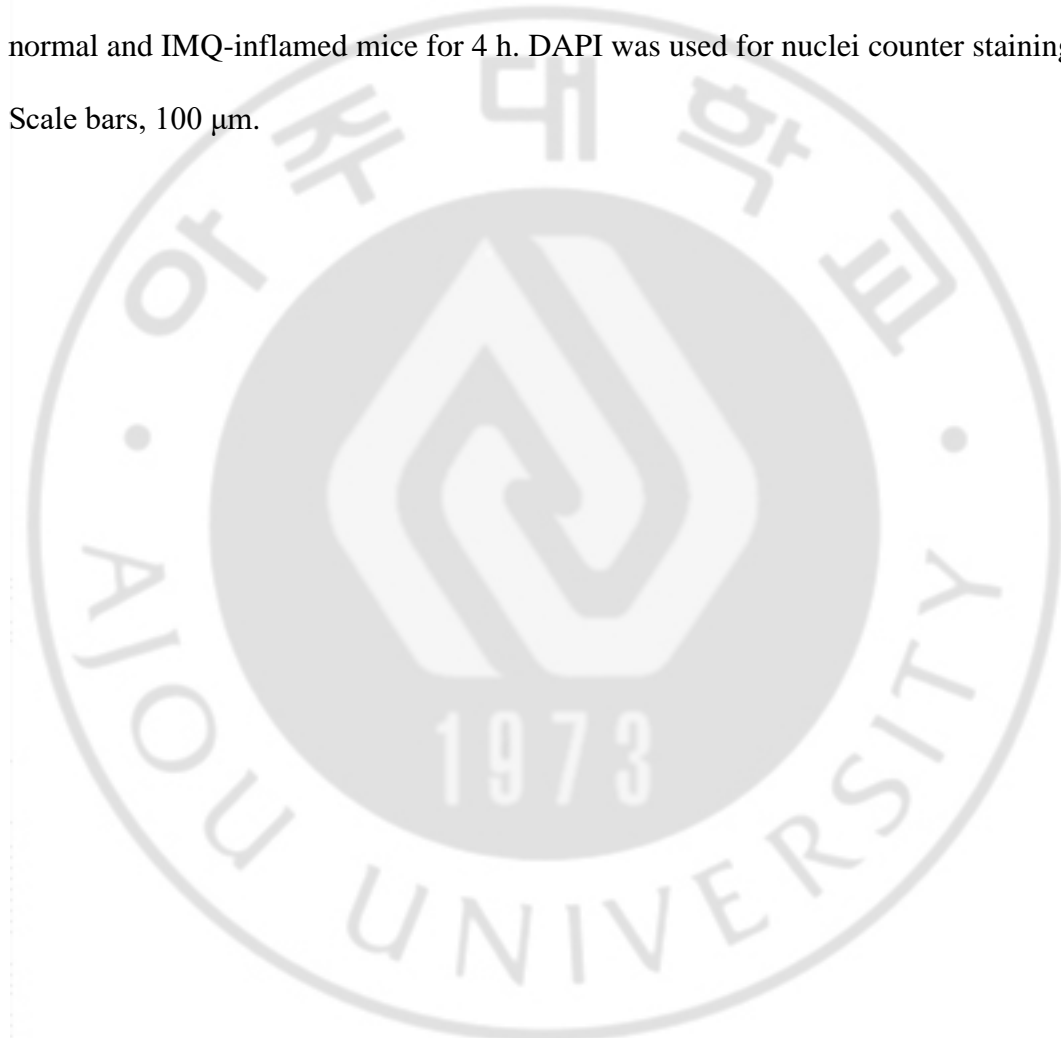


**Figure 13**

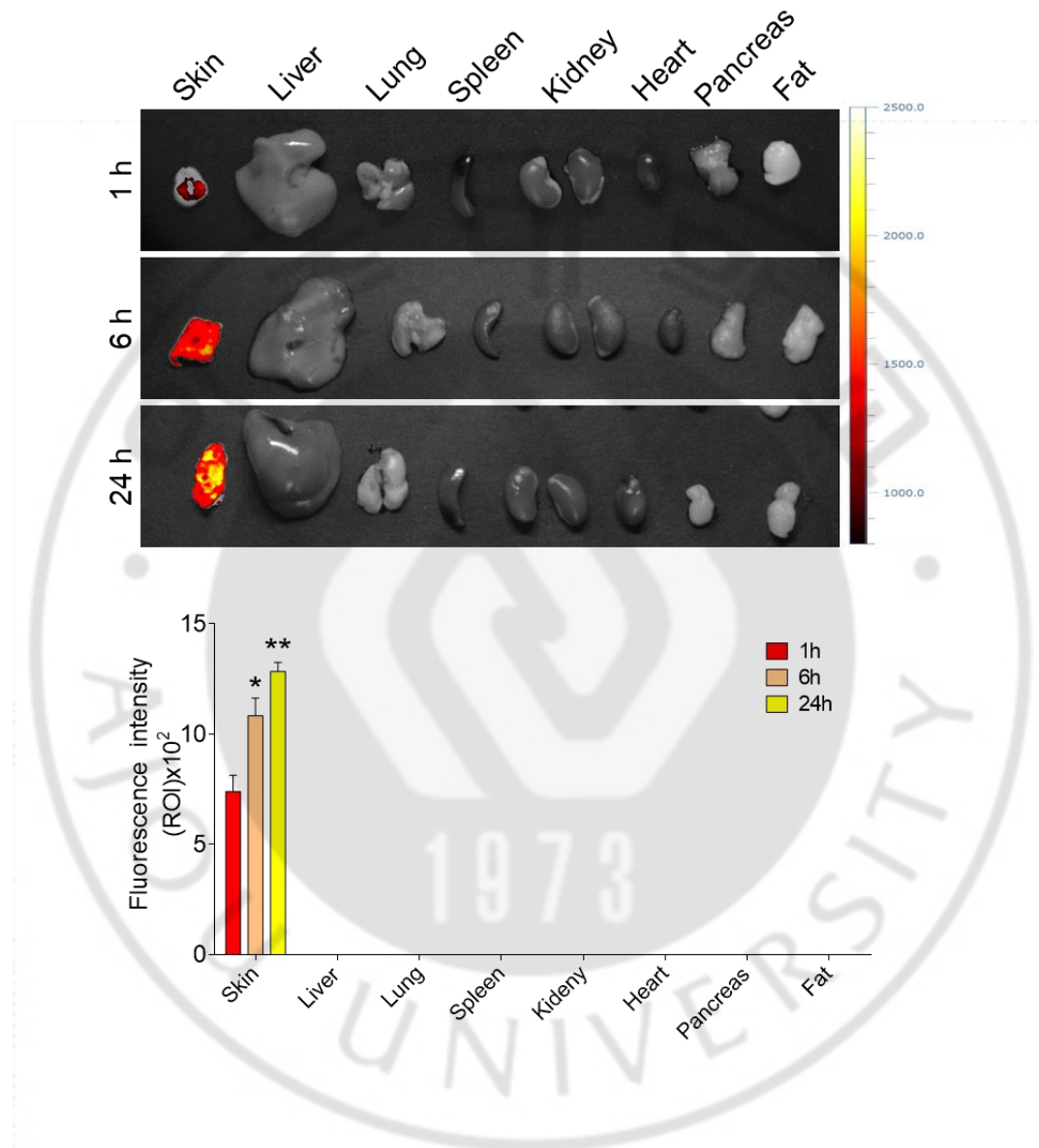
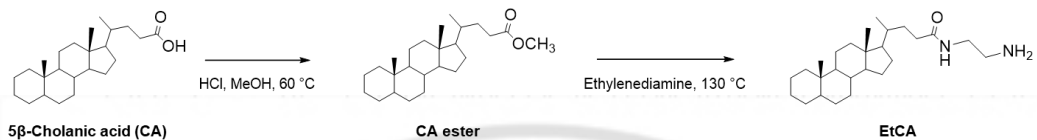


**Figure 13. Ex vivo biodistribution of transcutaneously administered Cy5.5-  
HALN**

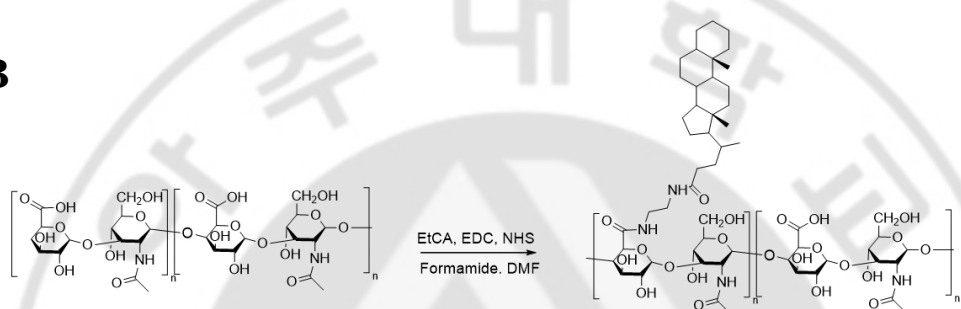
Cy5.5-HALN (1 mg/cm<sup>2</sup>) were transcutaneously administered on the shaved dorsal skin of C57BL/6 mice and the major organs (skin, liver, lung, spleen, kidney, heart, pancreas, and fat) excised at pre-determined time points were analyzed for the time-dependent signal intensity of Cy5.5-HALN. Data are presented as mean ± SD (n = 3 mice per group). \*P < 0.05, \*\*P < 0.01, analyzed by two-tailed Student's t test.

**Figure 14**

**A**



**B**



**C**

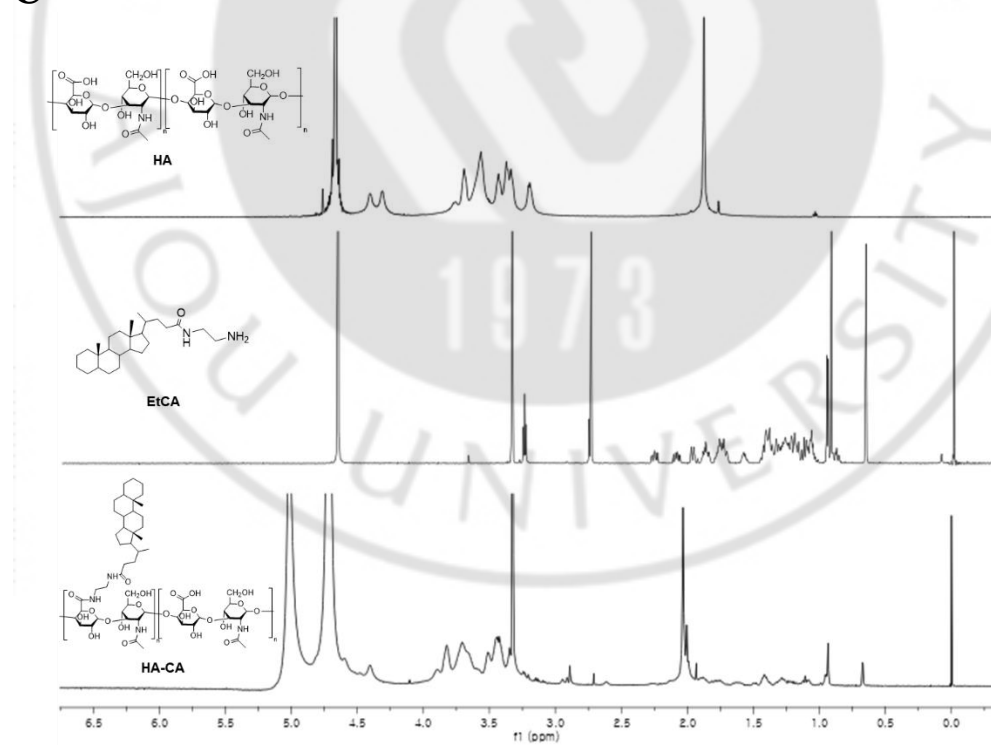


**Figure 14. The synthesis of HACN**

Scheme for the synthesis of (A) ethylenediaminated CA (EtCA) and (B) HA- $5\beta$ -cholanic acid conjugate (HA-CA). (C)  $^1\text{H-NMR}$  spectra of HA, EtCA, and HA-CA.



**Figure 15**

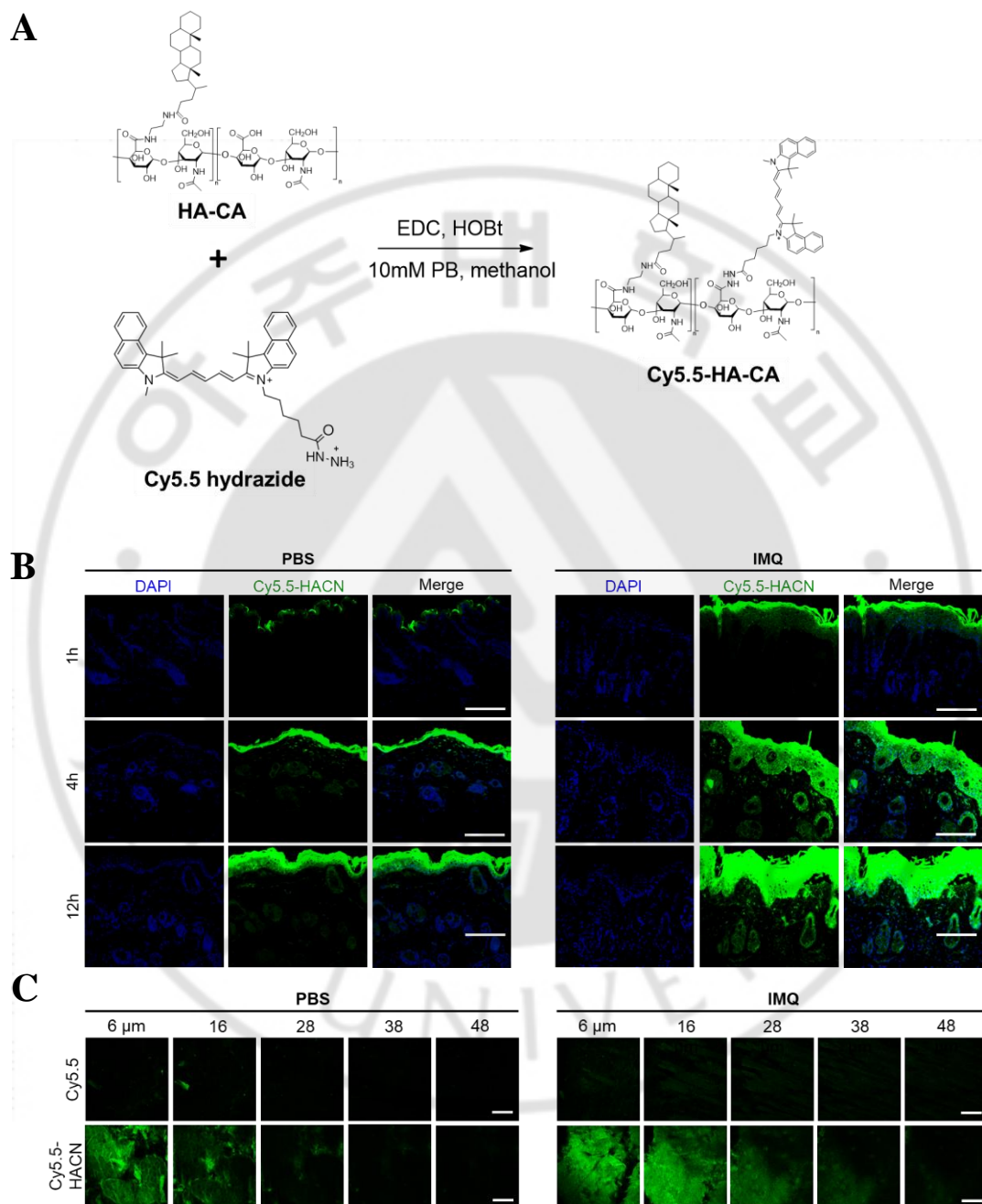


**Figure 15. Ex vivo skin penetration efficiency of Cy5.5-HACN**

(A) Scheme for the synthesis of Cy5.5-HA-CA. (B and C) PBS or Aldara cream (5% IMQ) was topically applied on the shaved dorsal skins of C57BL/6 mice for 4 consecutive days. On day 5, 2 mg/cm<sup>2</sup> of Cy5.5-HACN was applied on the shaved dorsal skin tissues in the FDC and images were acquired using a confocal microscopy (B) or two-photon microscopy (C). (B) Skin penetration profiles of Cy5.5-HACN in the skin sections of normal and IMQ-inflamed mice. DAPI was used for nuclei counter staining. Scale bars, 50 μm. (C) Optical serial sections of images from normal and IMQ-inflamed skins at intervals of 10 or 12 μm below the skin surface. Scale bars, 100 μm.

## **II-2.4. Efficacy of Transcutaneously Administered HALNs against Psoriasis-like Skin Dermatitis**

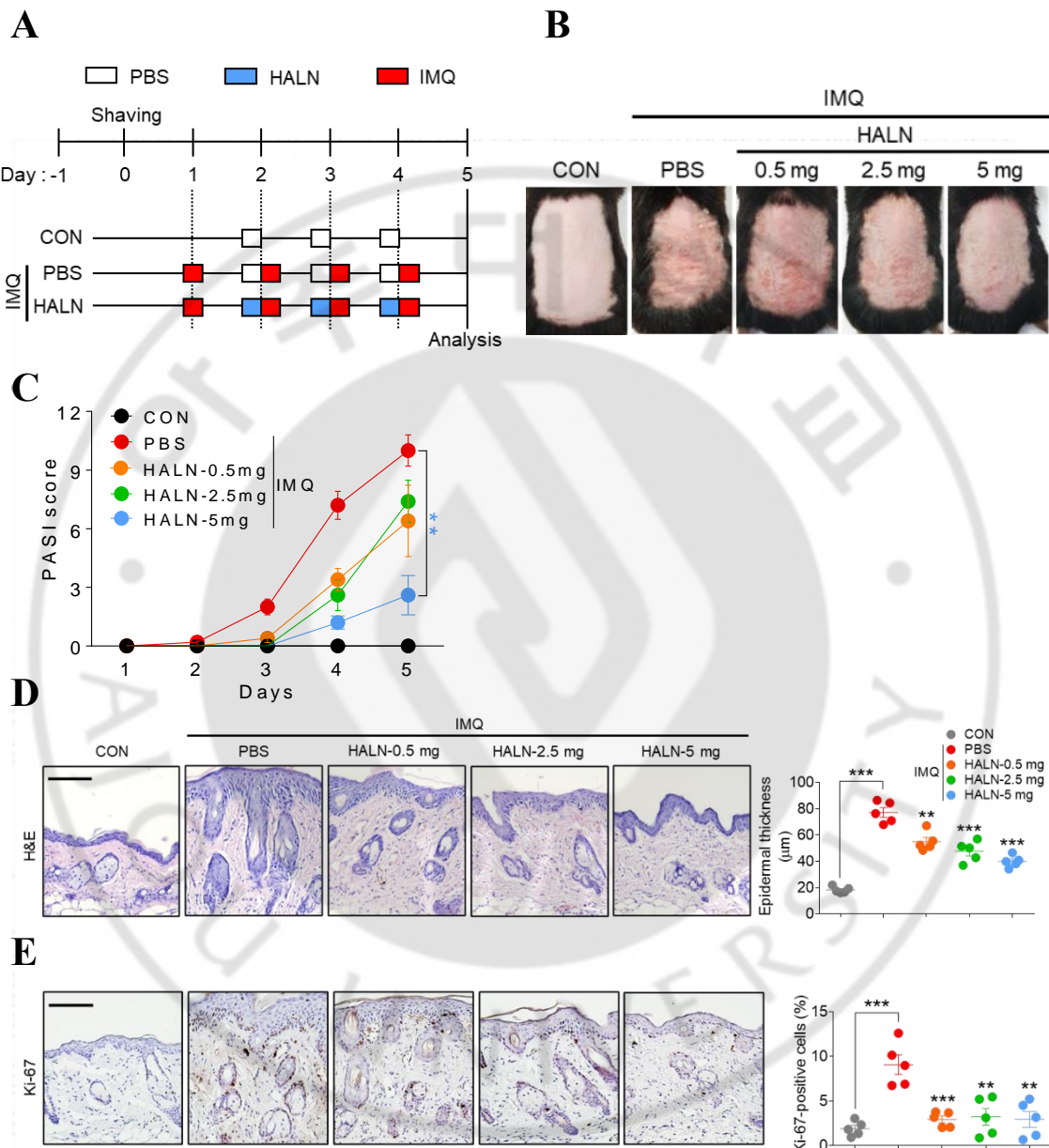
Based on the promising therapeutic outcomes via the subcutaneous route and skin-penetrating ability of HALN, I evaluated the therapeutic efficacy after a transcutaneous administration. C57BL/6 mice were transcutaneously administered with 5% IMQ for four consecutive days from day 1 and HALNs (0.5, 2.5, and 5 mg/cm<sup>2</sup>) for three consecutive days from day 2 on the shaved dorsal skin, and 5% IMQ treatment was applied topically 2 h after HALN treatment to allow its full absorption and minimize their interaction (Figure 16A). Compared with PBS-treated animals, HALN-treated animals were protected against an IMQ-induced increase of the PASI score, epidermal hyperplasia, macrophage infiltration, and expression of pro-inflammatory cytokines (Figure 16B–F). The therapeutic effect of HALN was enhanced as the hydrodynamic size decreased (Figure 17), suggesting size dependent therapeutic efficacy of HANP against psoriasis.

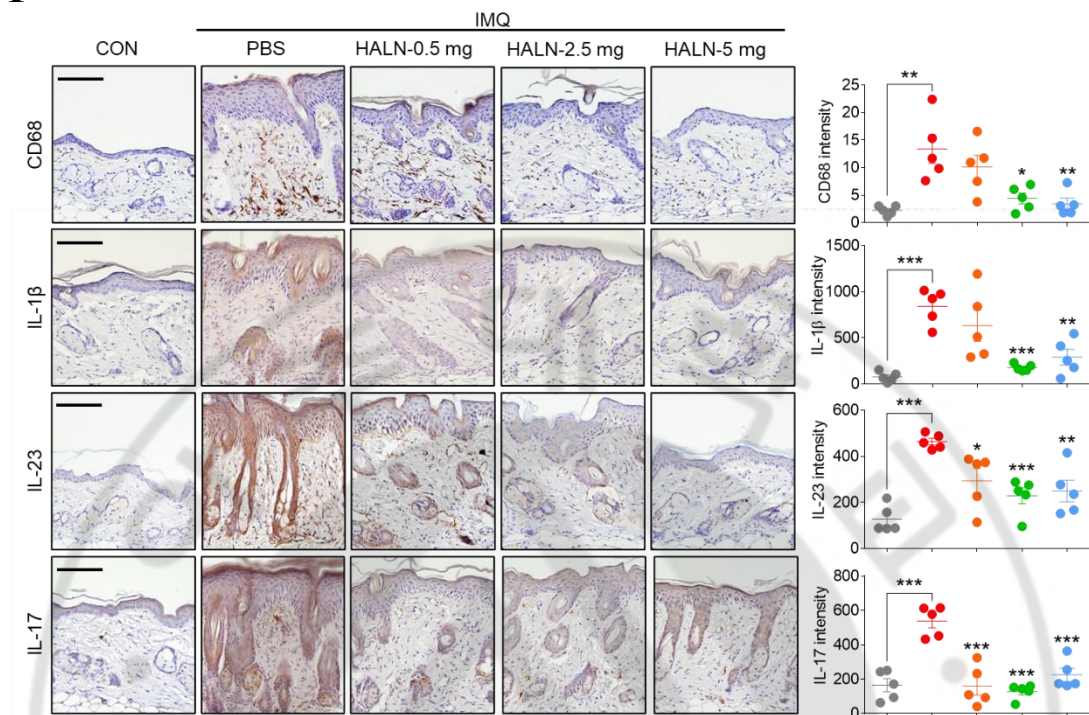
To examine the impact of HA molecular weight (MW) and hydrophobic moiety, I synthesized additional HANPs, consisting of hydrophilic 10 kDa HA and hydrophobic LCA (10k-HALN), as indicated by <sup>1</sup>H NMR and TEM (Figure 18A and Table 2). 10k-HALN had a similar hydrodynamic diameter to HALN and HACN (Table 2). For in vivo experiments using IMQ-inflamed mice, transcutaneously administered 10k-HALN also showed similar therapeutic efficacy to HALN and HACN, as reflected by a significant reduction in the PASI score, epidermal

hyperplasia, and macrophage infiltration (Figure 18B–G), indicating that the therapeutic efficacy of HANPs on psoriasis-like skin dermatitis is due to the outermost hydrophilic HA shell layer, independent of the MW of HA and the hydrophobic moiety.

Furthermore, I compared the efficacy of HALN with other topical psoriasis therapeutics widely used in the clinical settings, including Dermovate (clobetasol propionate) and Daivonex (calcipotriol). Compared with Dermovate and Daivonex, HALN treatment revealed comparable or improved therapeutic efficacy against IMQ-induced psoriasis-like skin dermatitis (Figure 19). Furthermore, the therapeutic efficacy of transcutaneously administered HALN was also similar to that of intraperitoneally injected anti-IL-17A antibody and MTX against IMQ-induced psoriasis-like skin dermatitis (Figure 20), indicating the therapeutic potential of HANP as a topical drug for psoriasis.

**Figure 16**

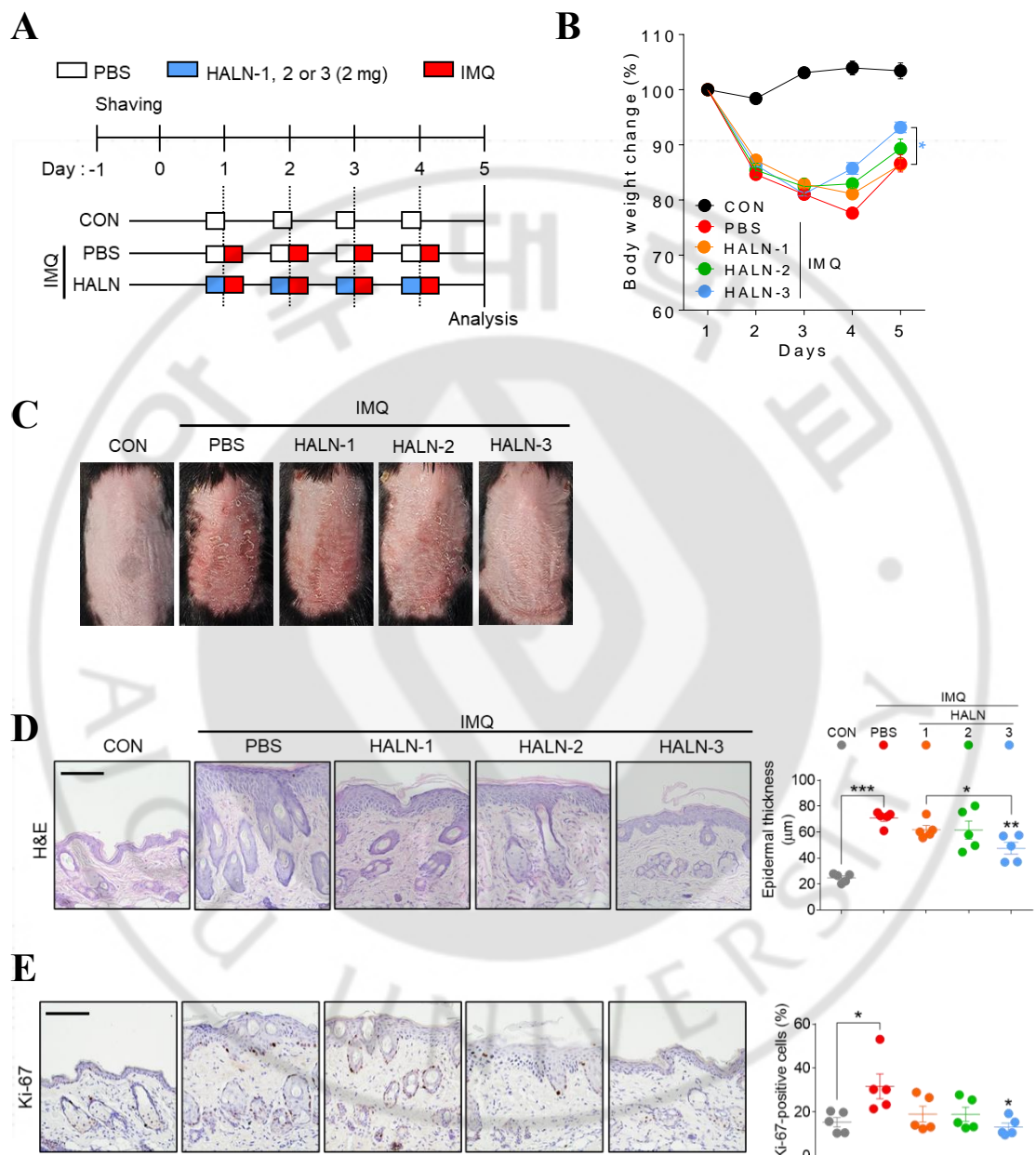


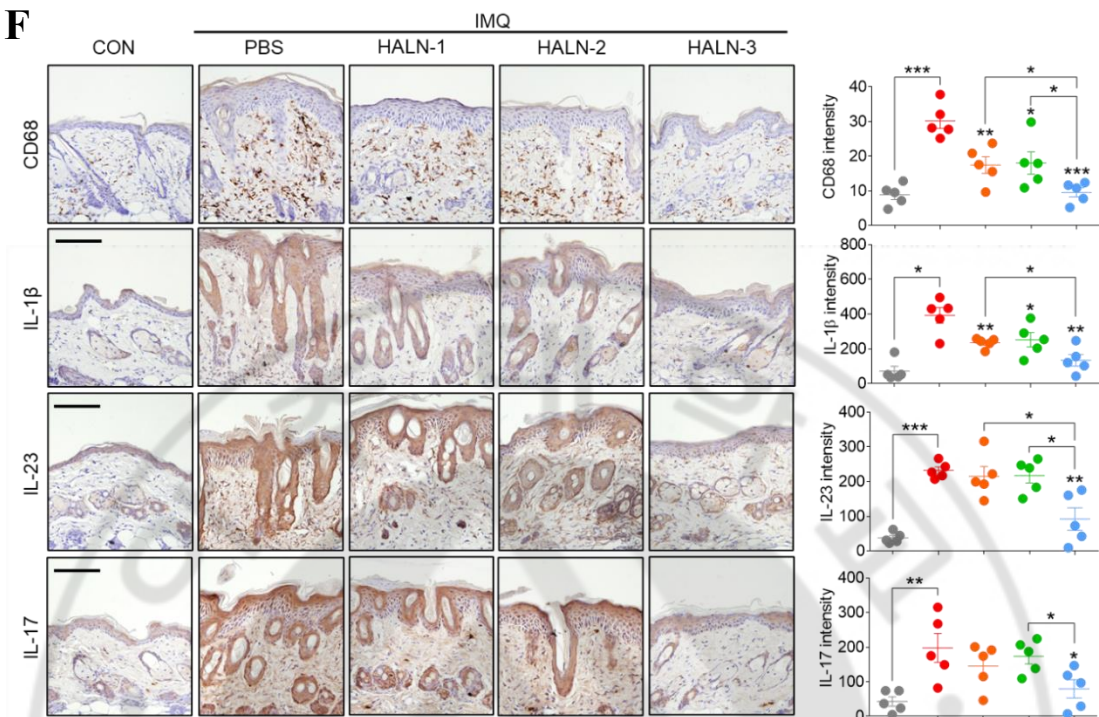
**F**

**Figure 16. Transcutaneous administration of HALN protects animals against IMQ-induced psoriasis-like skin dermatitis.**

**(A)** Experimental timeline. For four consecutive days, PBS or Aldara cream was topically applied on the shaved dorsal skin. On days 2, 3, and 4, PBS or HALN (0.5, 2.5, or 5 mg/cm<sup>2</sup>) was transcutaneously administered to IMQ-inflamed skin. **(B)** Representative gross images of the skin on day 5. **(C)** PASI score reflecting the severity of erythema, scaling, and skin thickening for five days. **(D)** Epidermal thickness assessed on day 5. **(E)** Epidermal percentage of Ki-67-positive cells assessed on day 5. **(F)** Expression patterns of CD68, IL-1 $\beta$ , IL-23, and IL-17 determined by immunohistochemical staining in skin sections of each group. Data are presented as mean  $\pm$  SEM ( $n = 5$  mice). \* $P < 0.05$ , \*\* $P < 0.01$ , \*\*\* $P < 0.001$ , analyzed by two-way ANOVA with Bonferroni's post hoc test (C) or two-tailed Student's t test (D-F).

**Figure 17**

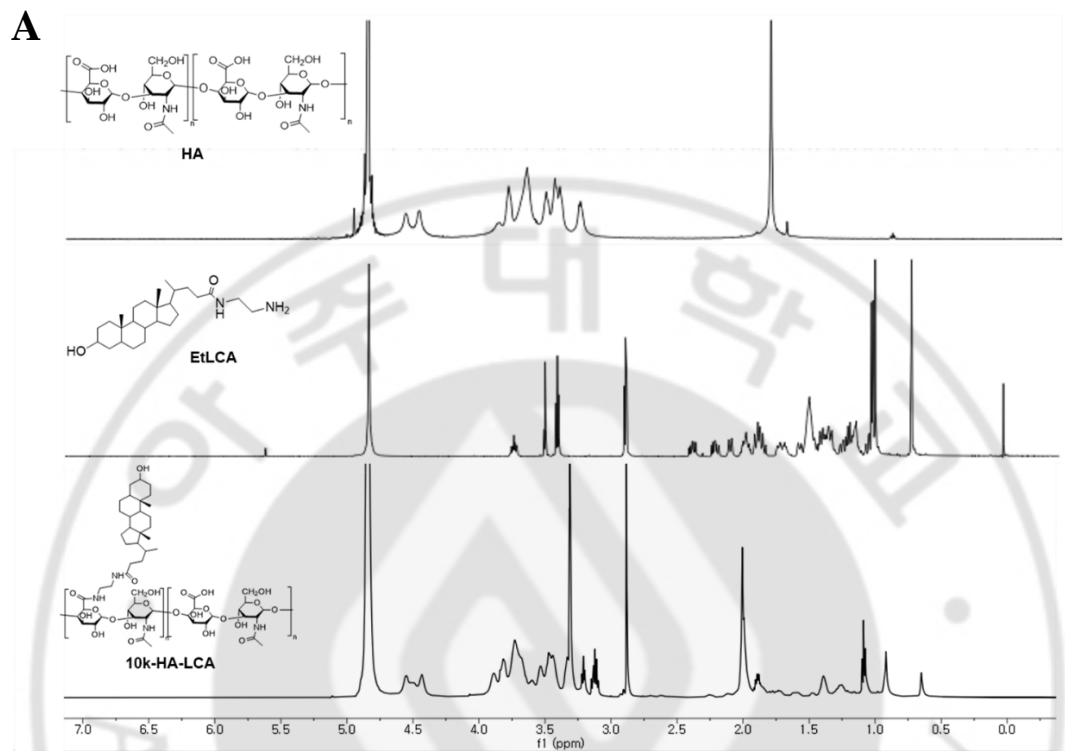


**F**

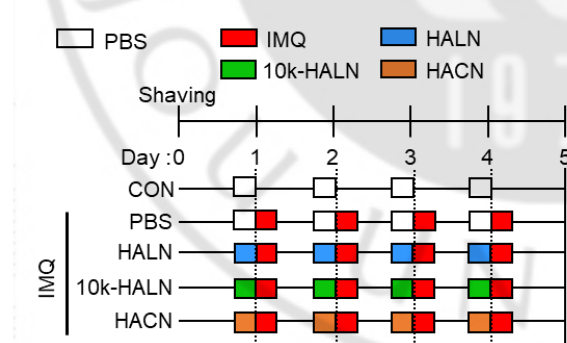
**Figure 17. Effects of HALN size on IMQ-induced psoriasis-like skin dermatitis**

(A) Experimental timeline for IMQ-induced psoriasis-like skin dermatitis and HALN treatment. C57BL/6 mice were transcutaneously administered with PBS or 2 mg/cm<sup>2</sup> of HALN-1, HALN-2, or HALN-3 prior to topical application of Aldara cream (5% IMQ) for 4 consecutive days. (B) Daily bodyweight changes in each group for 5 days. (C) Representative gross images of the skin on day 5. On day 5, animals were euthanized, and epidermal thickness (D) and the percentage of Ki-67-positive cells in epidermis (E) were quantified in skin sections from each group. Scale bars, 100 µm. (F) Expression patterns determined by immunohistochemical staining for CD68, IL-1 $\beta$ , IL-23 and IL-17 in skin sections of each group. Scale bars, 100 µm. Data are presented as mean  $\pm$  SEM (n = 5 mice per group). \*P < 0.05, \*\*P < 0.01, \*\*\*P < 0.001, analyzed by two-tailed Student's t test (D-F) or two-way ANOVA with Bonferroni's post hoc test (B).

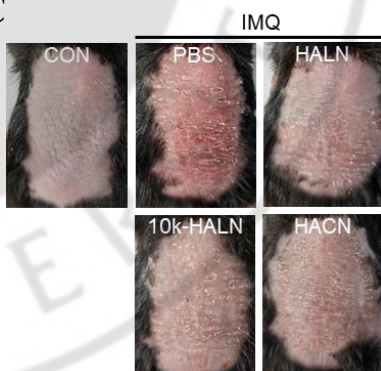
**Figure 18**

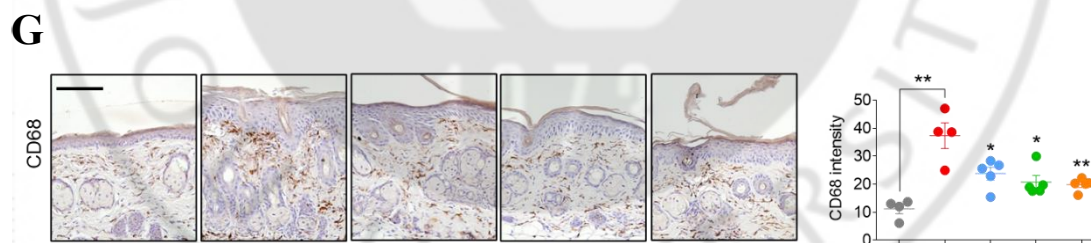
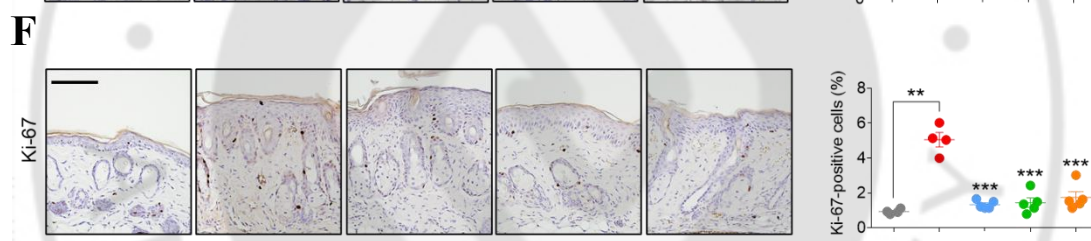
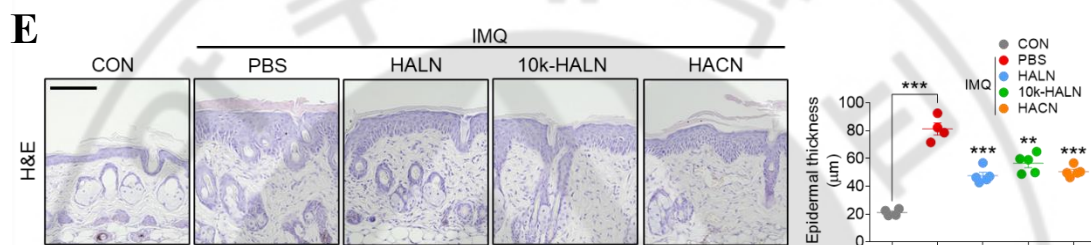
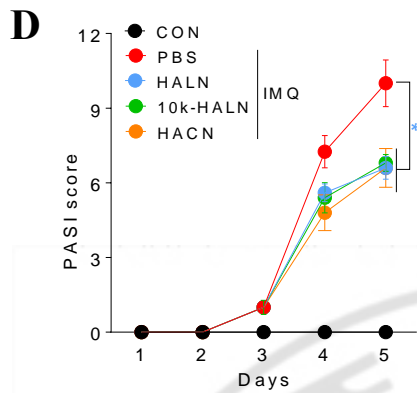


**B**



**C**

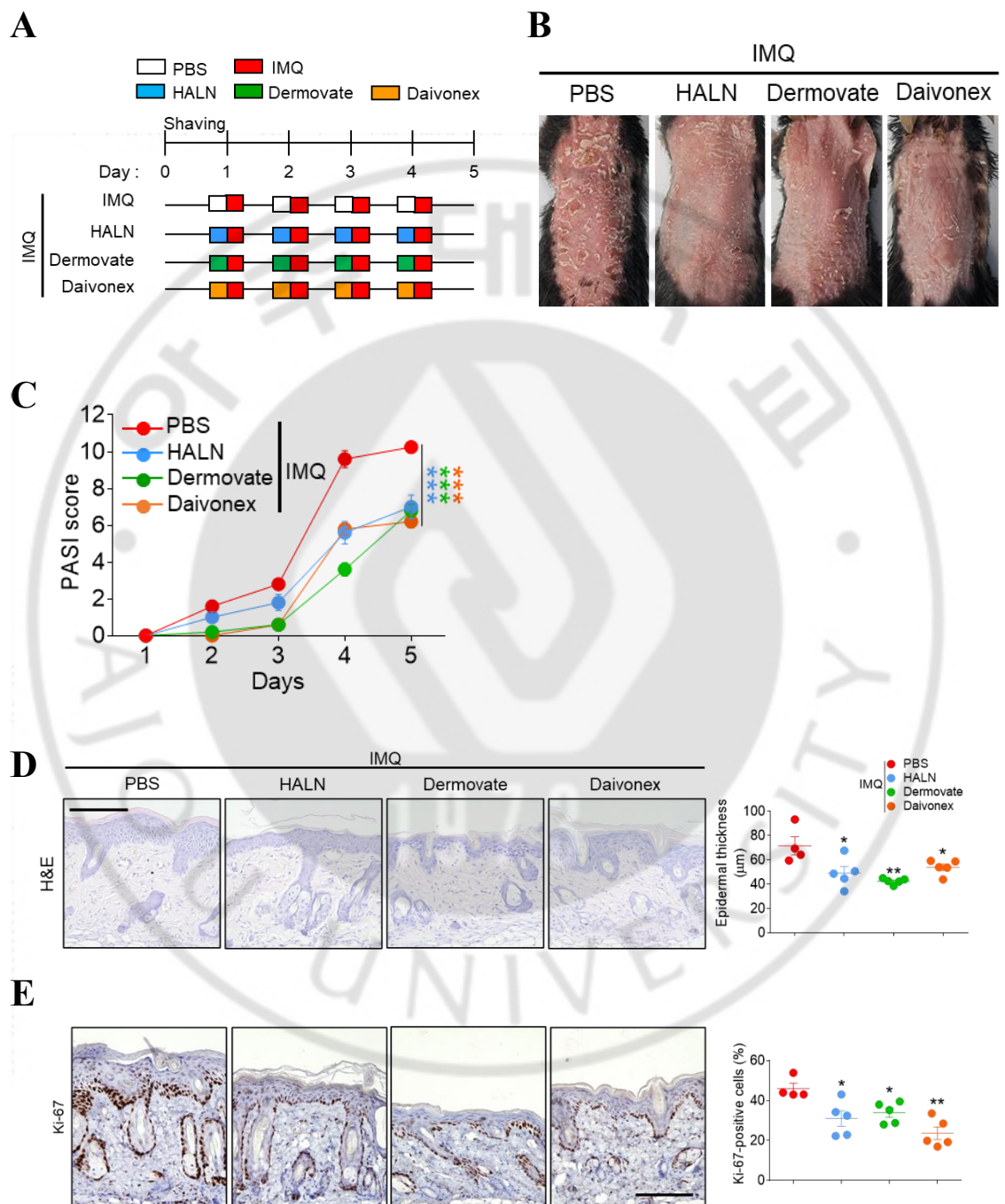


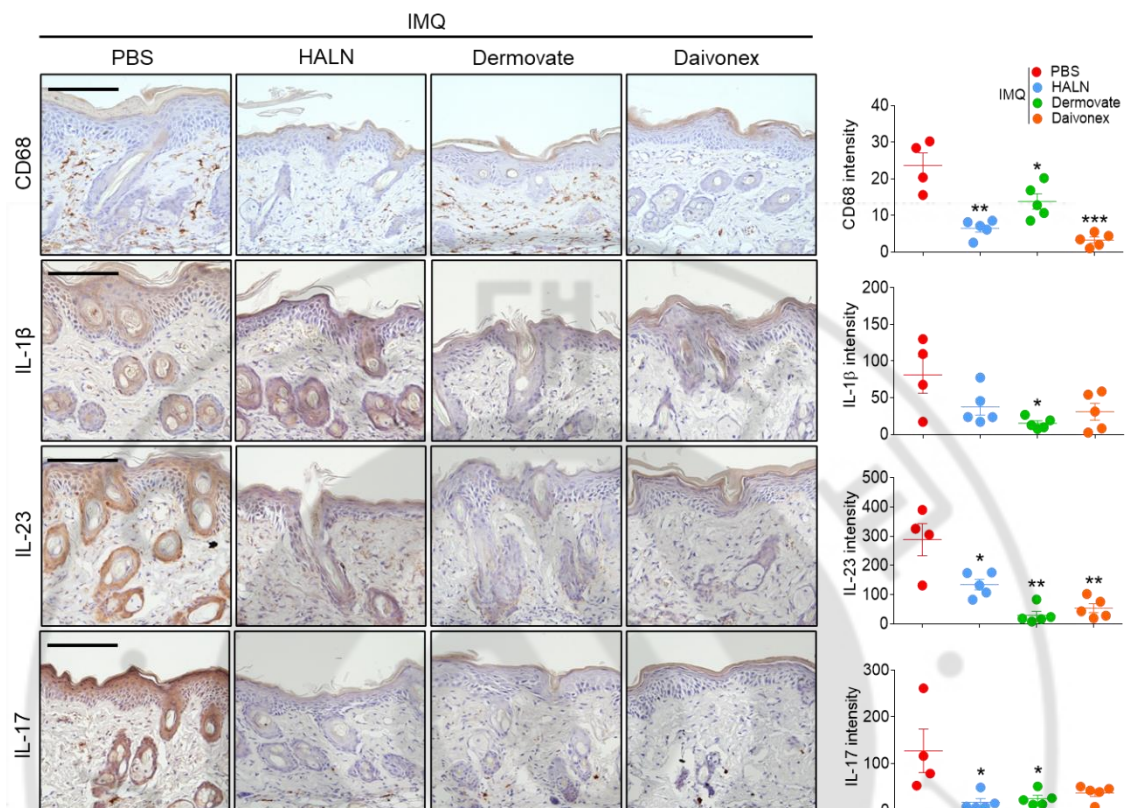


**Figure 18. Effects of 10k-HALN on IMQ-induced psoriasis-like skin dermatitis.**

**(A)**  $^1\text{H}$  NMR spectra of HA, EtLCA, and 10k-HA-LCA. **(B)** Experimental timeline. For 4 consecutive days, PBS or HANPs (2 mg/cm<sup>2</sup>) were transcutaneously administered on the shaved dorsal skin of C57BL/6 mice 6 h prior to topical application of Aldara cream (5% IMQ). **(C)** Representative gross images of the skin on day 5. **(D)** PASI score reflecting the severity of erythema, scaling, and skin thickening for 5 days. **(E and F)** On day 5, animals were euthanized, and epidermal thickness (**E**) and the percentage of Ki-67-positive cells in epidermis (**F**) were quantified in skin sections from each group. **(G)** Expression patterns determined by immunohistochemical staining for CD68 in skin sections of each group. Scale bars, 100  $\mu\text{m}$ . Data are presented as mean  $\pm$  SEM (n = 4–5 mice per group). \*P < 0.05, \*\*P < 0.01, \*\*\*P < 0.001, analyzed by two-tailed Student's t test (**E-G**) or two-way ANOVA with Bonferroni's post hoc test (**D**).

**Figure 19**



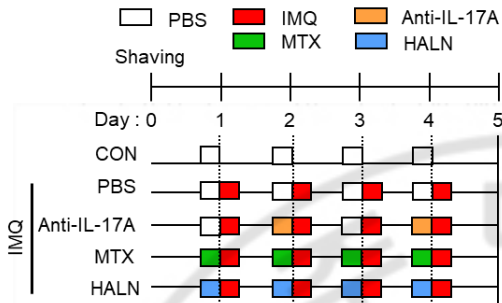
**F**

**Figure 19. Effects of HALN, Dermovate, and Daivonex on IMQ-induced psoriasis-like skin inflammation.**

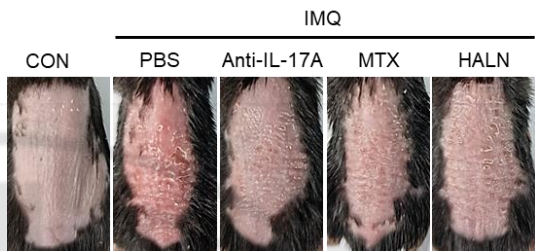
**(A)** Experimental timeline. For four consecutive days, PBS, HALN (2 mg/cm<sup>2</sup>), Dermovate (50 mg/cm<sup>2</sup>), or Daivonex (50 mg/cm<sup>2</sup>) was transcutaneously administered on the shaved dorsal skin, prior to topical application of Aldara cream. **(B)** Representative gross images of the skin on day 5. **(C)** PASI score reflecting the severity of erythema, scaling, and skin thickening for five days. **(D)** Epidermal thickness assessed on day 5. **(E)** Epidermal percentage of Ki-67-positive cells assessed on day 5. **(F)** Expression patterns were determined by immunohistochemical staining for CD68, IL-1 $\beta$ , IL-23 and IL-17 in skin sections of each group. Scale bars, 100  $\mu$ m. Data are presented as mean  $\pm$  SEM ( $n = 5$  mice per group). Data are presented as mean  $\pm$  SEM ( $n = 4\text{--}5$  mice). \* $P < 0.05$ , \*\* $P < 0.01$ , \*\*\* $P < 0.001$ , analyzed by two-way ANOVA with Bonferroni's *post hoc* test (**C**) or two-tailed Student's *t* test (**D-F**).

**Figure 20**

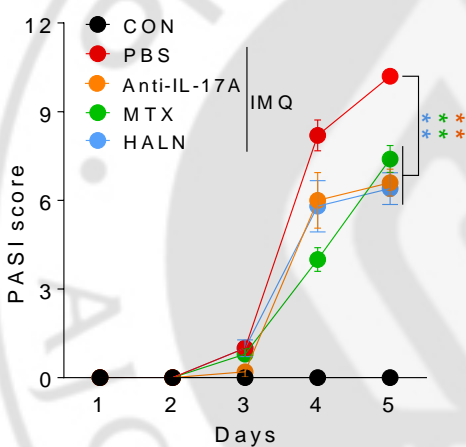
**A**



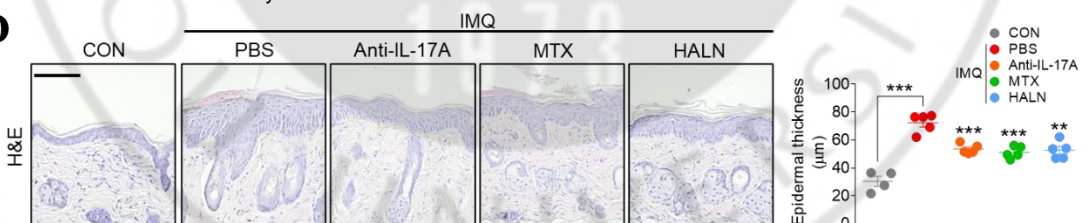
**B**



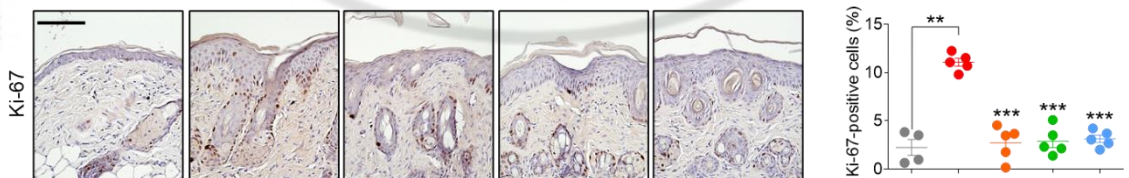
**C**



**D**



**E**



**F**

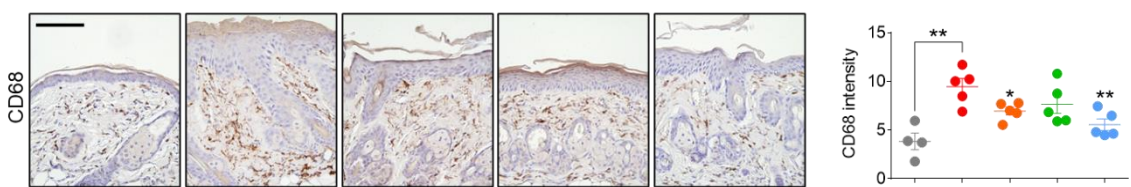


**Figure 20. Effects of HALN, anti-IL-17A antibody, and MTX on IMQ-induced psoriasis-like skin dermatitis**

(A) Experimental timeline. PBS and HALN ( $2\text{ mg/cm}^2$ ) were transcutaneously administered on the shaved dorsal skin of C57BL/6 mice, and MTX (10 mg/kg) and anti-IL-17A antibody (100  $\mu\text{g}$ ) were intraperitoneally administered into C57BL/6 mice 6 h prior to topical application of Aldara cream (5% IMQ). (B) Representative gross images of the skin on day 5. (C) PASI score reflecting the severity of erythema, scaling, and skin thickening for 5 days. (D and E) On day 5, animals were euthanized, and epidermal thickness (D) and the percentage of Ki-67-positive cells in epidermis (E) were quantified in skin sections from each group. (F) Expression patterns determined by immunohistochemical staining for CD68 in skin sections of each group. Scale bars, 100  $\mu\text{m}$ . Data are presented as mean  $\pm$  SEM ( $n = 4\text{--}5$  mice per group). \* $P < 0.05$ , \*\* $P < 0.01$ , \*\*\* $P < 0.001$ , analyzed by two-tailed Student's t test (D-F) or two-way ANOVA with Bonferroni's post hoc test (C).

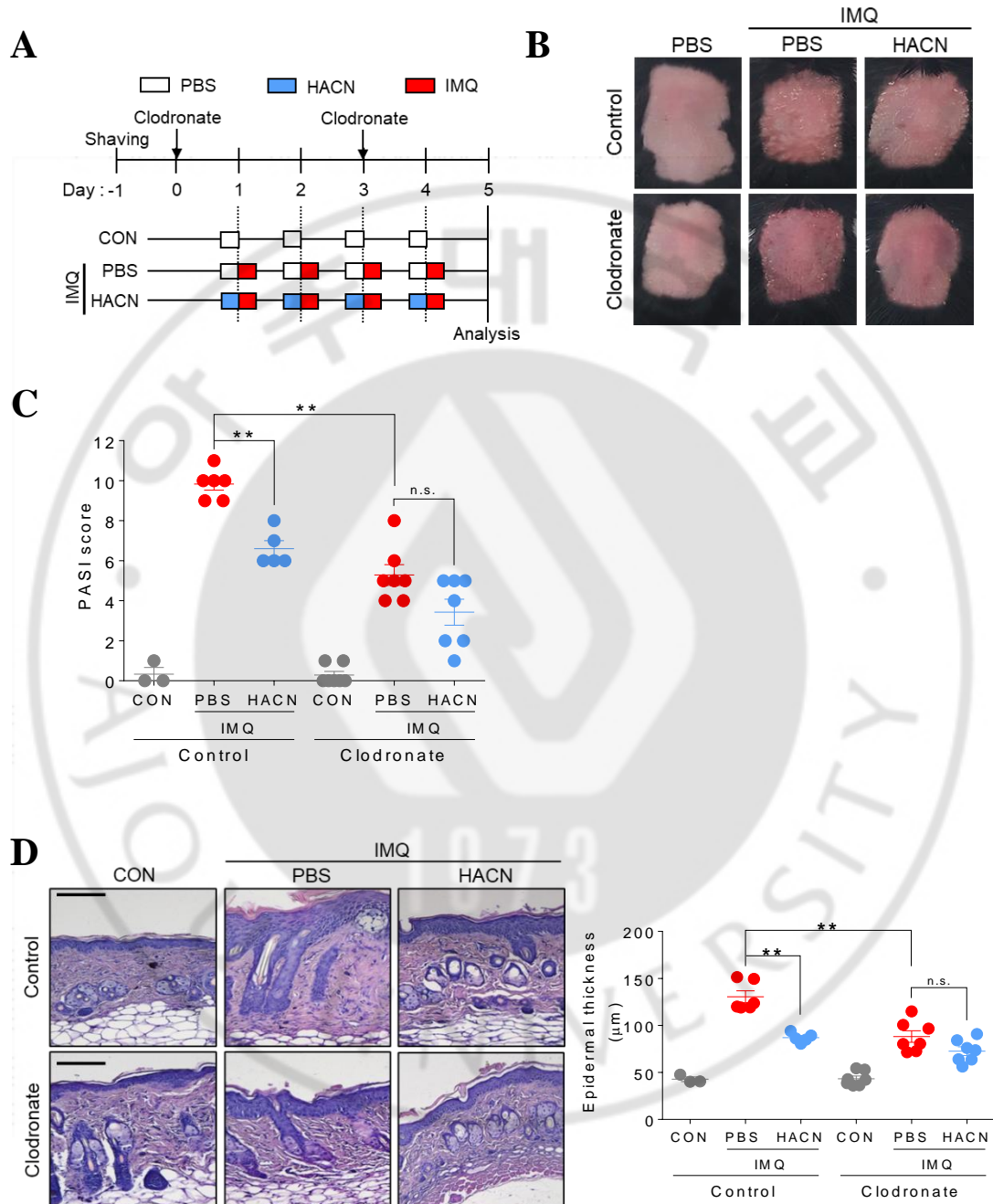
## **II-2.5. Macrophages as a Target in IMQ-Inflamed Skin**

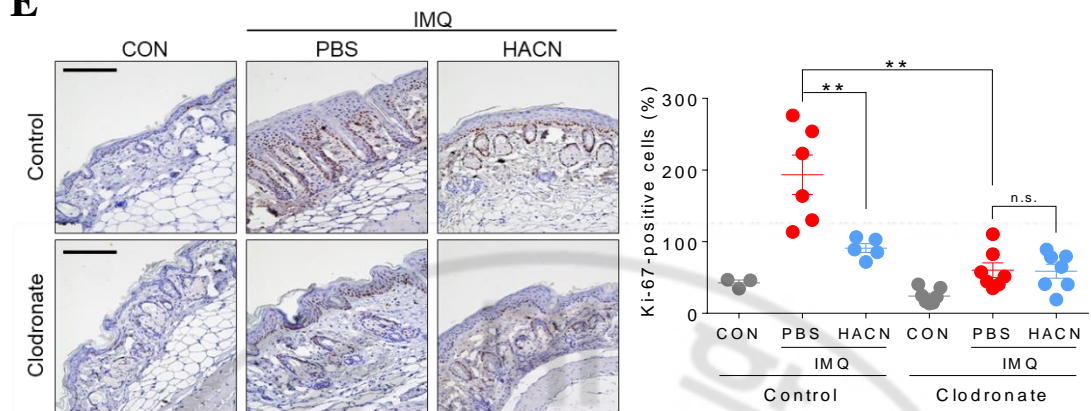
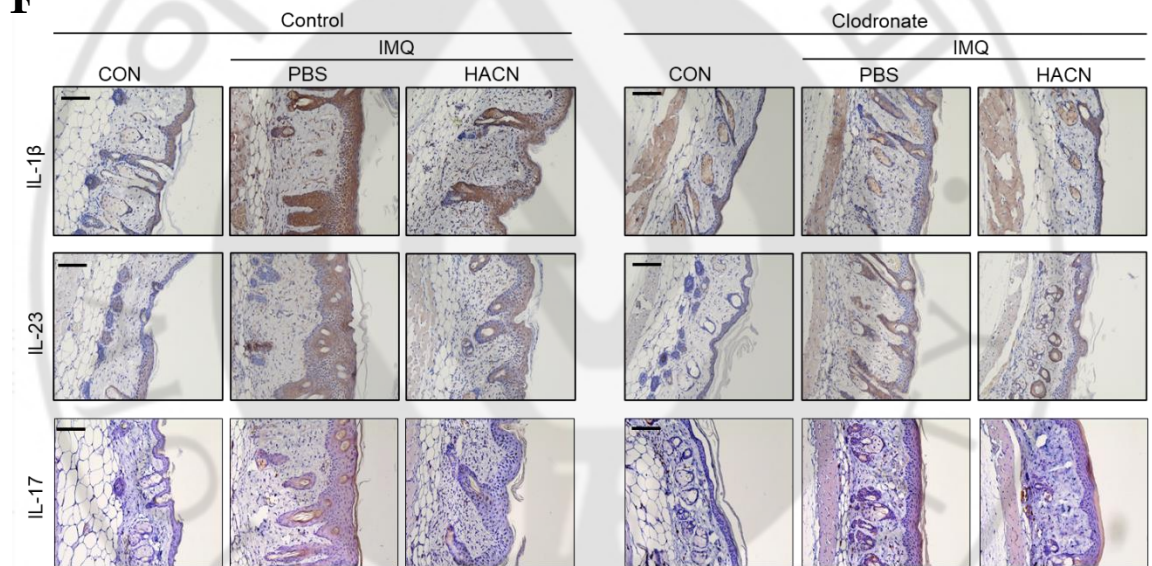
As shown in Figure 10D, I observed the association of HALN with macrophages in the dermis of IMQ-inflamed mice. Growing evidence indicates that the macrophage is a major psoriasis associated immune cell, and their infiltration and activation are a hallmark of psoriasis in mice and humans.<sup>77-80</sup> Thus, I examined the role of macrophages in the therapeutic efficacy of HANP against psoriasis-like skin dermatitis using clodronate liposomes, specifically depleting macrophages *in vivo*.<sup>78, 80, 81</sup> C57BL/6 mice were administered daily HACN via the intravenous route for four consecutive days followed by topical administration of 5% IMQ 1 h after HACN administration. C57BL/6 mice administered daily with HACN via the intravenous route were given 5% IMQ topically for four consecutive days on the shaved dorsal skin 1 h after HACN administration; clodronate and control liposomes were injected via an intraperitoneal route on days 0 and 3 (Figure 21A). The macrophage depletion by clodronate was evaluated by flow cytometry with peritoneal macrophages (PMs) isolated from control or clodronate liposome-treated mice and immunofluorescent staining with anti-CD68 antibody in the skin tissues (Figure 22A). Consistent with the previous reports<sup>77-80</sup>, clodronate liposome-treated mice were protected against IMQ-induced increase in the PASI score, epidermal hyperplasia, expression of psoriasis-associated cytokines, and macrophage infiltration, compared with control liposome-treated mice (Figure 21B-F and Figure 22B). In contrast to control

liposome-treated mice, the protective effect of HACNs against IMQ-induced clinical signs and skin inflammation was markedly lost in clodronate liposome-treated mice (Figure 21B-F and Figure 22B), suggesting that the therapeutic efficacy of HANPs is, at least in part, macrophage-dependent



**Figure 21**



**E****F**

**Figure 21. Effects of HACN on IMQ-inflamed mice after macrophage depletion.**

**(A)** Experimental timeline. For four consecutive days, PBS or HACN (20 mg/kg) was administered to C57BL/6 mice *via* the intravenous route 2 h prior to topical administration of Aldara cream on the shaved dorsal skins. Control and clodronate liposomes (50 mg) were intraperitoneally administrated on days 0 and 3. **(B)** Representative gross images of the skin on day 5. **(C)** PASI score reflecting the severity of erythema, scaling, and thickening on day 5. **(D)** Epidermal thickness assessed on day 5. **(E)** Epidermal percentage of Ki-67-positive cells assessed on day 5. **(F)** Expression patterns determined by immunohistochemical staining for IL-1 $\beta$ , IL-23 and IL-17 in skin sections. Data are presented as mean  $\pm$  SEM ( $n = 3\text{--}7$  mice).

$^{**}P < 0.01$ ,  $^{***}P < 0.001$ , analyzed by Mann-Whitney test. n.s., not significant.

**Figure 22**

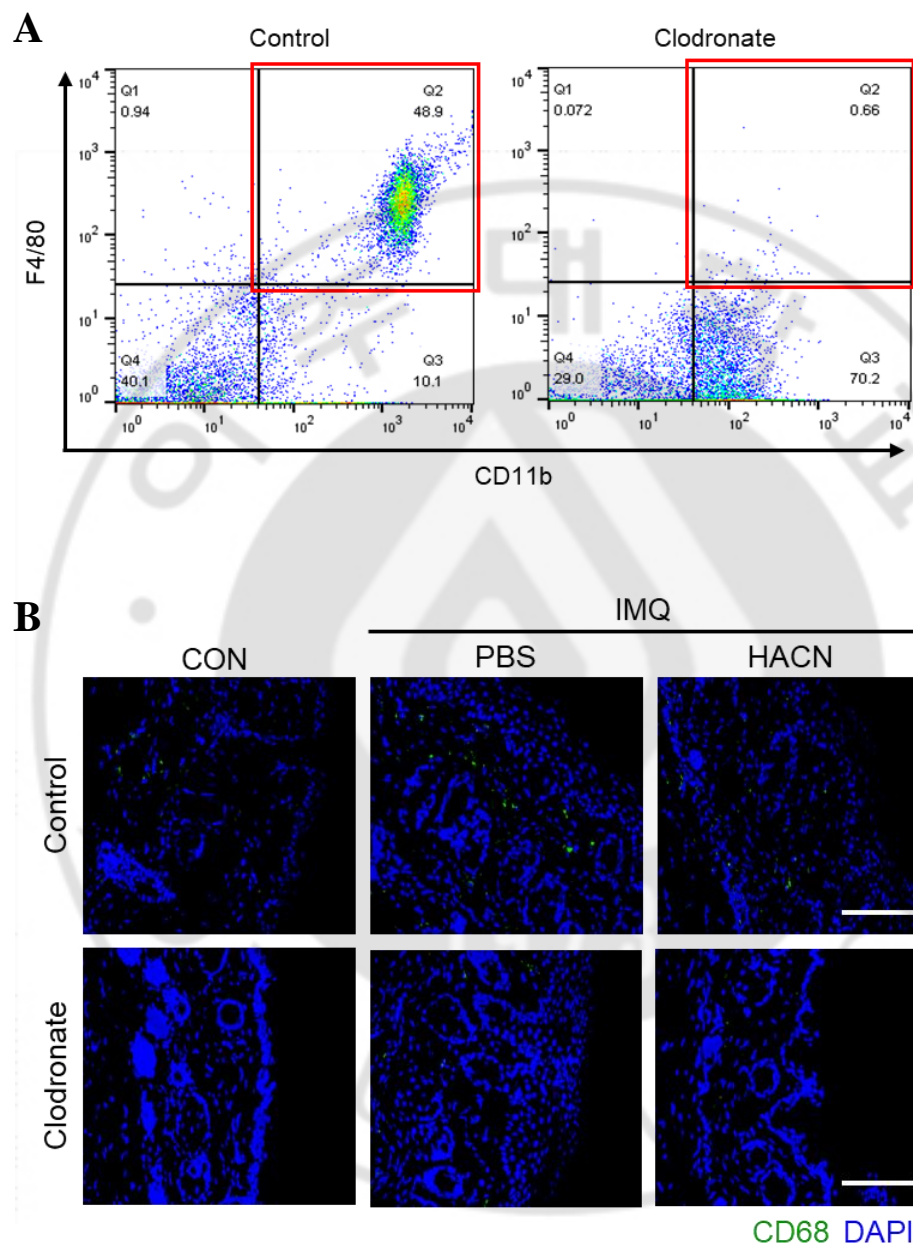


**Figure 22. Clodronate-mediated depletion of macrophages in normal and IMQ-inflamed mice**

(A) Frequencies of F4/80+CD11b+ macrophages isolated from peritoneal cavity of normal mice treated with control or clodronate liposomes (50 mg). (B) Macrophage content determined by immunohistochemical staining for CD68 in the skin sections of IMQ-inflamed mice intravenously administered with PBS or HACN (20 mg/kg) for 4 consecutive days. Control and clodronate liposomes (50 mg) were intraperitoneally administrated on day 0 and 3. DAPI was used for nuclei counter staining. Scale bars, 100  $\mu$ m.

## **II-2.6. Modulation of Macrophage Polarization.**

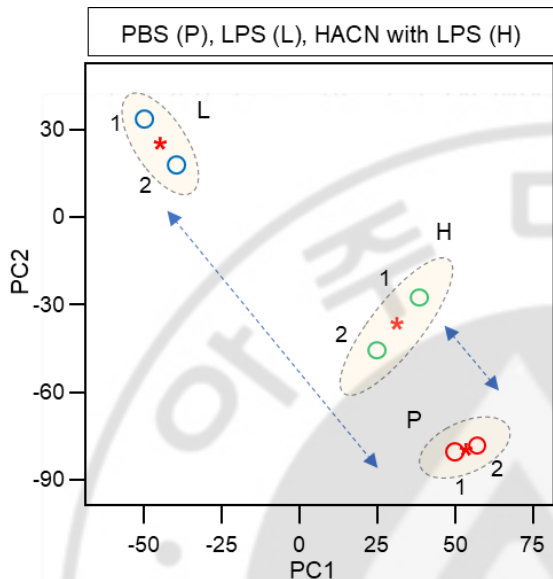
I also investigated whether HANP treatment modulates macrophage polarization toward the pro-inflammatory M1 phenotype (M1 polarization) required in the pathogenesis of psoriasis.<sup>78-80</sup> For this, I used lipopolysaccharide (LPS), an agonist of TLR4, as a major inducer of M1 polarization and performed RNA sequencing in mouse primary bone marrow-derived macrophages (BMDMs) after treating with LPS. The mRNA profiles by RNA sequencing in BMDMs showed that the whole gene expression patterns altered by LPS were restored by HACN treatment, and most of those genes were related to the inflammatory response, including M1 polarization (Figure 23A–D). Notably, transcripts associated with M1 polarization were among those whose expression was most affected by HACN (Figure 23E,F). Thus, I next validated in vitro competitive inhibition assay in THP-1 cells. It showed that the association of Cy5.5-LPS with THP-1 cells was dose-dependently decreased by HACN pretreatment (Figure 24). These findings reveal that HACN can competitively inhibit the LPS-binding capacity of TLR4 (Figure 24). As the downstream signaling of TLR4 occurs through the TLR adaptor protein MyD88 via NF-κB and/or MAP kinases, and this pathway is also critical for the M1 polarization, I verified whether HACN halts the MyD88-dependent TLR4 signals in macrophages. I revealed that LPS-stimulated activation of MAP kinases and NF-κB was significantly inhibited by HACN treatment (Figure 25). Similarly, the effect of HALN to inhibit the LPS-induced M1 polarization in mouse primary bone marrow-

derived macrophages (BMDMs) after treating with LPS. HALN treatment in LPS-stimulated macrophages reduced M1 marker gene expression without affecting cell viability (Figure 26). The inhibitory effect of HALN was enhanced as its hydrodynamic size decreased (Figure 27). In conclusion, these findings reveal that HACN suppresses M1 polarization of macrophages through TLR4 signaling pathway.

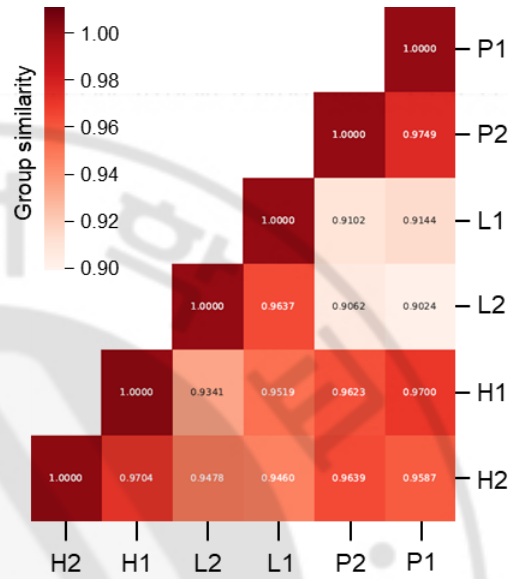


**Figure 23**

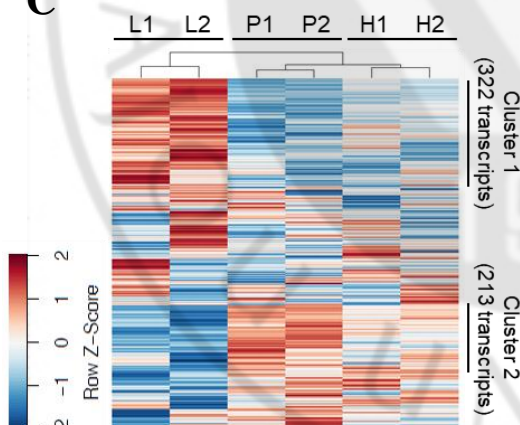
**A**



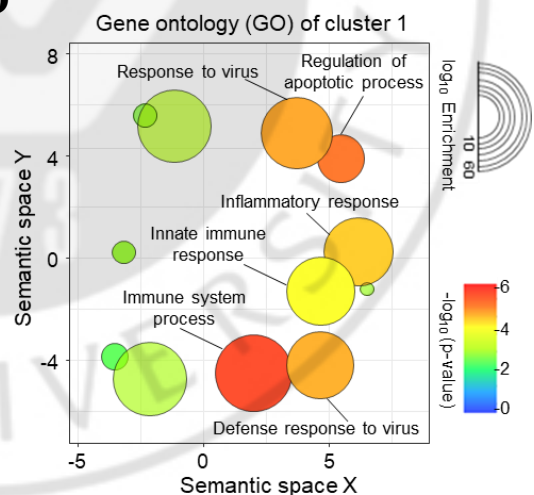
**B**

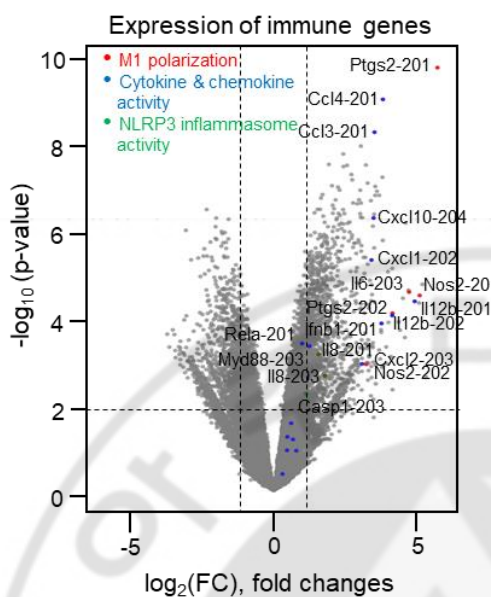
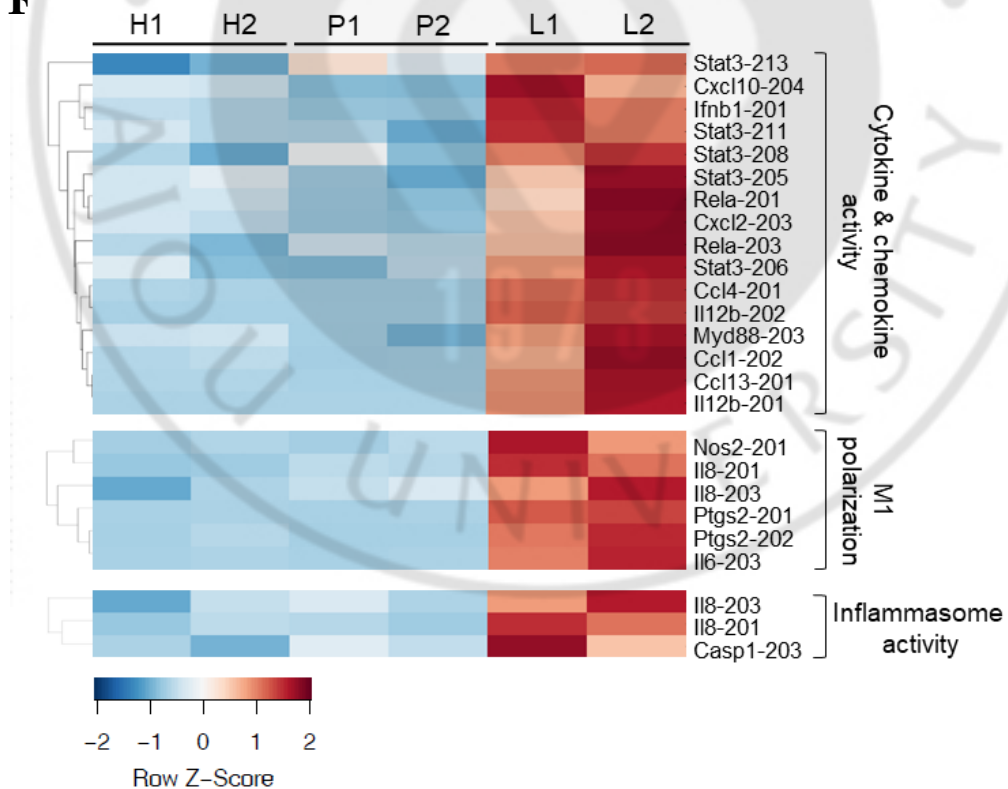


**C**



**D**



**E****F**

**Figure 23. HACN alters LPS-induced gene expression patterns in BMDMs.**

Bone marrow-derived macrophages (BMDMs) from C57BL/6 mice were stimulated with LPS (10 ng/ml) in the presence or absence of HACN (10 µg/ml) for 4 h. Common gene expression patterns through two independent experiments were identified by RNA-Seq platform. **(A)** Principal component analysis (PCA) of RNA-Seq. The values indicate the amount of variation attributed to each principal component. Small circles indicate individual samples, red asterisks indicate the average between experimental replicates, and larger yellow ovals represent each experimental group. **(B)** Cosine similarity represents the similarity between the indicated samples. **(C)** Differential gene expression patterns in the RNA-Seq. Hierarchically clustered genes (rows) and experimental samples (columns) with dendrograms and clusters from RNA-Seq data. Red in the heatmap indicates upregulation, and blue denotes downregulation of gene expressions based on z-score. **(D)** Top enriched GO biological processes and cellular components of LPS-treated cells were visualized from significant DEGs of RNA-Seq platforms. The size of the circle represents enriched genes, and the color represents  $-\log_{10}$  of the P-value. **(E)** Volcano plot from the filtered data set that are significant DEGs between untreated- and LPS-treated cells. **(F)** Hierarchically clustered inflammatory response genes (rows) and experimental samples (columns) with dendrograms and clusters from RNA-Seq data.

**Figure 24**

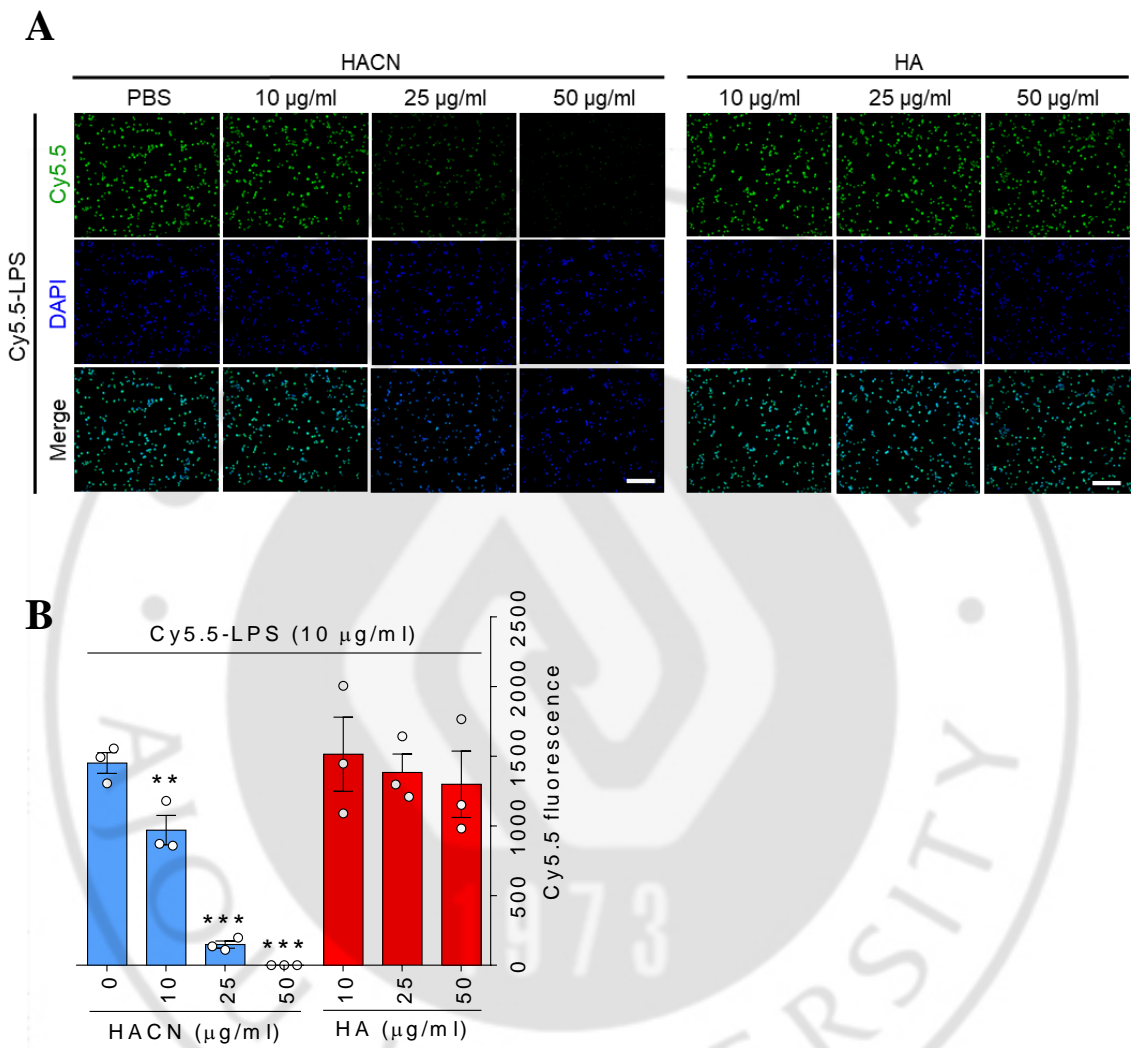


**Figure 24. HACN can competitively inhibit the LPS-binding capacity of TLR4.**

(A) Confocal images of THP-1 cells incubated with Cy5.5-labeled LPS (Cy5.5-LPS) and HACN or 10-kDa free HA (HA). Cells were incubated with HACN or HA (10, 25, or 50  $\mu$ g/ml) for 60 min, followed by stimulation with 10  $\mu$ g/ml Cy5.5-LPS for 30 min. DAPI was used for nuclei counter staining ( $n = 3$  independent samples). (B) The cy5.5 fluorescence intensity of the images was quantified. Data are presented as mean  $\pm$  SEM. \*\* $P < 0.01$ , \*\*\* $P < 0.001$ , analyzed by two-tailed Student's  $t$  test.

**Figure 25**

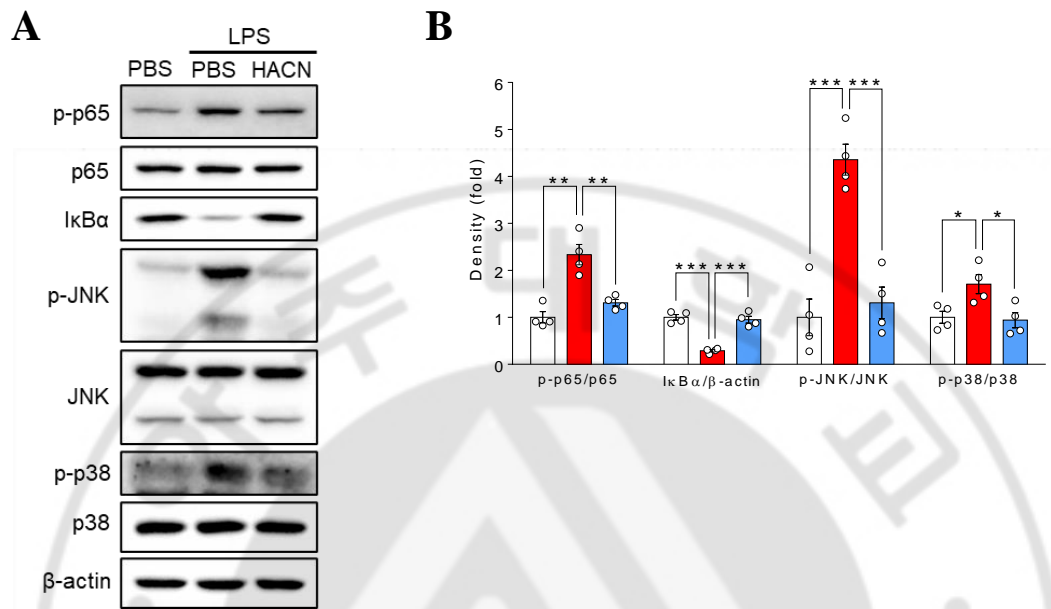
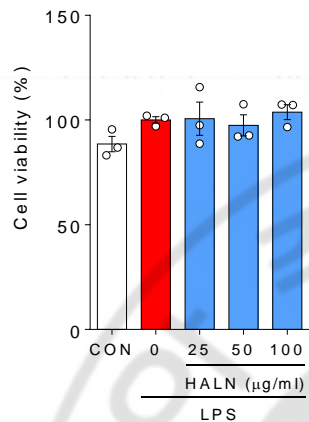


**Figure 25. Relative densities for TLR4 downstream signaling proteins determined by western blot analysis in THP-1**

(A) Abundance of TLR4 downstream signaling molecules determined by immunoblot analysis in THP-1 cells 30 min after stimulation with LPS (1 µg/ml) and PBS or HACN (100 µg/ml). p, phosphorylated. (B) Relative densities for TLR4 downstream signaling proteins determined by western blot analysis in A (n = 4). Data are presented as mean ± SEM. \*P < 0.05, \*\*P < 0.01, \*\*\*P < 0.001, analyzed by two-tailed Student's *t* test.

**Figure 26**

**A**



**B**

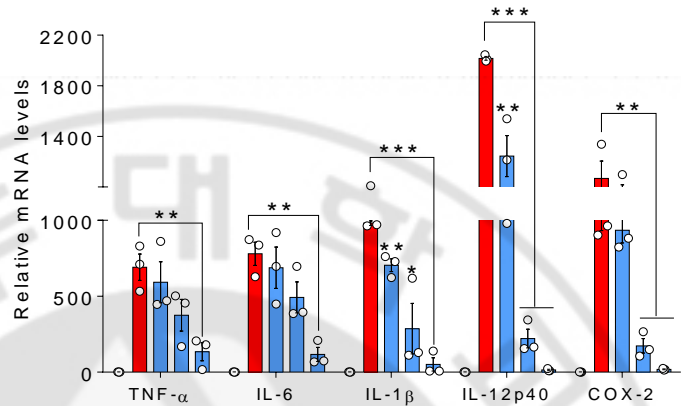
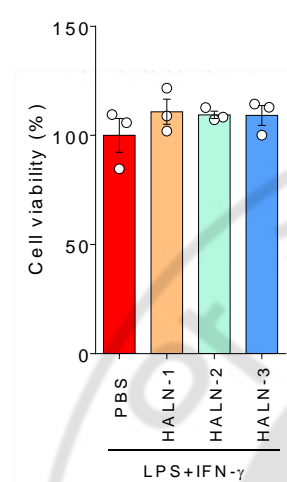


**Figure 26. HALN inhibits LPS-induced M1 polarization of macrophages**

(A) Cell viability of BMDMs stimulated with LPS (100 ng/ml) in the presence or absence of HALN (25, 50, or 100 µg/ml) for 4, 24, or 48 h. (B) mRNA levels of TNF- $\alpha$ , IL-6, IL-1 $\beta$ , IL-12p40, and COX-2 in BMDMs stimulated with LPS (100 ng/ml) in the presence or absence of HALN (25, 50, or 100 µg/ml) for 4 h. Data are presented as mean  $\pm$  SEM ( $n = 3$  independent samples). \*P < 0.05, \*\*P < 0.01, \*\*\*P < 0.001, analyzed by two-tailed Student's t test.

**Figure 27**

**A**



**B**

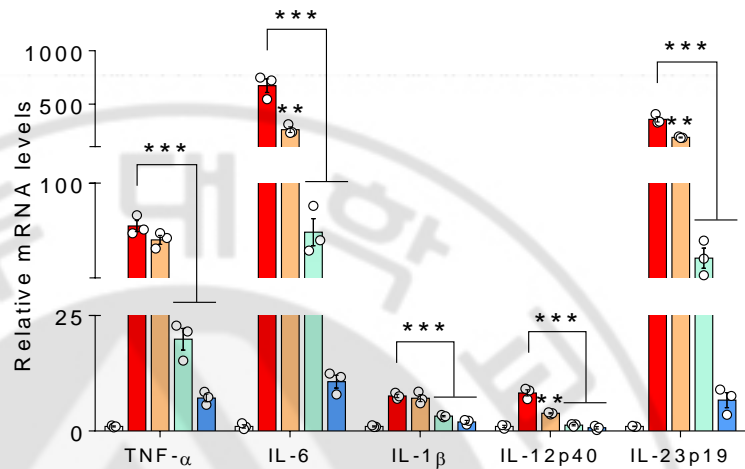


**Figure 27. HALN inhibits LPS-induced M1 polarization of macrophages**

(A) Cell viability of THP-1 cells stimulated with LPS (100 ng/ml) and IFN $\gamma$  (20 ng/ml) in the presence or absence of HALN-1, HALN-2, or HALN-3 (50  $\mu$ g/ml) for 4 h. (B) mRNA levels of TNF- $\alpha$ , IL-6, IL-1 $\beta$ , IL-12p40, and IL-23p19 in THP-1 cells stimulated with LPS (100 ng/ml) and IFN $\gamma$  (20 ng/ml) in the presence or absence of HALN-1, HALN-2, or HALN-3 (50  $\mu$ g/ml) for 4 h. Data are presented as mean  $\pm$  SEM ( $n = 3$  independent samples). \*\*P < 0.01, \*\*\*P < 0.001, analyzed by two-tailed Student's t test.

## II-3 DISCUSSION

I detected a self-assembled HANP with skin-penetrating and anti-inflammatory properties and demonstrated its therapeutic efficacy by transcutaneous administration in a mouse model of IMQ- and IL-23-induced psoriasis-like skin dermatitis (Figure 1A). Though recent reports have explored systemic administration of HANPs to treat several inflammatory diseases, including T2D,<sup>17, 72</sup> osteoarthritis,<sup>73</sup> and atherosclerosis,<sup>16</sup> this study demonstrates the promising potential of transcutaneously administered HANPs in their ability to penetrate the skin and modulate skin thickness and inflammatory responses. I showed that transcutaneous administration of HANP normalized the IMQ-induced clinical signs and skin inflammation. Additionally, HANP was associated with pro-inflammatory macrophages via TLR4. Moreover, compared with other conventional therapeutic agents for topical and systemic treatment of psoriasis, such as Dermovate, Daivonex, MTX and anti-IL-17A antibody, HALN revealed compatible or enhanced therapeutic efficacy against the IMQ- and IL-23-induced clinical signs and skin inflammation. While conventional immunosuppressive agents are associated with numerous off-target adverse effects to varying degrees,<sup>53, 54</sup> repeated HALN treatments did not trigger any local and systemic adverse effects. Taken together, these results indicate the multi-faceted benefits of a self-assembled HALN against psoriasis-like skin dermatitis safely and effectively.

Additionally, I showed the size-dependent therapeutic efficacy of HANPs against psoriasis-like skin dermatitis, likely due to their different stability and skin penetrating ability. Compared with the larger HANPs and free HA, the smallest HALN had the highest resistance to HYAL-mediated degradation and skin-penetrating ability. Moreover, the inhibitory effect of HANPs on pro-inflammatory response and IMQ-induced clinical signs was enhanced as their hydrodynamic size decreased, suggesting the importance of a more compact self-assembled nanostructure in improving therapeutic efficacy. Furthermore, the hydrophobic constituent LCA had no protective effect against IMQ- and IL-23-induced psoriasis models, and the MW of free HA did not affect the therapeutic efficacy of HANP. Thus, these results suggest that the therapeutic effects of HANPs on psoriasis-like skin dermatitis are due to the presence of self-assembled hydrophilic HA shell, regardless of hydrophobic moiety and MW of HA.

I also demonstrated the potential of HANP to suppress the polarization of macrophages toward the pro-inflammatory M1 phenotype, required in the pathogenesis of psoriasis, as reflected by the normalization of LPS-induced expression of M1 marker genes and the frequencies of pro-inflammatory F4/80<sup>+</sup>CD11b<sup>+</sup>CD86<sup>+</sup> populations. In contrast, the hydrophobic constituents (LCA and CA) and free HAs (10 and 60 kDa) failed to normalize the LPS-induced expression of M1 marker genes in BMDMs, indicating that the efficacy of HANPs was derived from the presence of self-assembled HA shell, independent of the

hydrophobic constituents and free HAs. This inhibitory effect of HANPs on M1 polarization is likely due to their ability to interact with TLR4 as a competitive inhibitor, as characterized by *in vitro* competitive inhibition assay. Consistently, transcutaneously administered HANP were found to be associated with CD68+ macrophages in IMQ-inflamed dermis, which was mediated by TLR4 on pro-inflammatory M1 macrophages. Notably, when macrophages were depleted by intraperitoneal injection with clodronate liposome *in vivo*, HANP therapy markedly lost its efficacy against IMQ-induced psoriasis-like skin dermatitis. While macrophages play an essential role in the pathogenesis of rodent and human psoriasis,<sup>82-85</sup> I demonstrate that the therapeutic efficacy of HANP was mediated, in part, by changes in the macrophages; whether HANP modulates the activity of other immune cells such as dendritic cells and T cells in psoriasis also deserves future investigation.

### **III. MATERIALS AND METHODS**

#### **2.1. Materials**

The chemicals were obtained from commercial vendors and used without further purification. Biomedical grade sodium hyaluronates were obtained from Lifecore Biomedical, Inc. Thin layer chromatography (TLC) was used to monitor the reaction progress, and components were observed under UV light or by staining TLC plates

#### **2.2. Characterization of Compounds**

$^1\text{H}$  and  $^{13}\text{C}$  NMR spectra were analyzed using JNM-ECZ 600R (JEOL) with chemical shifts reported as ppm (TMS as internal standard). Chemical shifts were reported in parts per million ( $\delta$ ) and calibrated using internal tetramethylsilane (TMS) standard or residual undeuterated solvent for  $^1\text{H}$  NMR spectra (CHLOROFORM-D 7.26 ppm; METHANOL-D<sub>6</sub> 3.31 ppm) and for  $^{13}\text{C}$  NMR spectra (CHLOROFORM-D 77.16 ppm; METHANOL-D<sub>6</sub> 49.00 ppm). Multiplicity was indicated as follows: s (singlet); d (doublet); t (triplet); q (quartet); quin (quintet); m (multiplet); dd (doublet of doublet); dt (doublet of triplet); br s (broad singlet), br d (broad doublet) etc. Coupling constants were reported in Hz. A compact mass spectrometer (Advion) was used as low-resolution mass spectrometry (LRMS).

### **2.3. CA Ester**

A methanol solution (20 mL) with 5 $\beta$ -cholanic acid (1 g, 2.77 mmol) and 12 N HCl (180  $\mu$ L) was refluxed at 70 °C for 6 h. After removal of methanol by evaporation, the reaction mixture was washed with double-distilled water and dried in vacuo for 1 day to obtain CA ester (926 mg, 91% yield) in a pure powder form.  $^1\text{H}$  NMR (600 MHz,  $\text{CDCl}_3$ )  $\delta$  3.65 (s, 3H), 2.34 (ddd,  $J$  = 15.4, 10.3, 5.2 Hz, 1H), 2.20 (ddd,  $J$  = 15.4, 9.9, 6.5 Hz, 1H), 1.93 (dt,  $J$  = 12.3, 3.0 Hz, 1H), 1.87–1.67 (m, 6H), 1.59–1.50 (m, 2H), 1.44–0.97 (m, 22H), 0.94–0.82 (m, 7H), 0.63 (s, 3H); LRMS (ESI) m/z calcd for  $\text{C}_{25}\text{H}_{42}\text{O}_3$  [M + H]<sup>+</sup> 375.62, found 375.51

### **2.4. EtCA**

An ethylenediamine solution (20 mL) with CA ester (926 mg, 2.47 mmol) was refluxed at 130 °C for 12 h. After removal of ethylenediamine by evaporation, the reaction mixture was resuspended with the ACN and double-distilled water (v:v = 1:4) mixture, the resulting precipitate was washed with double-distilled water, and the product was dried in vacuo to obtain EtCA (821 mg, 84% yield) in a pure powder form.  $^1\text{H}$  NMR (600 MHz,  $\text{CDCl}_3$ )  $\delta$  3.29–3.21 (m, 3H), 2.76 (dd,  $J$  = 7.8, 4.1 Hz, 2H), 2.30–2.23 (m, 1H), 2.13–2.06 (m, 1H), 1.98 (dd,  $J$  = 12.0, 2.5 Hz, 1H), 1.92–1.84 (m, 2H), 1.75 (dd,  $J$  = 20.7, 11.4 Hz, 4H), 1.59 (d,  $J$  = 3.3 Hz, 1H), 1.48–1.01 (m, 20H), 0.99–0.81 (m, 7H), 0.70–0.63 (s, 3H);  $^{13}\text{C}$  NMR (151 MHz,  $\text{CDCl}_3$ )  $\delta$  174.22, 56.83, 56.28, 43.94, 42.98, 42.11, 41.62, 40.72, 40.51, 37.80, 36.10,

35.77, 35.57, 33.90, 32.09, 28.49, 27.72, 27.46, 27.24, 26.77, 24.48, 24.45, 21.55, 21.04, 18.61, 12.28; LRMS (ESI) m/z calced for C<sub>26</sub>H<sub>47</sub>N<sub>2</sub>O [M + H]<sup>+</sup> 403.67, found 403.47.

## 2.5. HA-CA

A 5 mL DMF solution with EtCA (0.24 equiv to the hyaluronic acid, 29.7 mg, 0.073 mmol) was slowly added to a 24 mL formamide solution of EDC (28 mg, 0.14 mmol) and 10-kDa free HA (120 mg, 0.305 mmol). After 1 day, the reaction mixture was dialyzed using a 3.5K MWCO dialysis membrane in the mixture of double distilled water and methanol (v:v was changed from 1:3 to 1:1) for 24 h and in double-distilled water for 2 days. Lyophilization of the resulting product for 3 days gave HA-CA conjugates in a white fluffy powder form (76 mg, 63% yield). The DS value was determined with <sup>1</sup>H NMR. HA-CA. A 5 mL DMF solution with EtCA (0.24 equiv to the hyaluronic acid, 29.7 mg, 0.073 mmol) was slowly added to a 24 mL formamide solution of EDC (28 mg, 0.14 mmol) and 10-kDa free HA (120 mg, 0.305 mmol). After 1 day, the reaction mixture was dialyzed using a 3.5K MWCO dialysis membrane in the mixture of doubledistilled water and methanol (v:v was changed from 1:3 to 1:1) for 24 h and in double-distilled water for 2 days. Lyophilization of the resulting product for 3 days gave HA-CA conjugates in a white fluffy powder form (76 mg, 63% yield). The DS value was determined with <sup>1</sup>H NMR.

## 2.6. LCA Ester

A methanol solution (20 mL) with lithocholic acid (1 g, 2.65 mmol) and 12NHC<sub>l</sub> (180 μL) was refluxed at 70 °C for 6 h. Then, the crude product was obtained by concentration in vacuo. The resulting solid was washed with double-distilled water and dried in vacuo for 1 day to afford LCA ester (921 mg, 88% yield) as a white powder. <sup>1</sup>H NMR (600 MHz, CDCl<sub>3</sub>) δ 3.64 (s, 3H), 3.60 (td, J = 6.2, 3.1 Hz, 1H), 2.33 (ddd, J = 15.4, 10.3, 5.2 Hz, 1H), 2.23–2.17 (m, 1H), 1.93 (dt, J = 12.3, 3.1 Hz, 1H), 1.87–1.72 (m, 6H), 1.68–1.62 (m, 1H), 1.59–1.46 (m, 2H), 1.43–1.16 (m, 11H), 1.16–0.87 (m, 12H), 0.62 (s, 3H); <sup>13</sup>C NMR (151 MHz, CDCl<sub>3</sub>) δ 175.02, 71.99, 56.68, 56.13, 51.69, 42.91, 42.28, 40.61, 40.35, 36.61, 36.02, 35.55, 34.75, 31.24, 31.18, 30.70, 28.38, 27.39, 26.61, 24.39, 23.57, 21.01, 18.45, 12.22; LRMS (ESI) m/z calcd for C<sub>25</sub>H<sub>43</sub>O<sub>3</sub> [M + H]<sup>+</sup> 391.61, found 391.21.

## 2.7. EtLCA

An ethylenediamine solution (20 mL) with LCA ester (921 mg, 2.65 mmol) was refluxed for 12 h at 130 °C. After removal of ethylenediamine by evaporation, the reaction mixture was resuspended with the acetonitrile (ACN) and double-distilled water (v:v = 1:4) mixture, the resulting precipitate was washed with double-distilled water, and the product was dried in vacuo to obtain EtLCA (800 mg, 72% yield) in a pure powder form. <sup>1</sup>H NMR (600 MHz, CDCl<sub>3</sub>) δ 3.57 (tt, J = 11.1, 4.6 Hz, 1H), 3.25 (t, J = 6.2 Hz, 2H), 2.76 (t, J = 6.2 Hz, 2H), 2.35–2.21 (m, 1H), 2.10 (ddd, J =

13.9, 10.3, 6.2 Hz, 1H), 1.99 (dt,  $J$  = 12.6, 3.3 Hz, 1H), 1.89 (dddt,  $J$  = 18.2, 13.6, 9.0, 5.0 Hz, 2H), 1.8–1.71 (m, 3H), 1.69–1.56 (m, 2H), 1.53–1.37 (m, 8H), 1.35–1.22 (m, 6H), 1.19–1.05 (m, 6H), 1.02–0.91 (m, 8H), 0.67 (s, 3H);  $^{13}\text{C}$  NMR (151 MHz,  $\text{CDCl}_3$ )  $\delta$  174.14, 72.11, 56.76, 56.27, 43.00, 42.35, 42.13, 41.66, 40.69, 40.44, 36.73, 36.10, 35.77, 35.60, 34.83, 33.92, 32.08, 30.81, 28.50, 27.44, 26.67, 24.46, 23.62, 21.08, 18.65, 12.30; LRMS (ESI)  $m/z$  calcd for  $\text{C}_{26}\text{H}_{47}\text{N}_2\text{O}_2$  [ $\text{M} + \text{H}]^+$  419.67, found 419.43.

## 2.8. HA-LCA

EDC·HCl (56.1 mg, 0.293 mmol) and N-hydroxysuccinimide (33.3 mg, 0.293 mmol) were added to a 24 mL formamide solution containing 60 kDa free HA (120 mg, 0.305 mmol). After mixing for 20 min, a 5 mL DMF solution containing EtLCA (0.08, 0.32, or 0.48 equiv to the HA for HALN-1, HALN-2, or HALN-3, respectively) was dropwisely added to the reaction mixture and the reaction proceeded for 24 h. The resulting reaction mixture was dialyzed with a 13K MWCO dialysis membrane in the mixture of double-distilled water and methanol (v:v was changed from 1:3 to 1:1) and in double-distilled water for 1 day and 2 days, respectively. The resulting product solution was lyophilized for 3 days to obtain dried HA-LCA conjugates in a fluffy pure white solid form (80 mg, 66% yield). The DS value was determined with  $^1\text{H}$  NMR.

## **2.9. 10k-HA-LCA**

A 1 mL formamide solution with N-hydroxysuccinimide (33 mg, 0.287 mmol) was added to a 19 mL formamide solution with EDC (55 mg, 0.287 mmol) and 10 kDa free HA (120 mg, 0.305 mmol), followed by the dropwise addition of a 5 mL DMF solution containing EtLCA (0.48 equiv to the hyaluronic acid, 61.2 mg, 0.146 mmol). After mixing for 24 h, the reaction mixture was dialyzed using a 13K MWCO dialysis membrane in a mixture of double-distilled water and methanol (v:v was changed from 1:3 to 1:1) and in double-distilled water for 1 day and 2 days, respectively. The resulting product solution was lyophilized for 3 days to obtain dried 10k-HALN conjugates as a white fluffy powder (95 mg, 79% yield). The DS value was determined with  $^1\text{H}$  NMR.

## **2.10. Cy5.5-HA**

To a 30 mL solution of 10 mM PB with 60 kDa free HA (50 mg, 0.12 mmol), EDC (2 mg, 0.01 mmol), and hydroxybenzotriazole (HOBt, 1.4 mg, 0.01 mmol) was added a methanol solution (1 mL) with Cy 5.5 hydrazide (3 mg, 0.004 mmol). After 1 day of reaction under dark conditions, the reaction mixture was dialyzed using a 13K MWCO dialysis membrane in double-distilled water for 2 days.

## **2.11. Cy5.5-HA-LCA and Cy5.5-HA-CA**

To a 23 mL PB (10 mM) solution with EDC (4.8 mg), HOBr (3.2 mg), and HA-LCA

conjugate, or HA-CA conjugate (100 mg) was added a 5 mL methanol solution of Cy 5.5 hydrazide (6 mg). After 1 day of reaction under dark conditions, the reaction mixture was dialyzed using 13K MWCO dialysis membrane for HA-LCA conjugate and 3.5K MWCO dialysis membrane for the HA-CA conjugate, respectively, in double-distilled water for 2 days. Lyophilization for 3 days gave Cy5.5-HA-LCA conjugates or Cy5.5-HA-CA conjugates (~40 mg) in a fluffy blue powder form.

## **2.12. Characterization of HANPs**

Owing to the amphiphilic nature, the HA conjugates can form nanoparticles by self-assembly in aqueous conditions. For the characterization, a PBS solution of HA-CA, HALCA, Cy5.5-HA-CA, or Cy5.5-HA-LCA (1.5 mg/mL) was sonicated with a probe-type sonicator (266 W, 10 s on and 1 s off of the short interval) for 50 s to induce nanoparticle formation via self-assembly. After the nanoparticle formation, membrane filters (Millipore; 0.45  $\mu\text{m}$  pore size) were used to filter the solution to obtain evenly sized HANPs. An HANP solution (1 mg/mL) in double-distilled water was dropped on copper grid (200-mesh), followed by incubation with 1% uranyl acetate. The HANP morphologies were then analyzed by an HR-TEM (JEOL-2100F). The zeta potential and size of the nanoparticles were determined with a Zetasizer (Nano ZS90, Malvern Instruments).

## **2.13. The 3T3-L1 cell culture and differentiation**

3T3-L1 pre-adipocyte was purchased from American Type Culture Collection (ATCC; Manassas, VA, USA). The 3T3-L1 cells were cultured in high-glucose Dulbecco's Modified Eagle Medium (DMEM, Invitrogen, USA) with 10% (v/v) calf bovine serum (CBS, Gibco, NZ) and 1% (v/v) penicillin-streptomycin in a humidified atmosphere of 5% CO<sub>2</sub> at 37 °C. The pre-adipocytes were seeded at a density of  $2 \times 10^5$  cells per well on six-well plates and cultured until the cells became confluent. Two days later, culture medium was replaced with differentiation medium containing 10% FBS, 1 uM dexamethasone (Sigma-Aldrich, St Louis, MO, USA), 0.5 mM 3-iso-butyl-1-methylxantine (Sigma-Aldrich) and 1 ug/ml<sup>-1</sup> insulin (Roche Diagnostics GmbH, Mannheim, Germany) for 3 days. Then, cells were maintained in DMEM containing 10% FBS and 10 µg/ml insulin for up to 8 days and then the media were replaced with DMEM containing 10% FBS.

## **2.14. The 3T3-L1 cell viability assay**

Cell viability was determined by 3-(4,5-dimethylthiazol-2-y)-5-(3-carboxymethoxyphenyl)-2-(4-sulfophenyl)-2H-tetrazolium (MTS) assay (Promega Corp., USA), according to the manufacturer's instructions. 3T3-L1 cells ( $1.0 \times 10^4$  cells/well) were seeded in 96-well plate and differentiated as described above with various concentrations of HANP (50,100,200 µg/ml) for 10 day. Then, cells were washed with PBS and 200 µl volume of MTS solution was added to each well and

incubated at 37°C for 1 h. The formazan product was dissolved in dimethyl sulfoxide, and its optical density was measured by multi-well spectrophotometer (Cytation 3, BioTek Instruments Inc., USA) at 490 nm wavelength.

### **2.15. Transfection of small interfering RNA**

Transfection of small interfering RNAs (siRNAs) was carried out using Lipofectamine 2000 (Invitrogen), according to the manufacturer's instructions. Scrambled siRNA (Silencer Negative Control #1; Ambion, USA) were transfected as negative controls. The sense sequences of scrambled and CD44 siRNAs were 5' UGUGUCAUACUGGGAGGUUU 3' and 5' CACCUCCCAGUAUGACACAU U 3', respectively.

### **2.16. Mice**

Under the approval of the Institutional Animal Care and Use Committee (IACUC) at Ajou University (2019-0043), animal experiments were carried out in accordance with the guidelines established by the IACUC. C57BL/6 mice were bred and maintained under pathogen-free conditions at the Ajou University Animal Facility. Mice were randomly assigned to experimental groups after co-housing for 1 week.

### **2.17. Histology and Immunofluorescence**

Epididymal white adipose tissue (eWAT) and skin samples were first fixed by incubation with 4% paraformaldehyde (PFA), embedded in paraffin, and sectioned at 4- $\mu$ m thickness. Tissue sections were stained with hematoxylin and eosin (H&E) using a standard protocol and analyzed using Leica DMi8 microscopy (Leica). Epidermal thickness was measured by randomly drawing at least 30 random line segments from the SC to the epidermal-dermal junction for each section using an MRI skin tool of ImageJ software (National Institute of Health). For immunohistochemistry, skin sections were deparaffinized in xylene, rehydrated in distilled water (DW), heat retrieved (incubated for 30 min in boiling 10 mM sodium citrate buffer, pH 6.0, and then allowed to cool naturally), permeabilized (0.25% Triton X-100, 10 min), blocked in normal goat serum blocking solution (Vector Laboratories), and then incubated overnight at 4 °C with following primary antibodies: Ki-67 (1:200, Cell Signaling, D3B5), CD68 (1:200, R&D Systems, MAB101141), IL-1 $\beta$  (1:500, Novus biologicas, NB600-633), IL-23 (1:500, Novus biologicas, NBP1-76697), IL-17 (1:200, Novus biologicas, NBP1-72027). Slides were then washed and incubated with biotinylated secondary antibodies (1:200; Vector Laboratories) for 1 h at room temperature. Immunohistochemical signals were detected using Vectastain Elite ABC kit (Vector Laboratories) and DAB substrate kit for peroxidase (Vector Laboratories), according to standard protocols or the manufacturer's instructions, followed by hematoxylin counterstaining (Vector Laboratories). The slides were analyzed on an inverted microscope (Leica DMi8),

Leica Microsystems), and at least nine random images from at least three sections per mouse were analyzed for signal intensity, and the number of Ki-67-positive cells were analyzed using ImageJ software. The number of Ki-67-positive cells was expressed as a percentage of the total number of cells in the epidermis. For immunofluorescence, after incubation with primary antibodies to CD68 (1:200, Abcam, ab31630), slides were washed and incubated with Alexa Fluor 546 goat anti-rabbit or Alexa Fluor 488 goat anti-mouse secondary antibodies (Life Technologies) at room temperature for 1 h and then washed and sealed with ProLong Gold antifade reagent with DAPI (Life Technologies). The images were collected using LSM 880 NLO (ZEISS), FV3000RS (Olympus), or a Leica DMi8 (Leica Microsystems) microscope.

## **2.18. Quantitative real-time PCR analysis**

Total RNA was isolated using the TRIzol reagent (Thermo Fisher Scientific) according to the manufacturer's instructions. Reverse transcription PCR for cDNA synthesis were performed using the Rever tra qPCR RT Master Mix (TOYOBO, TOFSQ-201, Japan) and then quantitative real-time polymerase chain reaction (qPCR) were performed using a CFX Connect Real-Time PCR Detection System (Bio-Rad) with SYBR Green qPCR Kits (Alkali Scientific). The cycling conditions were as follows: 95 °C for 3 min, 40 cycles of 95 °C for 3 s, and 60 °C for 45 s. The

relative expression of target genes was calculated using GAPDH as a reference gene.

The gene-specific primer sets are listed in Table 3.

**Table 3.** Primer sequences used in this report

Gene	Origin	Strand	Sequence (5'-3')
GAPDH	Mouse	<sup>a</sup> F	CATCACTGCCACCCAGAAGACT
		<sup>b</sup> R	CCAGTGAGCTTCCCCTCA
TNF- $\alpha$	Mouse	F	GTCTCAGCCTCTTCTCATTCTG
		R	TCCTCCACTGGTGGTTGCTAC
IL-6	Mouse	F	TTTCCTCTGGTCTTCTGGAGTAC
		R	CTCTGAAGGACTCTGGCTTGT
COX-2	Mouse	F	TGCACTATGGTTACAAAAGCTGG
		R	TCAGGAAGCTCCTTATTCCCTT
IL-12p40	Mouse	F	GTCCTCAGAACGCTAACCATCTCC
		R	CCAGAGCCTATGACTCCATGTC
IL-23p19	Mouse	F	CAGAACCAAAGGAGGTGGATAG
		R	GGCAACAGCCATAGCATTATTAC
IL-17	Mouse	F	CTCAGACTACCTCAACCGTTCC
		R	ATGTGGTGGTCCAGCTTCC
IL-1 $\beta$	Mouse	F	GAAATGCCACCTTTGACAGTG
		R	TGGATGCTCTCATCAGGACAG
GAPDH	Human	F	TGCACCACCAACTGCTTAGC
		R	GGCATGGACTGTGGTCATGAG
TNF- $\alpha$	Human	F	TGGGATCATTGCCCTGTGAG
		R	CCAGGTTTCGAAGTGGTGGT

<i>IL-6</i>	Human	F	CCACTCACCTCTTCAGAACG
		R	CATCTTGAAAGGTTCAGGTTG
<i>COX-2</i>	Human	F	ATGCTGACTATGGCTACAAAAGC
		R	TCGGGCAATCATCAGGCAC
<i>IL-12p40</i>	Human	F	AACCCTGACCATCCAAGTCAA
		R	CTTGGCCTCGCATCTTAGAAAG
<i>IL-23p19</i>	Human	F	GCTTACAAACTCGGTGAACAACT
		R	GTGGAATCTCTGCCCACTTCC
<i>IL-1β</i>	Human	F	TTCGACACATGGGATAACGAGG
		R	TTTTGCTGTGAGTCCCGGAG

## 2.19. High-fat diet induced obesity mice

CD44 KO mice (C57/BL6J background) were obtained from The Jackson Laboratories (Sacramento, CA, USA). Four-weeks-old mice were fed high-fat diet (HFD; D12492, Research Diets, New Brunswick, NJ, USA) for 20 weeks and were divided into two weight-matched groups (n=8-9 per group). First group were administered a daily intraperitoneally (i.p.) injection with HANP (150 mg/kg) for 4 weeks, and the other group was administered PBS as control. HFD was continued during injection. At the end of the treatment period, mice were sacrificed under respiratory anesthetic and their eWAT were collected for analysis. WT groups were also conducted under the same conditions to compare with CD44 KO groups.

## **2.20. Determination of adipocyte size**

The adipocyte size was measured using a Leica DMRBE microscope with Leica LAS X Hardware Configurator. Measurements were performed on H&E staining images. Leica LAS X Hardware Configurator was used to measure the area of respective cells and classify them into the respective area range. The measured values are expressed as a percentage of cell number corresponding to each range.

## **2.21. Oil-red-O staining**

Lipid accumulation of differentiated 3T3-L1 pre-adipocytes was measured by Oil Red-O staining after adipocyte differentiation. The 3T3-L1 cells were washed twice with PBS and fixed in a 10% formalin in PBS for 2 h. The fixed cells were washed twice with DW and then stained with filtered Oil Red O solution for 10 min. Images were obtained using a Epson GT-1500 scanner (Seiko Epson Corporation, Japan). To quantify lipid accumulaton, stained cells were treated with 100% isopropyl alcohol for 10min, and the absorbance of the extracts was measured at 500nm with a Biotek Cytation 3 plate reader (Winooski, VT, USA).

## **2.22. Colorimetric Assessment of Terminal N-Acetyl-d-Glucosamine (Hyaluronan Breakdown Products)**

N-acetyl-d-glucosamine, a breakdown product of HA after exposure to hyaluronidase (HYAL), was measured using a colorimetric method, as previously

described.<sup>16,26,52</sup> Briefly, 1 mg/ml of free HA (MW = 60 kDa) or HANPs in pH 6.0 PBS buffer was treated with 14.2 IU/ml of HYAL II (Sigma-Aldrich) at 37 °C for 6 h. N-acetyl-D-glucosamine (1 mg/ml) was used for the control group. At determined time points (0 h, 10 min, 0.5 h, 1 h, 2 h, 4 h, and 6 h), 100 µl of the sample was taken, and the mixture comprising 166 µl of PBS was heated for 5 min at 100 °C to stop the enzyme reaction. Further, 33.3 µl of 0.8 M potassium tetraborate (pH 9.0) was added to the mixture, heated for 3 min at 100 °C, and cooled in tap water. Then, 1 ml of p-dimethylaminobenzaldehyde (DMAB) reagent (10 g of DMAB dissolved in 100 ml of glacial acetic acid containing 12.5% (v/v) of 10 M HCl) was added; immediately after mixing, the tubes were incubated in a water bath at 37 °C for 20 min. The solution (200 µl) was measured at a wavelength of 544 nm using a Cytation 3 Cell Imaging Multi-Mode microplate reader (BioTek Instruments Inc.).

## **2.23. Psoriasis-like Mouse Models**

Psoriasis-like mouse models were established after acclimatizing six-week-old female mice for 1 week. For the IMQ-induced psoriasis model, 62.5 mg/cm<sup>2</sup> of Aldara cream (5% IMQ; 3 M Pharmaceuticals) was topically administered for four consecutive days on the back skin treated with depilatory cream and shaved with an electric clipper. Two hours before IMQ application, PBS, HALN (5 or 20 mg/kg), or LCA (2 mg/kg) was administered subcutaneously to mice at the scheduled time points. T6167923 (20 mg/kg, Aobious) was intraperitoneally administered 30 min

prior to the subcutaneous application of HALN (20 mg/kg) for four consecutive days.

For the psoriasis model induced by IL-23 injection, PBS (20  $\mu$ L) containing mouse

recombinant IL-23 (500 ng, BiogLegend) was administered intradermally into the ear skin for eight consecutive days. Two hours after rIL-23 injection, PBS, HALN (20 mg/kg), or LCA (2 mg/kg) was administered via an intravenous route, and MTX (10 mg/kg) was administered via an intraperitoneal route for eight consecutive days.

In experiments evaluating the efficacy of transcutaneously administered HANPs, mice topically received 62.5 mg/cm<sup>2</sup> of Aldara cream (5% IMQ; 3 M Pharmaceuticals) on the shaved dorsal skin for four consecutive days, and HALNs (0.5, 2, 2.5, 5, or 10 mg/cm<sup>2</sup>), Dermovate (50 mg/cm<sup>2</sup>; GSK), Daivonex (50 mg/cm<sup>2</sup>; Leo Pharma), LCA (0.2 mg/cm<sup>2</sup>), 10k-HALN (2 mg/cm<sup>2</sup>), HACN (2 mg/cm<sup>2</sup>), or Six-week-old female C57BL/6 mice were housed in groups of five mice per cage and acclimatized for one week before inclusion in the study. For the IMQ-induced psoriasis model, 62.5 mg/cm<sup>2</sup> of 5% IMQ cream (Aldara; 3 M Pharmaceuticals) was topically applied for four consecutive days on the dorsal skin shaved using an electric clipper and depilatory cream. Two hours before IMQ application HALN (0.5, 2.5 or 5 mg/kg), Dermovate (50 mg/cm<sup>2</sup>; GSK), Daivonex (50 mg/cm<sup>2</sup>; Leo Pharma) or an equal volume of PBS was respectively transcutaneous applied on the shaved dorsal skin 6 h prior to IMQ application to minimize the interactions between the two preparations. HALN was applied on a patch of sterile gauze and then secured to the skin for 6 h using a transparent bio-occlusive dressing (Tegaderm, 3 M Pharmaceuticals). The

percentage changes in body weight were assessed daily for the experimental period. The severity of psoriatic skin lesions was evaluated daily using Area and Severity Index (PASI) scores, which rate erythema, scaling, and thickness on a scale of 0 to 4, as follows: no symptoms, 0; mild, 1; moderate, 2; severe, 3; very severe, 4. PASI scores were summed, resulting in a total scoring range of 0 to 12. On the last day of the experiment, mice were sacrificed, and full-thickness skin samples were excised. Then, the skin tissue samples were used for two-photon microscopy, histological assessment, immunofluorescence staining, flow cytometry analysis, and gene expression analysis.

## **2.24 Cell Isolation from the Shaved Dorsal Skin**

After thoroughly washing the excised skin with cold Hank's balanced salt solution (Gibco) without Ca<sup>2+</sup> and Mg<sup>2+</sup>, the skin was placed in DMEM and cut into small pieces, followed by incubation with DMEM, containing 0.01 mg/mL liberase TL (Roche) and 200 U/mL collagenase D (Merck), at 37 °C for 90 min. The digested tissues were removed by passing through a cell strainer (40 µm pore size, SPL Life Sciences), and the resulting solution was washed and incubated in RBC lysis buffer (Invitrogen) for 1 min. After centrifugation, cells were resuspended in PBS buffer with EDTA (5 mM, Sigma-Aldrich), 2% fetal bovine serum (FBS, Capricorn Scientific), and 2% bovine serum albumin (Bovogen) for flow cytometry.

## **2.25. Hematological Toxicity**

PBS or HALN (20 mg/kg) was subcutaneously administered for five consecutive days, and the percentage changes in body weight were evaluated daily during the duration of the experiment. After euthanizing the mice, their major organs and blood were collected. Blood was immediately sent to T&P Bio Clinical Pathology Core for blood assessment.

## **2.26. In Vivo Toxicity Test**

Six-week-old female C57BL/6 mice were housed in groups of five mice per cage and acclimatized for 1 week before inclusion in the study. Then, 20 mg/kg of HALN or PBS was administered daily via a subcutaneous route for five days, and the percentage changes in body weight were assessed daily for the experimental period. Mice were sacrificed, and their major organs (skin, heart, lung, kidney, liver, and spleen) and blood were collected. Blood was immediately sent to T&P Bio Clinical Pathology Core for blood assessment. Each organ was fixed with 4% (v/v) PFA, embedded in paraffin, and sectioned at 4- $\mu$ m thickness. Tissue sections were stained with H&E and examined by microscopy.

## **2.27. In Vivo Skin Penetration Studies**

Under light anesthesia with isoflurane, 1 mg/cm<sup>2</sup> of Cy5.5-HALNs was applied on a patch of sterile gauze and then secured to the shaved dorsal skins of normal and IMQ-

inflamed mice using a transparent bio-occlusive dressing (Tegaderm, 3 M Pharmaceuticals). Before harvesting the skin tissue for analysis at the scheduled time, the application site was rinsed with PBS to remove residual formulations. The tissue was fixed with 4% PFA, embedded in paraffin, and sectioned for imaging with LSM 880 NLO (ZEISS) or Leica DMi8 (Leica Microsystems) microscopy.

## **2.28. Multi-Photon Microscopy**

Hair was carefully removed from the knee joint of 12-week-old male C57BL/6 mice using a depilatory cream. The shaved dorsal skin from normal and IMQ-inflamed mice was transcutaneous administered with PBS or 2 mg/cm<sup>2</sup> Cy5.5-HALN, Cy5.5 (equivalent dose of Cy5.5 as in Cy5.5-HALN), or Cy5.5-HA (equivalent dose of Cy5.5 as in Cy5.5-HALN) and isolated, fixed in 4% PFA, and examined using LSM 880 NLO microscope (ZEISS), equipped with a BIG2 GaAsP detector at the GIST central research facility (GCRF). Femtosecond titanium: sapphire laser (MaiTai DeepSee, Spectraphysics) at a wavelength of 780 nm was used to detect a Cy5.5 fluorescent signal with a 575–610 nm band-pass filter. To collect three-dimensional images, an objective W-Plan Apochromat (NA 1.0, Zeiss) captured the field of view by 421.1 × 421.1 μm and 1.0 μm optical sectioning capacity and resolution of 1024 × 1024 pixels. Two-dimensional projection and three-dimensional images were processed and analyzed using Zen 2.3 SP1 black or blue edition software (ZEISS).

## **2.29. Ex Vivo Biodistribution**

The ex vivo biodistribution of transcutaneous administered Cy5.5-HALN was analyzed as previously reported (Rho JG et al., J Control Release 2018). Briefly, Cy5.5-HALN (1 mg/cm<sup>2</sup>) was administered transcutaneous on the shaved dorsal skin of 7-week-old female C57BL/6 mice, and the organs and tissues were then dissected from mice at pre-determined time points. Then, the time-dependent biodistribution of Cy5.5-HALN was monitored using the eXplore Optix system (ART Advanced Research Technologies Inc.). All data were calculated using the region of interest function of the Analysis Workstation software (ART Advanced Research Technologies, Inc.).

## **2.30 Cell Culture**

THP-1 (human monocyte), RAW 264.7 (murine macrophage) cells were obtained from the Korean Cell Line Bank (Korea). RAW 264.7 were maintained in DMEM (Capricorn) containing 10% FBS and 1% penicillin/streptomycin (Capricorn), and THP-1 cells were maintained in RPMI-1640 (Capricorn) containing 2% MycoXpert (Capricorn Scientific), 1% penicillin/streptomycin, and 10% FBS. For macrophage differentiation, THP-1 cells were incubated with 50 ng/mL phorbol 12-myristate 13-acetate (PMA; Sigma-Aldrich) for 24 h. For BMDM isolation, the tibias harvested from six- to eight-week-old male mice were flushed with RPMI-1640 culture medium, after which RBC lysis buffer (BioLegend) was added to remove red blood

cells. The cells were cultured in RPMI 1640 containing 20 ng/mL of macrophage-colony stimulating factor (SinoBiological), 1% penicillin/streptomycin, and 10% FBS. The media were changed every 3 days for 6 days. PMs were isolated from six- to eight-week-old male mice and maintained in RPMI 1640 containing 1% penicillin/streptomycin and 10% FBS. Cell viability was determined using a colorimetric MTS assay (Promega).

### **2.31. In Vivo Depletion of Macrophages**

For macrophage depletion, liposomes containing PBS (control) or clodronate were obtained from FormuMax Scientific Inc. A 200 µL amount of control or clodronate (1.4 mg) liposomes was intraperitoneally injected into mice 1 day before the IMQ treatment. A repeated injection of 100 µL of control or clodronate (0.7 mg) liposomes was carried out 3 days after the first injection. Macrophage depletion was evaluated either by staining macrophages in skin tissue using a primary antibody against CD68 (1:300, R&D Systems, MAB101141) or by flow cytometry analysis for PMs.

### **2.32. In Vitro Competitive Inhibition Assay**

For the competitive inhibition assay with LPS and HACN or 10 kDa free HA, THP-1 cells were preincubated with HACN or 10 kDa free HA (10, 25, or 50 µg/mL) for 60 min, followed by treatment of Cy5.5-LPS (10 µg/mL) for 30 min. After fixing

the cells with 4% PFA, the fluorescent intensity was analyzed using LSM 510 META NLO microscopy (Zeiss).

### **2.33. In Vitro Cellular Uptake Assay**

RAW 264.7 cells were preincubated with PBS, 100 ng/mL LPS, or 20 ng/mL IL-4. After 24h, the cells were incubated with 10 µg/mL Cy5.5-HALN for 10 min and then analyzed using flow cytometry. To observe the role of TLR4 on the association of HALN with macrophages, RAW 264.7 cells were transiently transfected with scrambled (siCtrl) or TLR4 siRNA (siTLR4) for 24 h and incubated with PBS or 100 ng/mL LPS. After 24 h, cells were treated with 10 µg/mL Cy5.5-HALN for 10 min and then analyzed using flow cytometry. Alternatively, cells were preincubated with control IgG2a or anti-TLR4 antibody (Novus Biologicals) for 1 h prior to LPS treatment.

### **2.34. RNA-seq and Bioinformatic Analysis**

Libraries for the RNA sequencing were generated using the NEBNext Ultra Directional RNASeq kit after rRNA removal at ebiogen. RNA-seq was carried out using the Illumina HiSeq X10 platform in the paired-end and unidirectional condition. The RNA-seq analysis pipelines were conducted using R (ver. 3.6) and systemPipeR (ver. 1.18.2). Adaptor sequences were removed from the raw sequencing files and aligned with *Mus musculus* annotation by Rsubread (ver.

1.24.6). Then, the read quantification was carried out using Genomic Alignments (ver. 1.20.1). The fragments per kilobase of transcript per million mapped reads (FPKM) was quantified using a “fpkm” option with robust median ratio method of DESeq2 (ver. 1.24.0). Limma (ver. 3.40.6) with the “voom” option was used for normalization of transcript reads. To identify the differentially expressed transcripts (DETs), the normalized sequencing counts were analyzed by EdgeR (ver. 3.26.7). Among the entire DETs, the fold change (FC) and adjusted P-value (<0.01) of the FPKM value (>2) in all experimental groups were selected as significantly changed transcripts. Gene names were annotated by Ensembl biomaRt (ver. 2.40.4). The graphs were generated by the gplots package (ver. 3.0.1.1). Based on the gene name annotation, differentially expressed genes (DEGs) were hierarchically clustered using the option of complete linkage and Euclidean distance. R (ver. 3.0.2) was used for the visualization of DEGs.

## **2.35. Immunoblot Analysis**

THP-1 cells were primed with PMA and incubated with LPS (1 µg/mL) for 30 min in the presence of PBS or HACN (100 µg/mL). Total protein extraction was performed using RIPA buffer [Tris-HCl (50 mM, pH 7.4), NaCl (150 mM), sodium

dodecyl sulfate (0.1%), NP-40 substitute (1.0%), and EDTA (1 mM)] containing phosphatase and protease inhibitors, and the Bradford assay was used to measure the protein concentration. Immunoblot analysis was carried out using polyacrylamide gel electrophoresis and the Trans- Blot turbo transfer system (Bio-Rad). The resultant membranes were immunoblotted with primary antibodies against NF- $\kappa$ B p65 (1:1000, Cell Signaling, 4764), p-NF- $\kappa$ B p65 (1:1000, Cell Signaling, 3033), I $\kappa$ B $\alpha$  (1:1000, Cell Signaling, 9242), p-JNK (1:1000, Cell Signaling, 9251), p-p38 (1:1000, Cell Signaling, 9211), JNK (1:1000, Cell Signaling, 9252), p38 (1:1000, Cell Signaling, 8690), IL-1 $\beta$  (1:1000, R&D Systems, AF-401-NA), and  $\beta$ -actin (1:10 000, Abcam, ab8226) and with the appropriate secondary antibodies conjugated with HRP (Bio-Rad). Protein signal was detected using enhanced luminescence (Bio-Rad)

### **2.36. In Vitro Macrophage Polarization**

For the M1 polarization experiment, BMDMs and PMs were incubated with LPS (10 ng/mL) and PBS or HACN (10, 25, or 50  $\mu$ g/mL), CA (0.2 or 0.6  $\mu$ g/mL), or 10 kDa free HA (25  $\mu$ g/mL) for 4 or 48 h. THP-1 cells primed with PMA were incubated with 20 ng/mL IFN- $\gamma$  (Peprotech) and 100 ng/

mL LPS in the presence of PBS or 60 kDa free HA (100  $\mu$ g/mL), HACN (10, 25, or 50  $\mu$ g/mL), HALNs (25, 50, or 100  $\mu$ g/mL), or LCA (1.6, 3.2, or 6.3  $\mu$ g/mL) for 4 or 48 h. For the M2 polarization experiment, BMDMs were incubated with IL-4 (20 ng/mL, Peprotech) in the presence of PBS or HACN (10  $\mu$ g/mL) for 4 h. PMA-primed THP-1 cells were treated with IL-13 (20 ng/mL, Peprotech) and IL-4 (20 ng/mL) for 4 or 48 h in the presence of PBS or HACN (25 or 50  $\mu$ g/mL), followed by RNA sequencing (RNA-Seq) analysis, quantitative real-time polymerase chain reaction (qPCR), or/and flow cytometric analysis to assess M1 and M2 induction. Flow Cytometric Analysis. Cells were incubated with an anti-mouse CD16/32 antibody (BD Bioscience) for 20 min and then stained with primary antibodies listed in Table S2 for an additional 1 h

### **2.37. Statistical analysis**

All the statistical analyses were based on biological replicates (n is indicated in the figures or figure legends) in the same set and carried out with GraphPad Prism version 6.0 (GraphPad Software). The statistical tests used for each experiment have been added to the corresponding figure legends. To determine P values for two groups as specified in each figure legend, a two-tailed Student's t-test or Mann-

Whitney test was employed. The results are expressed as means  $\pm$  S.E.M. Statistical significance is indicated as \* $P < 0.05$ , \*\* $P < 0.01$  and \*\*\* $P < 0.001$ .



## **IV. CONCLUSION**

In this study, I have demonstrated that HABA (HACN or HALN) suppress diet-induced weight gain (PART 1) and relieves symptoms of psoriasis (PART 2). In other words, HABA showed effects on both chronic inflammations diseases (CIDs). In addition, some groups previously have published papers on the efficacy of HANP on CID such as diabetes<sup>17, 72</sup>, osteoarthritis<sup>73</sup>, atherosclerosis<sup>16</sup> and IBD<sup>63</sup>. However, No one said that HANP had a comprehensive effect on CIDs. And here, I report that HABAs have potential as a nanomedicine for treatment of CIDs. HANPs may offer a powerful platform to treat many CIDs, whereas HANP bearing specific drugs might further improve or exhibit multiple therapeutic outcomes by simultaneous modulation of the same or different targets of the drugs and the HANPs, respectively, depending on the type of drug used.

## V. REFERENCE

1. Ghaben, A. L. & Scherer, P. E. Adipogenesis and metabolic health. *Nature reviews Molecular cell biology* **20**, 242–258 (2019).
2. Lin, F. & Lane, M. D. CCAAT/enhancer binding protein alpha is sufficient to initiate the 3T3-L1 adipocyte differentiation program. *Proceedings of the National Academy of Sciences* **91**, 8757–8761 (1994).
3. Siersbæk, R., Nielsen, R. & Mandrup, S. Transcriptional networks and chromatin remodeling controlling adipogenesis. *Trends in Endocrinology & Metabolism* **23**, 56–64 (2012).
4. Tontonoz, P., Hu, E. & Spiegelman, B. M. Stimulation of adipogenesis in fibroblasts by PPAR $\gamma$ 2, a lipid-activated transcription factor. *Cell* **79**, 1147–1156 (1994).
5. Wu, Z. *et al.* Cross-regulation of C/EBP $\alpha$  and PPAR $\gamma$  controls the transcriptional pathway of adipogenesis and insulin sensitivity. *Mol. Cell* **3**, 151–158 (1999).
6. Lefterova, M. I. *et al.* PPAR $\gamma$  and C/EBP factors orchestrate adipocyte biology via adjacent binding on a genome-wide scale. *Genes Dev.* **22**, 2941–2952 (2008).
7. Horton, J. D. *et al.* Activation of cholesterol synthesis in preference to fatty acid synthesis in liver and adipose tissue of transgenic mice overproducing sterol regulatory element-binding protein-2. *J. Clin. Invest.* **101**, 2331–2339 (1998).
8. Shimano, H. *et al.* Isoform 1c of sterol regulatory element binding protein is less active than isoform 1a in livers of transgenic mice and in cultured cells. *J. Clin. Invest.* **99**, 846–854 (1997).

9. Shimano, H. *et al.* Elevated levels of SREBP-2 and cholesterol synthesis in livers of mice homozygous for a targeted disruption of the SREBP-1 gene. *J. Clin. Invest.* **100**, 2115–2124 (1997).
10. Choi, K. Y. *et al.* Self-assembled hyaluronic acid nanoparticles as a potential drug carrier for cancer therapy: synthesis, characterization, and in vivo biodistribution. *Journal of Materials Chemistry* **19**, 4102–4107 (2009).
11. Choi, K. Y., Saravanakumar, G., Park, J. H. & Park, K. Hyaluronic acid-based nanocarriers for intracellular targeting: interfacial interactions with proteins in cancer. *Colloids and Surfaces B: Biointerfaces* **99**, 82–94 (2012).
12. Heo, R. *et al.* Hyaluronan nanoparticles bearing  $\gamma$ -secretase inhibitor: In vivo therapeutic effects on rheumatoid arthritis. *J. Controlled Release* **192**, 295–300 (2014).
13. Lapčík Jr, L., Lapčík, L., De Smedt, S., Demeester, J. & Chabrecek, P. Hyaluronan: preparation, structure, properties, and applications. *Chem. Rev.* **98**, 2663–2684 (1998).
14. Lee, G. Y. *et al.* Hyaluronic acid nanoparticles for active targeting atherosclerosis. *Biomaterials* **53**, 341–348 (2015).
15. Choi, K. Y. *et al.* Hyaluronic acid-based activatable nanomaterials for stimuli-responsive imaging and therapeutics: beyond CD44-mediated drug delivery. *Adv Mater* **31**, 1803549 (2019).
16. Beldman, T. J. *et al.* Hyaluronan nanoparticles selectively target plaque-associated macrophages and improve plaque stability in atherosclerosis. *Ac Nano* **11**, 5785–5799 (2017).
17. Rho, J. G. *et al.* Self-assembled hyaluronic acid nanoparticles: Implications as a nanomedicine for treatment of type 2 diabetes. *J. Controlled Release* **279**, 89–98 (2018).

18. Choi, K. Y. *et al.* Self-assembled hyaluronic acid nanoparticles for active tumor targeting. *Biomaterials* **31**, 106–114 (2010).
19. Phillips, J. N. The energetics of micelle formation. *Transactions of the Faraday Society* **51**, 561–569 (1955).
20. Tanabe, K. K. & Saya, H. The CD44 adhesion molecule and metastasis. *Critical Reviews™ in Oncogenesis* **5** (1994).
21. Ponta, H., Sherman, L. & Herrlich, P. A. CD44: from adhesion molecules to signalling regulators. *Nature reviews Molecular cell biology* **4**, 33–45 (2003).
22. Marhaba, R. & Zöller, M. CD44 in cancer progression: adhesion, migration and growth regulation. *Journal of molecular histology* **35**, 211–231 (2004).
23. Sugahara, K. N. *et al.* Hyaluronan oligosaccharides induce CD44 cleavage and promote cell migration in CD44-expressing tumor cells. *J. Biol. Chem.* **278**, 32259–32265 (2003).
24. Choi, K. Y. *et al.* PEGylation of hyaluronic acid nanoparticles improves tumor targetability in vivo. *Biomaterials* **32**, 1880–1889 (2011).
25. Cho, H. *et al.* Self-assembled nanoparticles based on hyaluronic acid–ceramide (HA–CE) and Pluronic® for tumor-targeted delivery of docetaxel. *Biomaterials* **32**, 7181–7190 (2011).
26. Ganesh, S., Iyer, A. K., Gattacceca, F., Morrissey, D. V. & Amiji, M. M. In vivo biodistribution of siRNA and cisplatin administered using CD44-targeted hyaluronic acid nanoparticles. *J. Controlled Release* **172**, 699–706 (2013).
27. Kang, H. S. *et al.* CD44 plays a critical role in regulating diet-induced adipose inflammation, hepatic steatosis, and insulin resistance. *PloS one* **8**, e58417 (2013).

28. Kodama, K. *et al.* Expression-based genome-wide association study links the receptor CD44 in adipose tissue with type 2 diabetes. *Proceedings of the National Academy of Sciences* **109**, 7049–7054 (2012).
29. Tran, T. H. *et al.* Targeted and controlled drug delivery system loading artersunate for effective chemotherapy on CD44 overexpressing cancer cells. *Arch. Pharm. Res.* **39**, 687–694 (2016).
30. Azeem, A. *et al.* Influence of Nonsulfated Polysaccharides on the Properties of Electrospun Poly (lactic-co-glycolic acid) Fibers. *ACS Biomaterials Science & Engineering* **3**, 1304–1312 (2017).
31. Bayer, I. S. Hyaluronic acid and controlled release: A review. *Molecules* **25**, 2649 (2020).
32. Snetkov, P., Zakharova, K., Morozkina, S., Olekhnovich, R. & Uspenskaya, M. Hyaluronic acid: The influence of molecular weight on structural, physical, physico-chemical, and degradable properties of biopolymer. *Polymers* **12**, 1800 (2020).
33. Kawasaki, K., Ochi, M., Uchio, Y., Adachi, N. & Matsusaki, M. Hyaluronic acid enhances proliferation and chondroitin sulfate synthesis in cultured chondrocytes embedded in collagen gels. *J. Cell. Physiol.* **179**, 142–148 (1999).
34. Greco, R. M., Iocono, J. A. & Ehrlich, H. P. Hyaluronic acid stimulates human fibroblast proliferation within a collagen matrix. *J. Cell. Physiol.* **177**, 465–473 (1998).
35. Price, R. D., Myers, S., Leigh, I. M. & Navsaria, H. A. The role of hyaluronic acid in wound healing. *American journal of clinical dermatology* **6**, 393–402 (2005).
36. Gomes, J., Amankwah, R., Powell-Richards, A. & Dua, H. S. Sodium hyaluronate (hyaluronic acid) promotes migration of human corneal epithelial cells in vitro. *Br. J. Ophthalmol.* **88**, 821–825 (2004).

37. Shigeda, W. *et al.* Hyaluronic acid enhances cell migration and invasion via the YAP1/TAZ–RHAMM axis in malignant pleural mesothelioma. *Oncotarget* **8**, 93729 (2017).
38. Kikuchi, S., Griffin, C. T., Wang, S. & Bissell, D. M. Role of CD44 in epithelial wound repair: migration of rat hepatic stellate cells utilizes hyaluronic acid and CD44v6. *J. Biol. Chem.* **280**, 15398–15404 (2005).
39. Weigel, P. H., Frost, S. J., McGary, C. T. & LeBoeuf, R. D. The role of hyaluronic acid in inflammation and wound healing. *Int. J. Tissue React.* **10**, 355–365 (1988).
40. Litwiniuk, M., Krejner, A., Speyrer, M. S., Gauto, A. R. & Grzela, T. Hyaluronic acid in inflammation and tissue regeneration. *Wounds* **28**, 78–88 (2016).
41. Ialenti, A. & Di Rosa, M. Hyaluronic acid modulates acute and chronic inflammation. *Agents Actions* **43**, 44–47 (1994).
42. Jiang, D., Liang, J. & Noble, P. W. Hyaluronan in tissue injury and repair. *Annu. Rev. Cell Dev. Biol.* **23**, 435–461 (2007).
43. Tavianatou, A. G. *et al.* Hyaluronan: molecular size-dependent signaling and biological functions in inflammation and cancer. *The FEBS journal* **286**, 2883–2908 (2019).
44. Tian, X. *et al.* High-molecular-mass hyaluronan mediates the cancer resistance of the naked mole rat. *Nature* **499**, 346–349 (2013).
45. Rayahin, J. E., Buhrman, J. S., Zhang, Y., Koh, T. J. & Gemeinhart, R. A. High and low molecular weight hyaluronic acid differentially influence macrophage activation. *ACS biomaterials science & engineering* **1**, 481–493 (2015).
46. Ruppert, S. M., Hawn, T. R., Arrigoni, A., Wight, T. N. & Bollyky, P. L. Tissue integrity signals communicated by high-molecular weight hyaluronan and the resolution of inflammation. *Immunol. Res.* **58**, 186–192 (2014).

47. Lee, B. M., Park, S. J., Noh, I. & Kim, C. The effects of the molecular weights of hyaluronic acid on the immune responses. *Biomaterials Research* **25**, 1–13 (2021).
48. Park, B. *et al.* Enzymatic fragments of hyaluronan inhibit adipocyte differentiation in 3T3-L1 pre-adipocytes. *Biochem. Biophys. Res. Commun.* **467**, 623–628 (2015).
49. Park, B., Park, Y., Park, J. W., Shin, E. & Shin, W. Anti-obesity potential of enzymatic fragments of hyaluronan on high-fat diet-induced obesity in C57BL/6 mice. *Biochem. Biophys. Res. Commun.* **473**, 290–295 (2016).
50. Ji, E. *et al.* Inhibition of adipogenesis in 3T3-L1 cells and suppression of abdominal fat accumulation in high-fat diet-feeding C57BL/6J mice after downregulation of hyaluronic acid. *Int. J. Obes.* **38**, 1035–1043 (2014).
51. Lowes, M. A., Suarez-Farinás, M. & Krueger, J. G. Immunology of psoriasis. *Annu. Rev. Immunol.* **32**, 227 (2014).
52. Pasparakis, M., Haase, I. & Nestle, F. O. Mechanisms regulating skin immunity and inflammation. *Nature reviews immunology* **14**, 289–301 (2014).
53. Raposo, I. & Torres, T. Palmoplantar psoriasis and palmoplantar pustulosis: current treatment and future prospects. *American journal of clinical dermatology* **17**, 349–358 (2016).
54. Mason, A. R., Mason, J. M., Cork, M. J., Hancock, H. & Dooley, G. Topical treatments for chronic plaque psoriasis of the scalp: a systematic review. *Br. J. Dermatol.* **169**, 519–527 (2013).
55. Prausnitz, M. R., Mitragotri, S. & Langer, R. Current status and future potential of transdermal drug delivery. *Nature reviews Drug discovery* **3**, 115–124 (2004).

56. Barry, B. W. Breaching the skin's barrier to drugs. *Nat. Biotechnol.* **22**, 165–167 (2004).
57. Jiang, D., Liang, J. & Noble, P. W. Hyaluronan as an immune regulator in human diseases. *Physiol. Rev.* **91**, 221–264 (2011).
- 
58. Duncan, R. The dawning era of polymer therapeutics. *Nature reviews Drug discovery* **2**, 347–360 (2003).
59. Zhu, Y., Crewe, C. & Scherer, P. E. Hyaluronan in adipose tissue: Beyond dermal filler and therapeutic carrier. *Science translational medicine* **8**, 323ps4 (2016).
60. Jiang, D. *et al.* Regulation of lung injury and repair by Toll-like receptors and hyaluronan. *Nat. Med.* **11**, 1173–1179 (2005).
61. Zheng, L., Riehl, T. E. & Stenson, W. F. Regulation of colonic epithelial repair in mice by Toll-like receptors and hyaluronic acid. *Gastroenterology* **137**, 2041–2051 (2009).
62. Rao, N. V. *et al.* Recent developments in hyaluronic acid-based nanomedicine for targeted cancer treatment. *Expert opinion on drug delivery* **13**, 239–252 (2016).
63. Lee, Y. *et al.* Hyaluronic acid–bilirubin nanomedicine for targeted modulation of dysregulated intestinal barrier, microbiome and immune responses in colitis. *Nature materials* **19**, 118–126 (2020).
64. Wan, T. *et al.* Effects of nanoparticles with hydroscopic nicotinamide on tacrolimus: permeability through psoriatic skin and antipsoriatic and antiproliferative activities. *International journal of nanomedicine* **12**, 1485 (2017).
65. Zhang, Y. *et al.* CD44 assists the topical anti-psoriatic efficacy of curcumin-loaded hyaluronan-modified ethosomes: A new strategy for clustering drug in inflammatory skin. *Theranostics* **9**, 48 (2019).

66. Dolz-Pérez, I. *et al.* Polypeptide–corticosteroid conjugates as a topical treatment approach to psoriasis. *J. Controlled Release* **318**, 210–222 (2020).
67. Pandey, M. *et al.* Hyaluronic acid–modified betamethasone encapsulated polymeric nanoparticles: fabrication, characterisation, in vitro release kinetics, and dermal targeting. *Drug delivery and translational research* **9**, 520–533 (2019).
68. Chatterjee, S., Hui, P. C., Kan, C. & Wang, W. Dual–responsive (pH/temperature) Pluronic F–127 hydrogel drug delivery system for textile–based transdermal therapy. *Scientific reports* **9**, 1–13 (2019).
69. Min, H. S. *et al.* Liver-specific and echogenic hyaluronic acid nanoparticles facilitating liver cancer discrimination. *Advanced Functional Materials* **23**, 5518–5529 (2013).
70. Zhang, L. *et al.* Activatable hyaluronic acid nanoparticle as a theranostic agent for optical/photoacoustic image–guided photothermal therapy. *Acs Nano* **8**, 12250–12258 (2014).
71. Kamat, M. *et al.* Hyaluronic acid immobilized magnetic nanoparticles for active targeting and imaging of macrophages. *Bioconjug. Chem.* **21**, 2128–2135 (2010).
72. Lee, W. H. *et al.* Self–assembled hyaluronic acid nanoparticle suppresses fat accumulation via CD44 in diet–induced obese mice. *Carbohydr. Polym.* **237**, 116161 (2020).
73. Kang, L. *et al.* Self–assembled hyaluronic acid nanoparticles for osteoarthritis treatment. *Biomaterials* **275**, 120967 (2021).
74. Udenfriend, S. *et al.* Fluorescamine: a reagent for assay of amino acids, peptides, proteins, and primary amines in the picomole range. *Science* **178**, 871–872 (1972).

75. Shi, Z. *et al.* Bile Acids Improve Psoriasiform Dermatitis through Inhibition of IL-17A Expression and CCL20–CCR6–Mediated Trafficking of T Cells. *J. Invest. Dermatol.* **142**, 1381–1390, e11 (2022).
76. Paik, D. *et al.* Human gut bacteria produce TH17–modulating bile acid metabolites. *Nature* **603**, 907–912 (2022).
77. Stratis, A. *et al.* Pathogenic role for skin macrophages in a mouse model of keratinocyte–induced psoriasis–like skin inflammation. *J. Clin. Invest.* **116**, 2094–2104 (2006).
78. Wang, H. *et al.* Activated macrophages are essential in a murine model for T cell–mediated chronic psoriasiform skin inflammation. *J. Clin. Invest.* **116**, 2105–2114 (2006).
79. Varga, G., Ludwig, S. & Wixler, V. Leite Dantas R, Masemann D, Schied T, Bergmeier V, Vogl T, Loser K. Brachvogel Macrophage–mediated psoriasis can be suppressed by regulatory T lymphocytes B. *J. Pathol.* **240**, 366–377 (2016).
80. Lu, C. *et al.* Involvement of M1 macrophage polarization in endosomal toll–like receptors activated psoriatic inflammation. *Mediators Inflamm.* **2018** (2018).
81. Rooijen, N. v. & Hendrikx, E. in *Liposomes* 189–203 (Springer, 2010).
82. Fuchs, E. & Green, H. Changes in keratin gene expression during terminal differentiation of the keratinocyte. *Cell* **19**, 1033–1042 (1980).
83. Candi, E., Schmidt, R. & Melino, G. The cornified envelope: a model of cell death in the skin. *Nature reviews Molecular cell biology* **6**, 328–340 (2005).
84. Stratis, A. *et al.* Pathogenic role for skin macrophages in a mouse model of keratinocyte–induced psoriasis–like skin inflammation. *J. Clin. Invest.* **116**, 2094–2104 (2006).

85. Wang, H. *et al.* Activated macrophages are essential in a murine model for T cell-mediated chronic psoriasiform skin inflammation. *J. Clin. Invest.* **116**, 2105–2114 (2006).



## VI. ABSTRACT IN KOREAN (국문초록)

여러 소수성 중심 부분을 친수성 히알루론산으로 둘러싸고 있는 자가 조립 히알루론산 나노입자(HANP)는 나노 운반체로서 광범위하게 연구되어 왔다. 그런데 흥미롭게도 최근 몇 그룹에서 어떤 약물도 함유하지 않은 빈 HANP가 제2형 당뇨병, 관절염 및 동맥경화증 치료를 위한 잠재적인 치료제라고 보고했다. 여기, 나는 비만과 건선을 포함한 다른 만성 염증성 질환에서 HANP의 효능을 보고한다. 첫번째로 자가조립 히알루론-담즙산 나노 입자 (HABA)가 지방세포생성과 지방산합성에 미치는 효과를 평가하여 비만 치료제로서의 가능성을 확인했다. HABA를 3T3L-1 지방 전구세포에 처리하면 지방세포생성 및 지질 축적이 높도 의존적으로 억제되고, 주요 지방세포생성 및 지방산합성 조절인자의 발현이 감소했다. 그러나, 이러한 HABA 매개 효과는 CD44에 대한 siRNA로 형질주입 된 3T3-L1 세포에서는 관찰되지 않았다. 이러한 결과와 일치하게, 식이 유도 비만 마우스의 HABA 치료는 체중과 부고환 지방량을 감소시켰고, 지방세포생성 및 지방산합성 조절인자의 유도를 억제한 반면, CD44가 없는 마우스에서는 이러한 효과가 약화되었다. 그 다음으로 나는 건선 치료를 위한 치료제로서 HABA의 가능성을 확인했다. HABA는 뚜렷한 독성 징후

없이 각질세포의 과증식과 대식세포의 M1 분화를 억제함으로써 건선 유사 피부에 대해 강력한 치료 효능을 발휘했다. 경피투여 된 HABA는 염증이 있는 피부에서 전 염증성 대식세포에 축적되어 대식세포의 M1 분극화를 억제하는 것으로 확인되었다. 그 결과, HABA는 IMQ로 유발된 건선 유사 마우스에서 기존 약물에 비해 현저한 효능을 보였다. 종합하면, 나는 HANP가 비만 관련 만성 염증성 질환 치료를 위한 나노의약으로서의 가능성을 가지고 있음을 보고한다.